Structural characterization and tectonic evolution of 1.3 Ga REE-bearing Fox Harbour Volcanic Belt, southeast Labrador - Canada.

Submitted by:

Nicolas Prieto-Moreno

A dissertation submitted to the School of Graduate Studies of
In partial fulfillment of the requirements for the degree of

Master of Science (MSc.)

Department of Earth Sciences

Memorial University of Newfoundland

May 2025

St. John's, Newfoundland

Abstract

The Southeastern Labrador region, Canada, preserves a complex geological history shaped by multiple deformation and metamorphic events. This study investigates the structural evolution, metamorphism, and deformation of the 1.3 Ga Fox Harbour Volcanic Belt (FHVB), a bimodal volcano-sedimentary sequence of peralkaline rhyolites enriched in rare earth elements (REE), mafic rocks, and sedimentary rocks deposited on 1.7-1.5 Ga basement rocks in an extensional setting along the Laurentian margin. Hosted in a highly strained amphibolite-facies corridor within the Lake Melville terrane (LMT), the FHVB domain is bordered by the Long Harbour (LHsz) and Fox Harbour (FHsz) shear zones to the south and north, respectively. Field observations, structural and petrographic analyses, along with U-Pb petrochronology on zircon, monazite, and titanite, reveal a multi-stage tectonic evolution. Deformation that accompanied the main phase of Grenvillian metamorphism (D1; ~1.06–1.04 Ga) locally involved amphibolite-facies metamorphism and anatexis, tight buckle folding, and tectonic burial of the LMT during Grenvillian convergence. The Pinware and Mealy Mountains terranes remained structurally higher in the tectonic pile and were shielded from significant metamorphism. Continued deformation (D2; ~1.04–1.02 Ga) was characterized by cooling, folding, and localized strain during a period of orogenic collapse, characterized by extensional adjustments of the orogenic crust. Late-stage transpressive deformation (D3; ~1.0 Ga) involved greenschist-facies oblique-slip and strike-slip shearing, overprinting earlier amphibolite-facies fabrics and facilitating the FHVB exhumation. These findings refine the tectonometamorphic history of the FHVB, providing new insights into the kinematic evolution of the Southeastern Grenville Province.

Acknowledgments

First, I would like to express my sincere gratitude to my supervisor, Dr. Eric J. Thiessen, for his invaluable support and mentorship throughout this research project. From guiding me during my first field visit in Labrador to providing insightful lessons during coursework, his encouragement and expertise have been pivotal over the past two years. His constructive feedback, both during the early stages and in refining this document, has significantly enhanced my analytical and writing skills. I would also like to thank my committee member, Dr. Philipe Belley, for his thoughtful comments and feedback on this thesis.

I want to acknowledge the financial support provided by NRCan's Targeted Geoscience Initiative (TGI) program, which funded this research as part of the Magmatic Ore Systems Sub-Activity: Critical minerals within carbonatite, syenite, and allied peralkaline-alkaline rocks in the central and eastern parts of the Canadian Shield: Where, when, and how were they formed. I sincerely appreciate the support of Search Minerals, particularly R. Miller and J. Haley, for granting ground access and providing valuable data. I extend special thanks to Dr. Zsuzsanna Magyarosi from the Geological Survey of Newfoundland and Labrador for her field guidance and insightful discussions about the geology of the study area.

Special acknowledgment goes to Dr. Steve Denyszyn for performing the thermal annealing of zircon grains and to Dr. Greg Dunning for conducting the chemical abrasion process on the analyzed zircons. Dr. Dunning's invaluable feedback and insightful discussions greatly contributed to advancing my research project. I extend my gratitude to the CREAIT staff

for assisting in sample preparation for mineral separation and supporting data acquisition using the scanning electron microscope and mass spectrometry instruments at Memorial University of Newfoundland.

Lastly, I express my heartfelt gratitude to my family, who encouraged and supported me from a distance while I was studying abroad; their belief in me has been a constant source of motivation. I am equally grateful to the colleagues and friends I have made over the past two years for making this journey an enriching and memorable experience.

Table of Contents

List of Tables

List of Figures

List of Appendices

Chapter 1 Thesis Introduction

1.1 Introduction

The Grenville Province in Labrador, Canada, preserves a complex geological record of Paleoproterozoic to Mesoproterozoic orogenic phases punctuated by extensional periods between approximately 1.8 and 0.9 Ga. These orogenic events are grouped into different geological stages: pre-Labradorian (>1710 Ma), Labradorian (1710-1600 Ma), Pinwarian (1520-1460 Ma) orogenesis, Elsonian magmatic event (1460-1230 Ma), Grenvillian Orogeny (1090-985 Ma), and post-Grenvillian events [985-955 Ma] (Gower, 1996; Gower and Krogh, 2002). These events are recorded in different terranes (Figure 1.1), which are shear-bounded crustal blocks with unique timing and styles of crust formation, deformation, and metamorphism (Scharer et al., 1986; Scharer and Gower, 1988; Gower et al., 1991; Gower 1996, 2008b). The study area, between Port Hope Simpson and St. Lewis, Labrador, lies within the Lake Melville terrane (LMT), an arcuate high-strain corridor over 300 km long and 20 km wide, separated from the Pinware terrane (PT) to the south by the Long Harbour shear zone (LHsz). The 1.3 Ga Fox Harbour bimodal volcanic belt (FHVB), located within this high-strain corridor, comprises strongly deformed and metamorphosed peralkaline rhyolites that host Rare Earth Elements (REE) mineralization (Haley, 2014).

Previous studies have interpreted pervasive ductile deformation in the region, occurring at amphibolite- (~500–700 °C at 3–12 kbars) to granulite-facies (>700 °C at 4–13 kbars) around ~1.6 Ga (Gower, 1985; Hanmer and Scott, 1990; Scott et al., 1993; Gower, 2005), while narrow belts of greenschist-facies (~300-500 °C at 2-8 kbars) mylonites formed at ~

1.0 Ga within the LMT (Hanmer and Scott, 1990; Scott et al., 1993). In the northern LMT, Corrigan et al. (2000) reported pervasive Grenvillian-aged deformation and metamorphism, and given the intense high-temperature deformation observed in the 1.3 Ga FHVB, it is reasonable to expect that similar Grenvillian overprinting also affected the LMT in southeast Labrador. However, the kinematics, metamorphic conditions, and precise ages of these deformational events in the area remain poorly characterized. Moreover, no detailed studies at this project's scale have focused on the deformational ages and structural style of the host rocks in the FHVB and LMT (e.g., Scott et al., 1993). Mineralization in the FHVB occurs in three distinct horizons, possibly representing either stratigraphic layers (Miller, 2015) or a single structurally repeated sequence. However, current field relationships and geochronology are insufficient to test these models.

This project builds upon prior geophysical data (Search Minerals, 2010) and existing bedrock maps (Gower, 2005) as a basis for detailed field observation and sample collection in the FHVB and its bounding structures. The aim is to combine age data with structural data to discern deformation styles, kinematics, and the tectonic evolution of the FHVB. Field analysis and oriented thin-section petrography provide information into rock deformation kinematics and deformation temperatures via quartz microstructures (Trouw and Passchier, 2009) and the metamorphic conditions in each tectonic domain. Additionally, U-Pb zircon dating using Chemical-Abrasion Laser Ablation Inductively Coupled Plasma Mass Spectrometry (CA-LA-ICPMS) was performed on augen-gneiss, mafic and sedimentary rocks of the FHVB, as well as on orthogneiss and deformed dykes within shear zones.

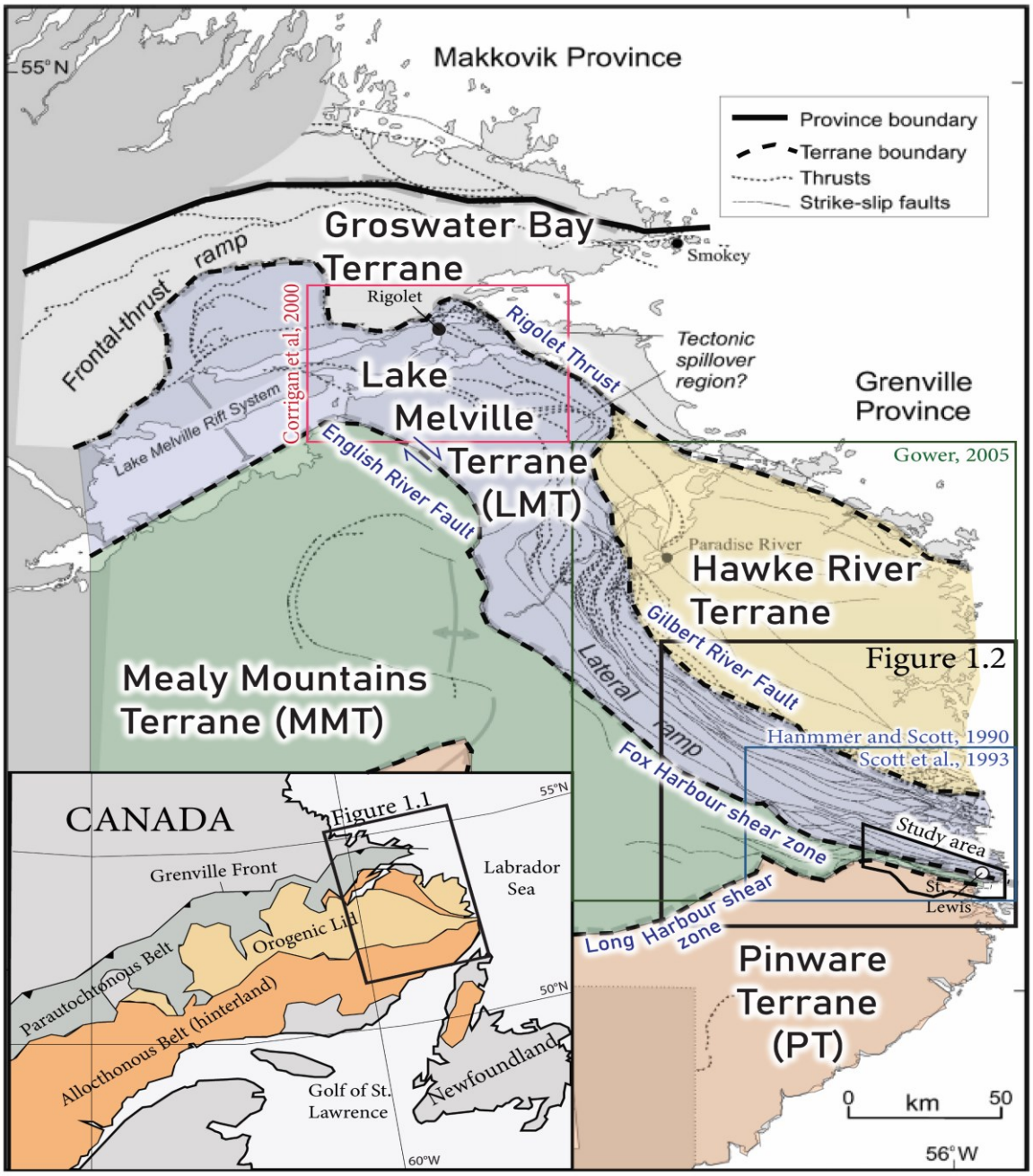

Figure 1.1 *Tectonic divisions of the Eastern Grenville Province (inset) according to Rivers et al., 1989, showing the Parautochtonous and Allochtonous Belts and the Orogenic Lid. The main figure shows Eastern Labrador with the different tectonic terranes (modified from Gower, 2008b). Areas of previous studies and mapping projects in this region are shown and the study area of the present project is outlined.*

Complementary in-situ U-Pb LA-ICPMS analysis of titanite and monazite will provide additional constraints in protolith, metamorphic, and deformational ages. These data are critical for understanding the nature of and structural modification of the REE deposits in

Southeast Labrador, as well as for testing existing models of Mesoproterozoic tectonics in the region, such as the indentor tectonism model proposed by Gower et al. (2008a), which outlines a transition from NW-verging thrusting in the Rigolet area (Corrigan et al., 2000) to lateral-ramp tectonics along the southeast Labrador coast (Figure 1.1).

1.2 Geological Framework

The orogenic events in southeastern Labrador are grouped into distinct geological stages (Gower, 1996, 2019; Gower and Krogh, 2002) that occurred at the southern margin of Laurentia and are presented below:

i) **Pre-Labradorian events (>1710 Ma)**: These include magmatic events between 1810 and 1775 Ma (Gower et al., 2008b) and the emplacement of A-type granitoid rocks between 1.75 and 1.71 Ga.

ii) **Labradorian Orogenesis (1710–1600 Ma)**: This stage involves the accretion of an outboard, oceanward-subducting calc-alkaline pre-Labradorian arc, that evolved into a collisional orogen with Laurentia (Gower 1996, 2019 and references therein). Three different sequential magmatic events were classified in this orogeny at 1677 Ma, 1671 Ma, and 1658-1649 (Gower, 1992). Late Labradorian events (1625-1600 Ma) include the emplacement of minor granitic intrusions and waning deformational activity, leading to the development of a passive continental margin until 1520 Ma, potentially associated with the Plus Value sequence inferred to have formed from rifting of pericratonic segments

at 1.50 Ga in central Grenville Province (Indares, 2020). However, no specific sedimentological information from eastern Labrador is available for this stage (Gower, 1996; Gower and Krogh, 2002; Gower, 2019).

iii) **Pinwarian Orogenesis (1520–1460 Ma)**: Characterized by widespread voluminous granitic magmatism accompanied by metamorphism, between ca. 1.5 – 1.47 Ga (Gower and Tucker, 1994; Gower and Krogh, 2002 and references therein), with minor intrusions emplaced at 1509 Ma (Scott et al., 1993) and 1474 Ma (Corrigan et al., 2000), reflecting a continental-margin arc developed above a north-dipping subduction zone (Gower and Tucker, 1994; Gower 1996, 2019).

iv) **Elsonian event (1460-1230 Ma)**: Representing a stable but intermittently extensional tectonic environment (Gower and Krogh, 2002; Gower, 2019), this event includes the emplacement of mafic magmatism and the Anorthosite-Mangerite-Charnockite-Granite (AMCG) Nain Plutonic Suite between 1460-1290 Ma outside of the Grenville province(Gower 1996, 2019), and the 1.3 Ga FHVB felsic volcanism alongside the 1296 Ma Upper North River granite and the 1250 Ma mafic magmatism of the Mealy Dykes in southeast Labrador (Haley, 2014; Miller, 2015; Gower, 1996; Gower and Krogh, 2002).

v) **Grenvillian orogenesis (1090-985 Ma):** Represents a continent-continent collision between Amazonia and the southern margin of Laurentia (Tohver et al., 2004) marked by the formation and collapse of a thick orogenic plateau during the Ottawan phase (1090–1020 Ma), exposed in the hinterland (or Allochthonous Belt) across the Grenville Province with local Rigolet-age

(1005-980 Ma) overprints (Rivers et al., 2012). The Ottawan phase comprises an early interval (1085–1050 Ma) associated with tectonic burial and peak metamorphism in the medium-pressure segment, followed by a period of orogenic collapse (1050-1020 Ma), characterized by normal to transtensional adjustments of the orogenic crust, suggesting active extension (Indares, 2024). In the Parautochthonous Belt, northwest propagation of structures during the Rigolet phase (1005–980 Ma) marks the advance of the orogen against the Archean lithosphere of internal Laurentia (Hoffman, 1989). In southeast Labrador, distinct thermal peaks at varying times define multiple tectonothermal events (Gower and Krogh, 2002). Gower et al. (2008) subdivided this orogenesis into early (1085-1040 Ma), mid- (1040–1010 Ma), and late (1010–985 Ma) Grenvillian phases, which vary along strike, rejecting the terms "Ottawan" and "Rigolet" orogenies as they suggest the events in eastern Grenville province occurred within a continuous tectonic process.

i) **Post-tectonic Grenvillian magmatism (985-955 Ma):** Comprising alkalic mafic-anorthositic magmatism between 985 and 975 Ma, and granitic magmatism between 975 and 955 Ma, these events mark the end of the Grenvillian orogeny and are attributed to late stages of orogenic collapse (Rivers et al. 2012) or related with late stages of opening of the Asgard sea (Strowbridge et al., 2022).

Rivers et al. (1989) regionally divided the Grenville Province into the Parautochthonous Belt at the northwest margin and a composite Allochthonous Belt to the southeast,

representing the orogenic hinterland. The Allochthonous Belt consists of shear-zone-bounded crustal panels buried at different depths during the high-temperature Ottawan (1090–1020 Ma) phase, while the Orogenic Lid largely escaped Ottawan metamorphism and deformation at higher crustal levels (Rivers, 2012) (Inset. Figure 1.1). The Parautochthonous Belt connects with the orogenic foreland and underwent lower-temperature deformation and metamorphism during the late stages of the late Rigolet (1005–980 Ma) phase (Rivers, 2009).

Expanding on the regional division by Rivers et al. (1989), the Grenville Province also includes an Exterior Thrust Belt (Gower et al., 1991), which falls within the Allochthonous Belt. This Exterior Thrust Belt encompasses terranes primarily influenced by the Labradorian orogeny and includes high- to medium-grade metamorphic rocks, such as pelitic gneiss and calc-alkaline plutonic rocks (Scharer et al., 1986; Scharer and Gower, 1988; Gower et al., 1991; Gower, 1996). Bounded by the Grenville Front, this thrust belt marks the northern extent of significant Grenvillian and Labradorian deformation (Owen, 1988; Gower, 1996). In the study area, the thrust belt is divided into the Hawke River terrane (HRT), Lake Melville terrane (LMT), and Mealy Mountains terrane (MMT) (Gower, 1996; Rivers, 2009) (Figure 1.1).

Details of geological characteristics, bounding shear zones, basement rock types, plutonic and metamorphic ages, and tectonic interpretations are elaborated below based on relevance to the present study.

1.2.1 Lake Melville Terrane (LMT)

The LMT is a major crustal feature extending 300 km long and 60 km wide (Gower and Owen, 1984), narrowing to the southeast into the highly deformed ~ 20 km wide zone with intense northwest-trending dextral strike-slip deformation and younger sinistral movement cutting the dextral mylonitic shears (Hanmer and Scott, 1990; Scott et al., 1993) (Figure 1.2A). The LMT experienced Grenvillian tectonometamorphism (Gower, 2019) and comprises two distinct structural regions (Figure 1.1): i) The northern part, west of Rigolet, features a stack of pervasive Labradorian northwest-verging thrust panels, overprinted by high-grade Grenvillian metamorphism (Corrigan et al., 2000), and ii) the southern part, from the southern Labrador coast to Rigolet, consists of northwest-trending steep dextral strike-slip segments, interpreted to represent Labradorian (Scott et al., 1993) or Grenvillian metamorphism (Gower et al., 1997a; Gower 2005, 2012, 2019).

The northern boundary of the LMT is defined in the north by the 1.05 Ga Rigolet thrust zone (Corrigan et al., 2000; Gower, 2019) and to the southeast by the dextral strike-slip Gilbert River fault (Gower et al., 1987). The southern boundary with the Mealy Mountains terrane (MMT) is marked by the 1.01 Ga dextral strike-slip English River shear (Gower, 1985; Corrigan et al., 2000), while the southeast boundary with the Pinware Terrane (PT) consists of reverse- and strike-slip shear zones (Figure 1.1).

Near St. Lewis, Labrador, interpretations of the LMT footprint vary; Scott et al. (1993) propose that the Long Harbour shear zone (LHsz) separates the LMT from the Pinware terrane (Figure 1.2B). Conversely, Gower (2019) suggests a 5 km wide sliver of MMT (Orogenic Lid) is wedged between the LMT and the PT, formed by northeast-striking,

southeast-verging thrust/reverse, and strike-slip faults, marking the boundary between the MMT and the PT (Figure 1.2C).

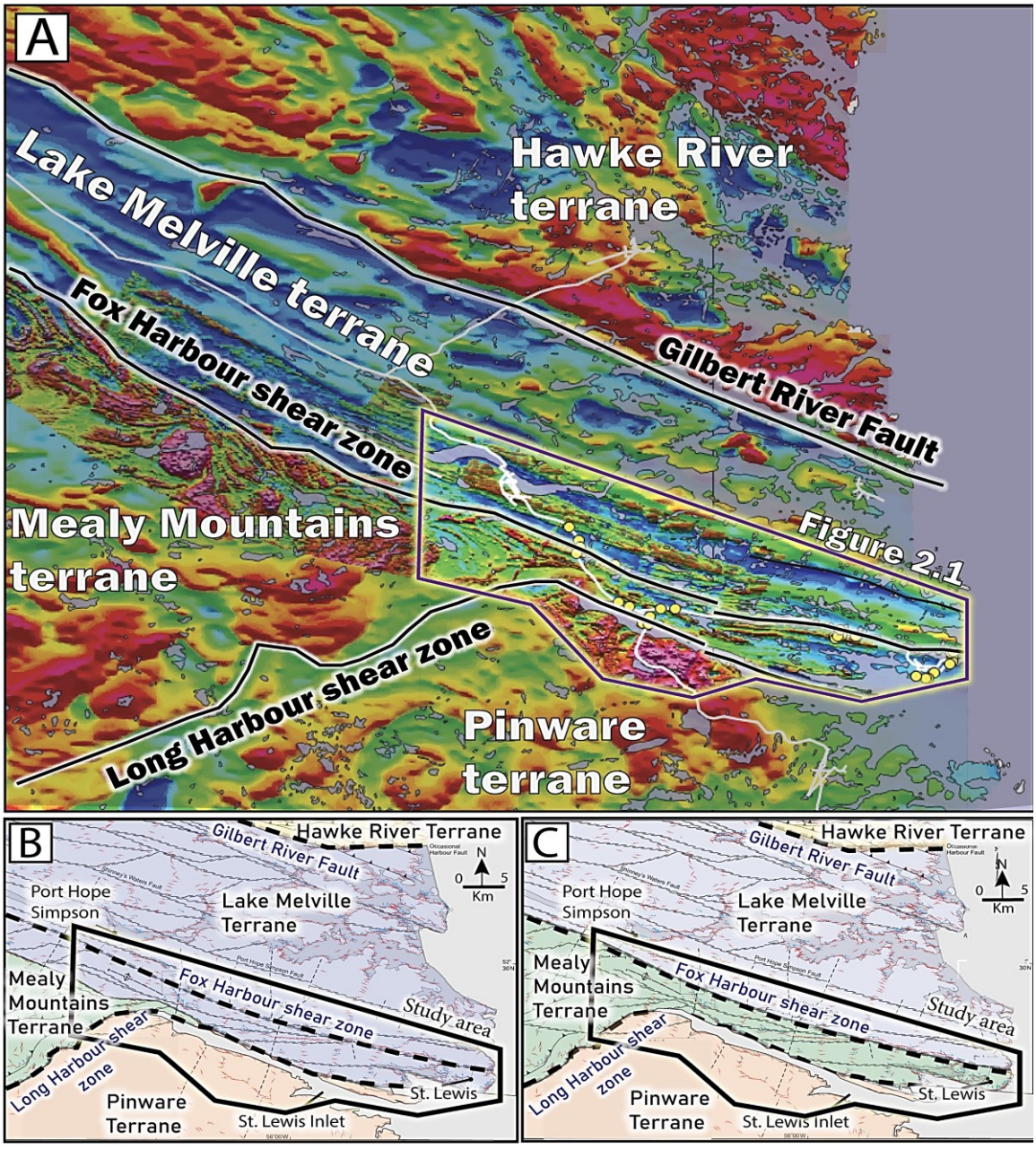

Figure 1.2 A) *Regional aeromagnetic anomalies in southeast Labrador and the Search Minerals TMI 2010: A distinctive low magnetic anomaly in blue colour is identified within the high-strain corridor of the LMT, contrasting with the more pronounced, massive, and higher magnetic anomalies observed in the adjacent terranes. Yellow dots represent the outcrops stations visited in this work.* ***B)*** *Interpretation 1****:*** *southeast extension of LMT bouded south by the LHsz according to Scott et al., 1993; black box showing the study area.* ***C)*** *Interpretation 2: A thin sliver of MMT wedged between the LMT and PT (Gower, 2019). Map modified from Gower 2019.*

The LMT bedrock consists of mylonitic K-feldspar megacrystic granitoids and orthogneiss, grading into migmatites with protolith ages of 1678 and 1677 Ma (Gower et al., 1992). In the southern part of the LMT, Scott et al. (1993) identified minor Labradorian granitic intrusions (1664-1644 Ma) that underwent amphibolite-facies deformation similar to their host rocks. Additionally, Scott et al. (1993) reported a 1509 Ma Pinwarian granitic vein near the LHsz and syntectonic granitic veins with a U-Pb zircon age of 1113 Ma and monazite age of ~1078 Ma, attributed to tectonic-magmatic activity during Grenvillian orogenesis.

In the northern part of the LMT, northeast-verging thrusting and granulite-facies metamorphism occurred at the margin of the Rigolet thrust zone during late Labradorian orogenesis (1619-1610 Ma), followed by high-grade deformation and uppermost-amphibolite-facies metamorphism during Grenvillian tectonism (1050-1045 Ma). The Rigolet thrust zone preserves Grenvillian reactivation in upper structural levels, while Labradorian fabrics are preserved within lower crustal levels (Corrigan et al., 2000). Pinwarian magmatism includes 1489 Ma to 1474 Ma intermediate to felsic intrusions and gabbro emplacement at ca. 1472 Ma (Corrigan et al., 2000) and ca. 1426 Ma (Michael and Shabogamo gabbro dyke swarms, Scharer et al., 1986). In the northern LMT, a 1038 Ma metamorphic overprint in an undated amphibolite mafic dyke located in the Upper North River (Scharer et al., 1986) aligns with zircon, monazite and titanite dates between 1040 and 1026 Ma (Scharer et al., 1986; Scharer and Gower, 1988). Additionally, a 1003 Ma pegmatite (Gower, 1991) intrudes a migmatitic gneiss at the northeastern part of the

boundary between the MMT and the LMT, representing the youngest reported Grenvillian age in this terrane.

1.2.2 Mealy Mountains Terrane (MMT)

The MMT comprises a pre-Labradorian crust (Gower et al., 1995) with two main rock groups: i) 1646 Ma anorthositic and leucogabbroic rocks in the north, and ii) sillimanite-bearing pelitic gneiss, felsic to mafic plutons, and orthogneiss in the southeast side. Pinwarian plutonism is represented by the 1510–1470 Ma magmatism (Gower et al., 1993; Wasteneys et al., 1997). The Mealy Mountain Intrusive Suite is intruded by the northeast-striking Mealy dykes (olivine tholeiitic gabbros), with crystallization ages of 1380 Ma (Rb-Sr [whole-rock], Emslie et al., 1984) and 1245 Ma (^{40}Ar-^{39}Ar [amphibole and biotite], Reynolds, 1989). A granodiorite dyke (1047 Ma) intrudes sillimanite-bearing metasedimentary gneiss at the LMT/MMT boundary (Wasteneys et al., 1997). The youngest event is an undeformed granite emplaced at 962 ± 3 Ma in the southeast part of the MMT (Gower, 1996).

This terrane exhibits subtle Grenvillian metamorphism (1020-1000 Ma) evidenced in localized deformation from thrusting (1010 Ma), sporadic Grenvillian magmatism**,** and post-tectonic granitoid pluton emplacement (990-960 Ma) (Gower, 2019)**.** According to Rivers (2008), the MMT consists principally of Labradorian basement and belongs to the Orogenic Lid (Inset Figure 1.1), lacking penetrative high-temperature Ottawan metamorphism and deformation (1090-1020 Ma). In the study area, according to one model (see Fig. 1.2C) the northeast flank of the MMT is faulted against the LMT by the FHsz

(Gower, 1996) and in the southeast part by the LHsz which separates the MMT from the PT (Figure 1.1).

1.2.3 Pinware Terrane (PT)

The northern boundary of this terrane is defined by the Long Harbour shear zone (Gower, 1988). Supracrustal units include quartzites deposited around 1805 Ma and pelitic schist-gneiss, reflecting a pre-Labradorian basin with recrystallized quartz-felspathic rocks from 1650-1637 Ma, likely of felsic plutonic/volcanic origin (Tucker and Gower, 1994; Wasteneys et al, 1997). Pinwarian magmatism is evidenced by foliated granitoid rocks ranging approximately from 1500 to 1450 Ma (Tucker and Gower, 1994; Wasteneys et al., 1997). High-grade Pinwarian metamorphism is recorded in a quartzite with a monazite U-Pb age of 1500 Ma and a quartz-monzonite from migmatite with a zircon U-Pb age of 1450 Ma (Wasteneys et al., 1997).

The PT exhibits extensive Grenvillian pluton emplacement and high-grade pervasive deformation and metamorphism around 1030-1015 Ma (Gower, 2019), along with post-tectonic magmatism between 985-940 Ma (Gower et al., 1988; Gower and Krogh, 2002; Rivers, 2009). Alkaline magmatism is represented by a strongly deformed syenite (991 Ma) and mostly undeformed mafic dykes (985 Ma), highlighting the last significant deformation between 991-985 Ma (Wasteneys et al., 1997). Granitoid plutonism from 974 to 956 Ma marks post-Grenvillian magmatism in this terrane (Gower and Loveridge, 1987; Gower, 1991; Tucker and Gower, 1994).

1.3 Local Geology

The study area in Southeast Labrador lies within the southeastern extension of either the LMT or MMT, depending on the model (e.g., Gower 2005, 2019, cf. Hanmer and Scott, 1990; Scott et al.,1993). It is situated immediately north of the LHsz and south of the FHsz (Figure 1.3). The 1.3 Ga FHVB, located between these shear zones, features highly deformed amphibolite-facies peralkaline rhyolites and mafic schist hosting REE mineralization (Haley, 2014).

The area includes a variety of medium-to-high-grade metamorphic rocks such as deformed granitoids, volcano-sedimentary sequences, mafic gneiss, and later pegmatites (Haley, 2014; Miller, 2015). These units have undergone one or more deformational phases (Scott et al.,1993) and are described by Gower et al. (1988b) as fine-grained, laminated mylonites grading into lower strain rocks that include monzonite, K-feldspar megacrystic granodiorite, granite, quartz diorite and amphibolite (Figure 1.3). The FHVB was discovered during Search Minerals' 2010 exploration season (Haley, 2014 and references therein) and was therefore not included in the regional maps (Gower et al., 1987, 1988b, 2005). The Total Magnetic Intensity (TMI) map (1:100,000) from Search Minerals highlights linear magnetic anomalies with a northwest trend, aligning with the FHVB (Figure 2.1).

The peralkaline rhyolites of the FHVB are enriched in high field strength elements (HFSE) and classified as pantellerites and comendites due to their high Fe and low Al content (Haley, 2014). The FHVB rocks were deposited at 1.3 Ga in an environment interpreted as

extensional and metamorphosed at ~1.05 Ga (Haley, 2014; Magyarosi and Rayner, 2023). Three distinct REE-mineralized volcanic horizons within the Fox Harbour area with high radiometric and magnetic anomalies are mapped from south to north (Haley, 2014): the South Belt (100-250 m thick), the Magnetite (MT) Belt (20-150 m thick), and the Road Belt (10-50 m thick) (Figure 1.3). Adjacent to these volcanic packages, mylonitic to megacrystic granitic augen-gneiss with concordant amphibolite layers and metagabbroic gneiss are interpreted as either stratigraphic layers that are conformable with the REE-mineralized volcanic package or basement unconformably underlying the deformed packages. The three volcanic belts, with similar textures and elemental signatures, are interpreted to represent a bimodal volcanic sequence (Haley, 2014; Miller, 2015).

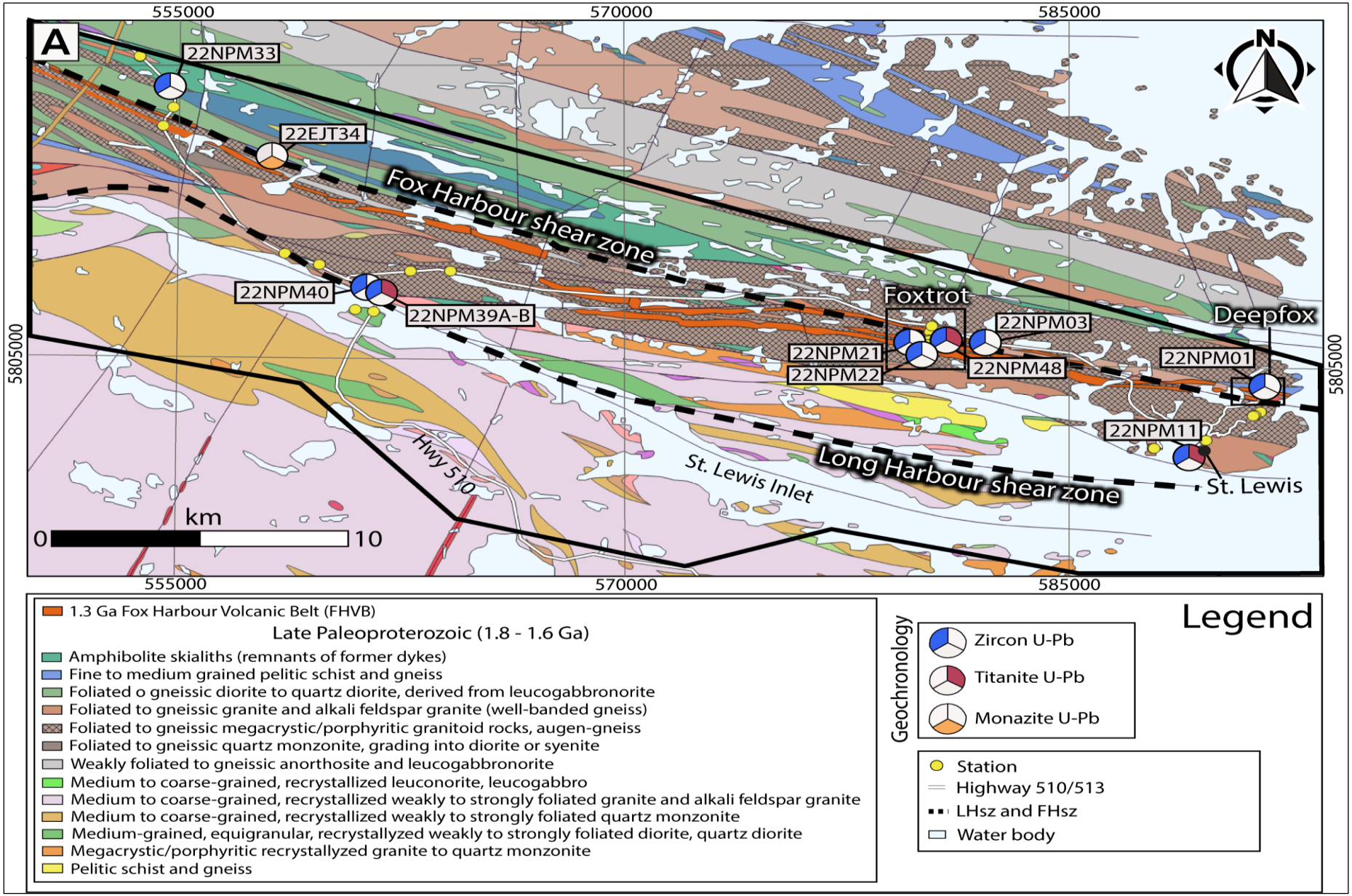

Figure 1.3 *Location study area, St. Lewis—Labrador.* ***A)*** *local geology and main structures (modified from Gower 2005) displaying the Fox Harbour Volcanic Belt mapped by Search Minerals in 2010 (orange); the location of stations and samples collected for U-Pb geochronological analyses (zircon, titanite, and monazite) for this project are also displayed. The Foxtrot and Deep Fox REE deposits were targeted for field analysis herein.*

The southern boundary structure of the FHVB, the LHsz, exhibits pervasive amphibolite-facies ductile deformation along moderate to steeply northwest-plunging extension lineations (40-65°), which suggests a dip-slip component with a north-side-up to the SE, previously interpreted to have formed at 1.6 Ga (Gower, 1985; Hanmer and Scott, 1990; Scott et al., 1993; Gower, 2005). Narrow belts of greenschist-facies mylonite zones, measuring approximately 10 meters in width and extending up to several kilometers in length within the LMT, formed around 1.0 Ga and display shallow (~10°) to moderate southeast-plunging extension lineations (Hanmer and Scott, 1990; Scott et al., 1993). Gower (2005) also documented horizontal-plunging lineations in the FHsz, ranging from N-NE to NW.

1.4 Field Methodology and Interpretation

1.4.1 Sample and Data Acquisition

Fieldwork was conducted in August 2022 near St. Lewis, Labrador, over a two-week period. The approach involved structural mapping and sample collection at strategic locations using existing bedrock and geophysical maps. The objectives were to address the following research questions: i) what is the age and structural style of high-temperature ductile deformation and metamorphism related to the FHVB and surrounding rocks, including the bounding shear zones? ii) what is the structural or stratigraphic relationship between the three distinct mineralized horizons of the FHVB and their host rocks?

Utilizing bedrock maps from Gower 1985; Hanmer and Scott, 1990; Scott et al., 1993 and Gower 2005, along with updated Total Magnetic Intensity (TMI) data from Search Minerals (2010), various tectonic domains and shear zone traces were identified, and interpreted herein (Figure 2.1). This approach provided a basis for collecting structural and geochronological information to address the unresolved scientific questions. The integration of this information with newly acquired field data enabled a comprehensive reinterpretation of these domains.

The newly interpreted domains underwent detailed field observations, with structural and field relationships collected across a 50 x 10 km area covering the FHsz, the FHVB, and the LHsz. Structural data was gathered using a Brunton compass and the FieldMoveClino app on an iPhone 11, which allowed for efficient collection of planar and linear measurements, enhancing the statistical validity of the collected data. Additionally, more than 50 samples were collected and processed into thin sections for petrographic analysis (including 20 oriented thin sections), and 14 samples were taken for U-Pb geochronological studies (zircon, titanite, and monazite).

Chapter 2 Field observations and petrography

2.1 Domain Classification

Based on previous studies (Gower, 1985; Hanmer and Scott, 1990; Scott et al., 1993; Gower, 2005; Haley, 2014) and new geophysical data, the study area is divided into three distinct main domains for further structural analysis: the Pinware domain, the FHVB domain, and the Lake Melville domain. A first-order subdivision of domains is based on their characteristic shear bounding structures and differing magnetic patterns (Figure 2.1).

Pinware domain: This is the southernmost domain considered herein and is part of the more regional PT. In this domain, some of the intrusive bodies exhibit a relatively homogenous high magnetic pattern, while in the northern part, the LHsz (previously mapped by Gower, 1985; Hanmer and Scott, 1990; and Scott et al., 1993) coincides with strike-parallel linear magnetic patterns, delineating the northern boundary of the PT from the southeastern extension of the LMT (Scott et al., 1993) or the MMT (Gower, 2005).

FHVB domain: This newly defined domain herein is regionally associated with either the LMT or the MMT. It is situated north of the LHsz and displays NW-striking rock units and parallel, elevated magnetic anomalies that highlight the three distinct REE-mineralized horizons of the 1.3 Ga FHVB. In the southern part of the FHVB domain, strike-slip structures (Scott et al., 1993; Gower, 2005) align with magnetic lineaments that are spatially related to the LHsz. One of these lineaments parallels the main LHsz, and is well

exposed along the shoreline of St. Lewis (Figure 2.1) and is herein called the St. Lewis shear zone (SLsz).

Lake Melville domain: This domain encompasses the LMT, is north of the FHVB domain, and displays broad NW-striking linear low-intensity magnetic anomalies, which suggest a distinct geological environment to domains to the south. The southernmost low magnetic pattern corresponds to the FHsz, previously mapped by Gower, 2005, which separates the FHVB domain from the LMT. All these structures and domains are intersected and displaced by late N-NE brittle faults, as evident in the offsets highlighted by the geophysical data; these are beyond the scope of this thesis and not discussed in further detail.

2.2 The FHVB Domain

The FHVB domain exhibits W-NW trending linear high magnetic anomalies, with a Km-scale plunging fold evident in magnetic patterns south of Port Hope Simpson (Figure 2.1A). The FHsz marks its northern boundary, and the LHsz marks the southern boundary. Dominant rock types in the FHVB include Kfs-megacrystic, protomylonitic augen-gneiss interlayered with three mylonitic, steeply dipping tabular REE-mineralized felsic volcanic layers of the 1.3 Ga FHVB (Haley, 2014). Associated with the FHVB are undated Hbl±Cpx±Bt schist with Grt-leucosomes (mineral abbreviations follow the notation by Whitney and Evans, 2010), Grt-bearing leucodiorite, and meter-thick quartzite layers; all of which are intruded by volumetrically minor granitic amazonite-bearing pegmatites that may be ~1024 Ma (e.g., Kamo et al., 2011). Rare screens of metapelite also occur throughout this domain.

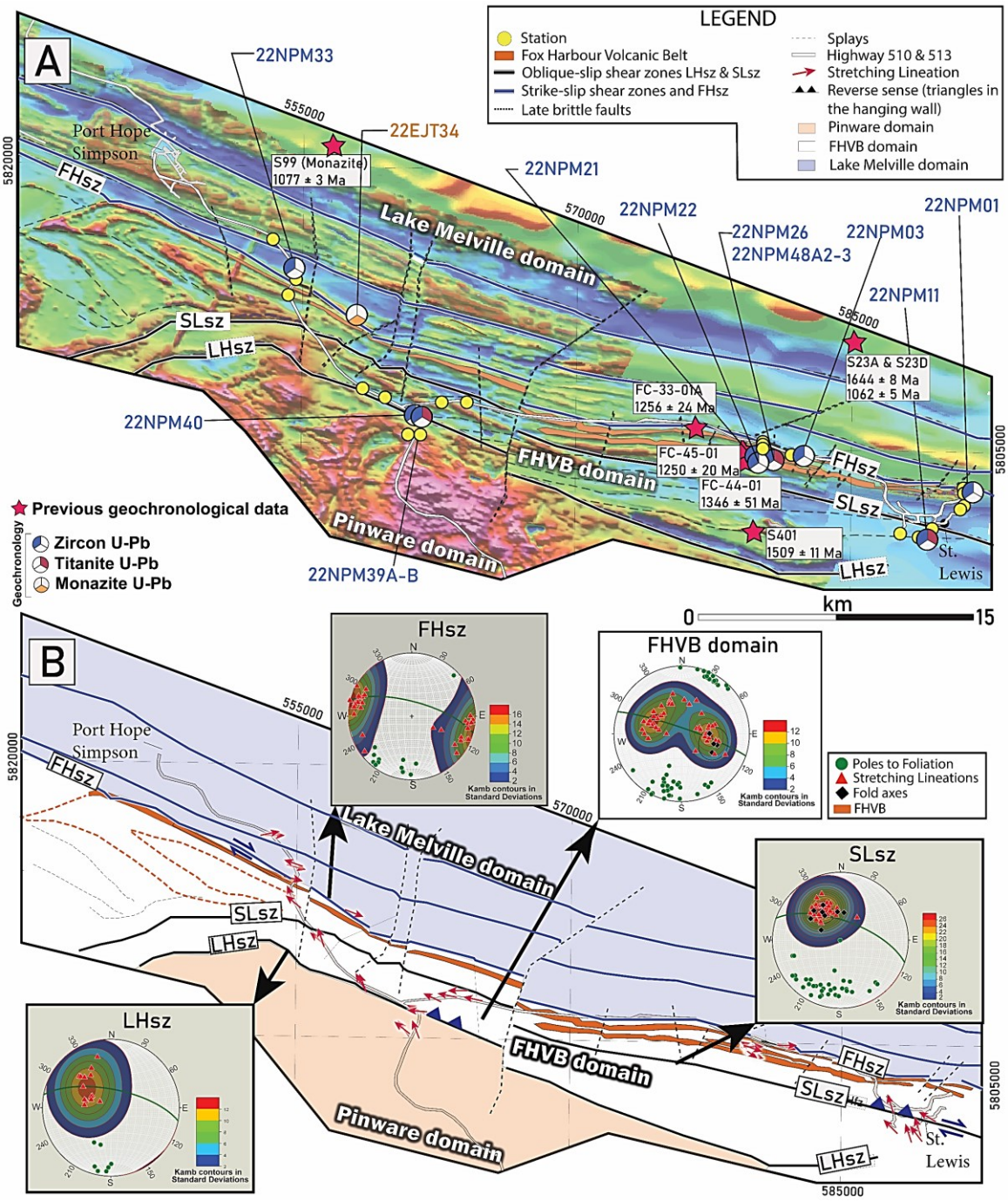

Figure 2.1 A) *New interpretation of domains and traces of structures based on Total Magnetic Intensity Map by Search Minerals. The domain boundary shear zones (LHsz, SLsz, and FHsz), the folded REE mineralized FHVB, Lake Melville, and Pinware domains are displayed. Previous geochronological data locations are shown as red stars (Haley, 2014).* ***B)*** *Simplified map of tectonic domains showing stereograms for each domain: Fox Harbour shear zone (FHsz), St. Lewis shear zone (SLsz), Long Harbour shear zone (LHsz). The orange dashed lines represent likely the folded FHVB interpreted by aeromagnetic signatures, which are truncated by the SLsz and bounded by fault splays.*

All rock types within the FHVB domain exhibit a pervasive tectonic foliation ($S_{1\text{-}FHVB}$) with a mean orientation 289/83 NE (n=43) (Figure 2.2A), defined by interlayering of units, aligned Bt+Amp, stretched Qz+Fsp layers, and layer parallel leucosomes. Within the FHVB, Grt-bearing leucosome in the Hbl+Cpx schist and leucodiorite layers are isoclinally folded (Figure 2.2B) with axial surfaces parallel to the $S_{1\text{-}FHVB}$ foliation. This suggests that the early leucosome-present fabric ($S_{1\text{-}FHVB}$) may represent the peak of metamorphism in the FHVB domain, and a second axial planar fabric ($S_{2\text{-}FHVB}$) formed after leucosome crystallization, forming a parallel composite $S_{1/2\text{-}FHVB}$ foliation. Fold axes ($F_{2\text{-}FHVB}$) within the FHVB rocks plunge moderately eastward (50-108, n=52) while stretching lineations ($L_{2\text{-}FHVB}$), defined by elongated Qz+Fsp in the peralkaline rhyolites, define two maxima towards the east and NW (51-294). Within some folded structures, a ~90° relationship of $L_{2\text{-}FHVB}$ and $F_{2\text{-}FHVB}$ within $S_{1/2\text{-}FHVB}$ foliation is consistent with layer active buckle-folding geometry (Figure 2.2A-B). However, many isoclinal folds exhibit narrowing limbs akin to class 1C or class 2 folds, suggesting homogenous strain affected the earlier buckle folds. The augen-gneiss exhibits a protomylonitic structure where shear plane folia (C plane) run 290/80 parallel to $S_{1/2\text{-}FHVB}$, with δ- and σ-type winged-porphyroclasts and S-C' folia reflecting right-lateral, strike-slip shearing. It is not obvious from field relations if shearing occurred distinctly after buckle-folding or also during active buckling. (Figure 2.2 C-D-E).

2.2.1 Sample Description and Petrography

Despite the FHVB being reported as a bimodal volcanic sequence (Haley, 2014), the ages of the mafic and quartzite components associated with the felsic mineralized rocks are unknown. Furthermore, the metapelite and augen gneiss also remain undated.

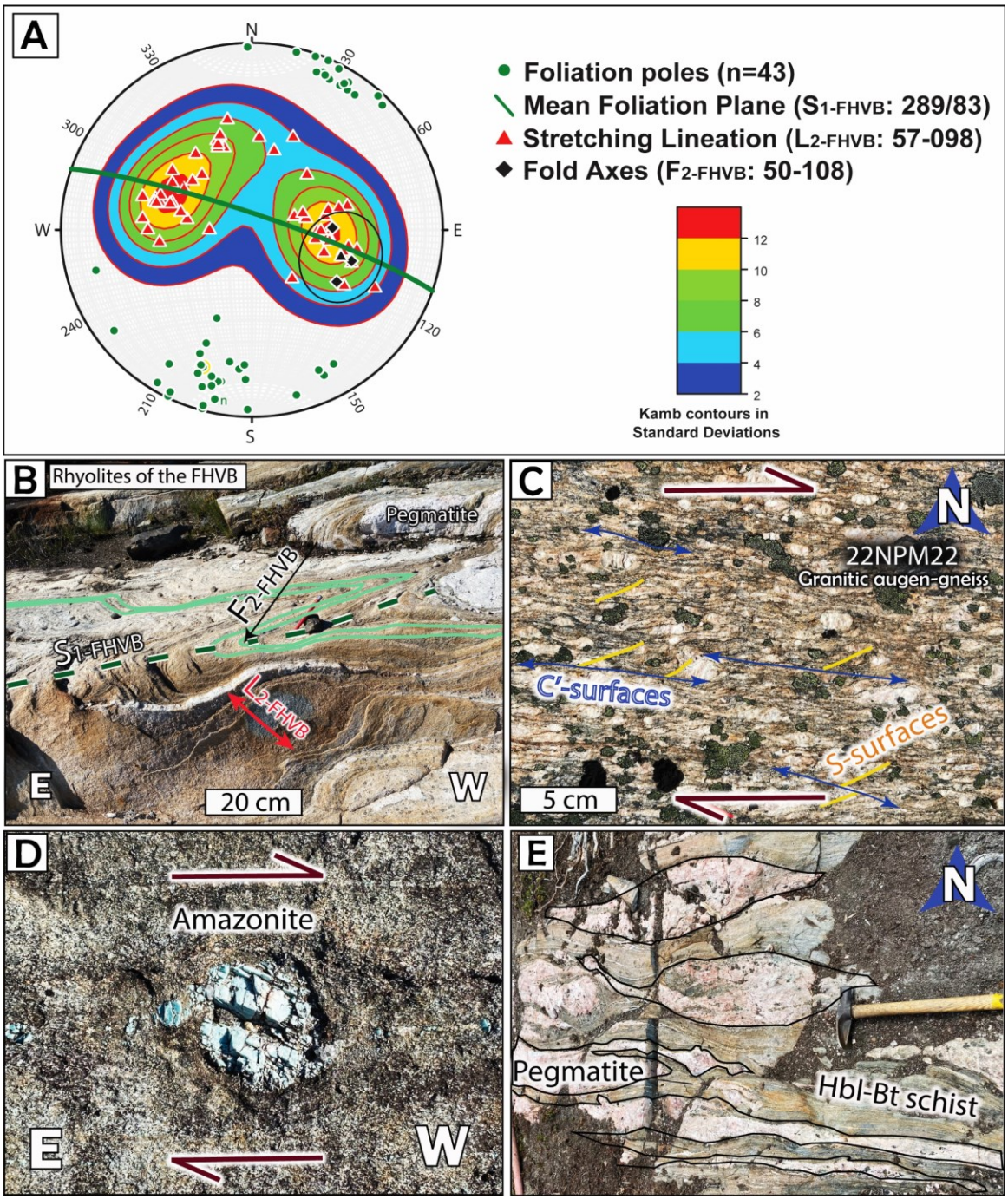

Figure 2.2 A) *Lower hemisphere, equal area stereographic plot of structures from the FHVB domain.* ***B)*** *Highly deformed REE-mineralized rhyolite of the FHVB with* $F_{2\text{-FHVB}}$ *perpendicular to the* $L_{2\text{-FHVB}}$. ***C)*** *S-C' folia in felsic augen-gneiss (22NPM22) showing a dextral shear sense.* ***D)*** *δ-type rotated porphyroclast of teal feldspar (amazonite variety) showing dextral shear sense.* ***E)*** *Asymmetric Boudinage showing subtle right-lateral sigmoids of granitic pegmatite interlayered with Hbl+Bt schist from the FHVB.*

To establish the minimum crystallization ages of the mafic schists and maximum depositional age of the quartzite units, two samples of folded concordant leucodiorite layers (22NPM01 and 22NPM26) and a Grt-bearing leucosome sample (22NPM48A3) were collected from Hbl+Cpx schists (22NPM48A2), along with one presumed quartzite layer (22NPM21) adjacent to the schists (Figure 2.3 and Figure 2.4 A-E). Additionally, the stratigraphic relationship between the FHVB and the augen-gneiss remains untested. To investigate this, two augen-gneiss samples were collected from the northern (22NPM03) and southern (22NPM22) parts of the three mineralized horizons of the FHVB (Figure 1.3 and Figure 2.3).

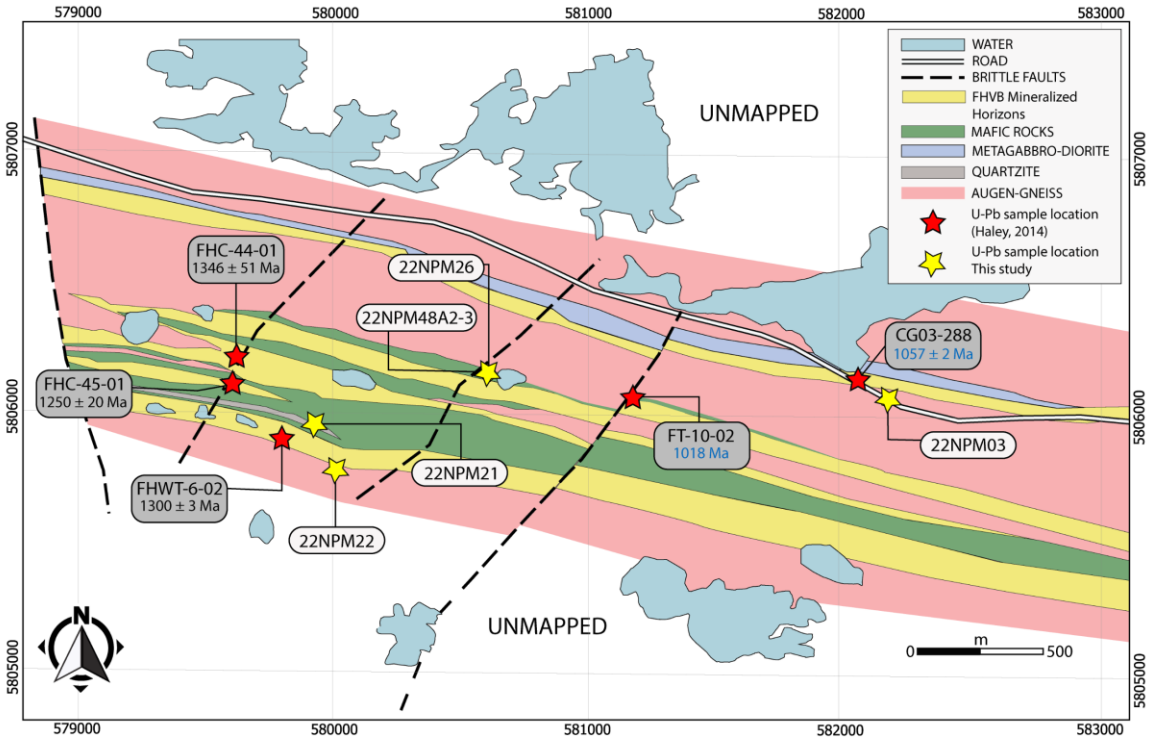

Figure 2.3 *Detailed geological map of the Foxtrot area (modified from Haley, 2014) showing interlayered augen-gneiss rocks (pink) within the three mineralized horizons of the FHVB (yellow). The map highlights the interlayered relationship between dated rhyolites (Haley, 2014) and associated mafic and quartzite layers. U-Pb zircon crystallization ages (black) and metamorphic ages (blue) from Haley (2014) are also displayed.*

The Hbl-Cpx schist displays grey mesocratic to dark melanocratic centimeter-scale bands, primarily composed of Cpx+Pl+Hbl+Ttn_1 and Hbl+Pl+Bt+Ttn_1, respectively, representing compositional or gneissic layering associated with Pl+Qz+Grt+Hbl+Cpx anatectic layers ($S_{1\text{-FHVB}}$) with two generations of titanites. These leucosomes are parallel to $S_{1\text{-FHVB}}$ and folded about $S_{2\text{-FHVB}}$ fabric (Figure 2.4D). Furthermore, this Grt-bearing leucosome (22NPM48A3) is discretely crosscut by non-penetrative late thin <mm sub-planar titanite (Ttn_2) seams, that overprint and run subparallel to $S_{1/2\text{-FHVB}}$. These late Ttn_2 are assumed to have formed post-leucosome crystallization and are tentatively attributed to $S_{3\text{-FHVB}}$ (Figure 2.5D).

Distinct medium-grained metapelites, quartzites, and garnet-amphibolites are located in the northern part of the FHVB domain, near the Fox Harbour shear zone (FHsz) boundary. These rocks are presumably older and do not have clear contact relations with the FHVB rocks (Figure 1.3 and Figure 2.1). Gower (2019) assumed this sequence as pre-Labradorian supracrustal rocks, mapped along the LMT as fine- to medium-grained pelitic schist and gneiss. A pelitic schist exhibits a high-temperature mineral assemblage of Crn+Ms+Grt+Sil+Bt+Mnz (22EJT34, Figure 2.4F). To constrain the metamorphic age, monazite dating was performed in this rock; however, the depositional age was not tested herein and remains uncertain. Detailed sample descriptions and field relationships are as follows:

2.2.1.1 Sample 22NPM22: Granitic augen-gneiss.

This highly deformed granitic augen-gneiss, collected from the southern part of the FHVB (Figure 2.3), is primarily composed of Kfs+Pl+Qz+Amp+Bt in which foliation ($S_{1/2\text{-}}$

$_{FHVB}$) is defined by aligned Amp+Bt crystals. This sample exhibits a right-lateral sense-of-shear in plan view, evidenced by centimetric Kfs+Qz σ-porphyroclasts, along with S-C folia (Figure 2.2C). The presence of randomly oriented Chl+Ep replacing and surrounding the Amp+Bt crystals (Figure 2.5A) suggests a distinct younger metamorphic assemblage (Bt+Chl+Ep+Ser), indicative of greenschist facies conditions. This sample was collected to establish the crystallization age (U-Pb zircon) of the basement rocks interlayered with the mineralized 1.3 Ga FHVB.

2.2.1.2 Sample 22NPM03: Granodioritic gneiss.

This sample is collected from the northern part of the FHVB (Figure 2.3) and consists of highly deformed orthogneiss with leucocratic layers that are aligned parallel to the $S_{1/2\text{-}FHVB}$ foliation. This grey-to-black mylonite displays a smoothly parallel gneissosity defined by Pl+Qz+Bt+Amp+Ttn. The rock is classified as a granodioritic gneiss (Figure 2.4A). The tabular biotite (aligned and defining $S_{1/2\text{-}FHVB}$) is overprinted by Chl+Ep in random orientations, indicating Chl+Ep growth in a hydrated and low differential-stress environment at Chl+Ep grade, indicating a greenschist-facies metamorphism.

Rounded Kfs porphyroclasts exhibit undulose extinction (Ue) and form smaller equant grains of Kfs+Qz (~50 μm) in winged mantles, with smooth grain boundaries and clear triple point textures, preserving evidence for grain size reduction through dynamic recrystallization processes such as Subgrain Rotation (SGR) and Grain Boundary Migration (GBM) during $S_{1/2\text{-}FHVB}$ development. However, mantled regions also exhibit Grain Boundary Area Reduction (GBAR) textures (Figure 2.5B), indicating static recrystallization at elevated temperatures > 600 °C (Trouw and Passchier, 2009). This

sample was collected to establish the crystallization age (U-Pb zircon) of the basement rocks interlayered with the mineralized 1.3 Ga FHVB.

2.2.1.3 Sample 22NPM01: Grt-bearing leucodiorite (Deep Fox).

This rock was collected in the northern segment of the FHVB domain (Figure 1.3 and Figure 2.1) from a highly deformed mafic orthogneiss adjacent to the FHVB rocks, which could be a mafic age equivalent to the bimodal volcanic rocks. The sample represents a folded leucocratic layer that comprises a centimetric gneissic banding (Figure 2.4B). The rock is fine-grained (< 1 mm) and exhibits granular and mylonitic textures. It is composed of Pl+Bt+Amp+Qz+Grt+Ttn and is classified as a Grt-bearing quartz diorite, which displays an anastomosing smooth foliation ($S_{1/2\text{-}FHVB}$) characterized by aligned Bt+Amp crystals, which are overprinted along with Grt by aligned Chl+Ep crystals.

Both Pl+Qz σ-porphyroclasts and elongated (5:1) Qz ribbons exhibit undulose extinction and subgrain formation, preserving evidence for grain size reduction through dynamic recrystallization such as GBM, which is overprinted by internal polygonal granoblastic fabric indicative of static growth (~650 °C, Trouw and Passchier, 2009). This sample was collected in the eastern FHVB to establish the minimum emplacement age (U-Pb zircon) of the mafic gneiss and assess its possible age equivalence to the 1.3 Ga felsic members of the FHVB.

2.2.1.4 Sample 22NPM26: Grt-bearing leucodiorite (Foxtrot)

This sample was collected from a highly deformed fine-grained intermediate layer concordant with melanocratic Hbl-rich and mesocratic Cpx-rich bands in the FHVB mafic

schists (Figure 2.3). The sample exhibits a whitish-weathered surface and a grey colour on a fresh surface (Figure 2.4C). The rock is composed mostly of Pl+Qz+Bt+Hbl+Grt+Ttn and is classified as Grt-bearing leucodiorite.

This leucodiorite is oriented parallel to $S_{1/2\text{-FHVB}}$ in the mafic schist, is tightly folded, and exhibits a foliation defined by aligned Hbl+Bt. Randomly oriented Chl overgrows Hbl+Bt, indicating a younger mineral assemblage grew in a low differential-stress regime. This sample was collected to establish a minimum emplacement age (U-Pb zircon) of the mafic schist in the central FHVB to assess possible age equivalence to the 1.3 Ga felsic members of the FHVB.

2.2.1.5 Sample 22NPM48A2: Mafic schist – Mesocratic Cpx-rich band.

This sample represents the highly deformed, compositionally banded mafic schist. Dark-green bands comprise Cpx+Hbl+Qz+Pl+Ttn, while the grey felsic bands consist of Qz+Pl+Cpx+Ttn (Figure 2.3 and Figure 2.4 D). The alignment of Hbl+Bt+Ttn in this sample is parallel to the compositional banding and defines the foliation $S_{1/2\text{-FHVB}}$.

Clinopyroxene exhibits a basal form with irregular margins and is not aligned, suggesting it retains its primary igneous textures. By contrast, the Hbl+Bt+Ttn in the melanocratic band are aligned and exhibit a tabular and wedge-shaped habit. The Hbl surrounds and replaces some of the Cpx crystals, indicating it is likely a younger mineral associated with retrograde metamorphic processes. Additionally, these Hbl-rich bands spatially envelop the leucosome, a key texture suggesting the leucosomes are in-situ partial melts and the dark layers are restite (Sawyer, 2008), indicating the Hbl-rich bands lost some amount of felsic

material during $S_{1\text{-}FHVB}$ (Figure 2.5C). In-situ U-Pb titanite targets, observed as grains aligned parallel to $S_{1\text{-}FHVB}$ within the three mineralogical bands (Cpx-rich, Hbl-rich, and Qz-rich), were analyzed to determine the timing of metamorphism associated with the restite formation.

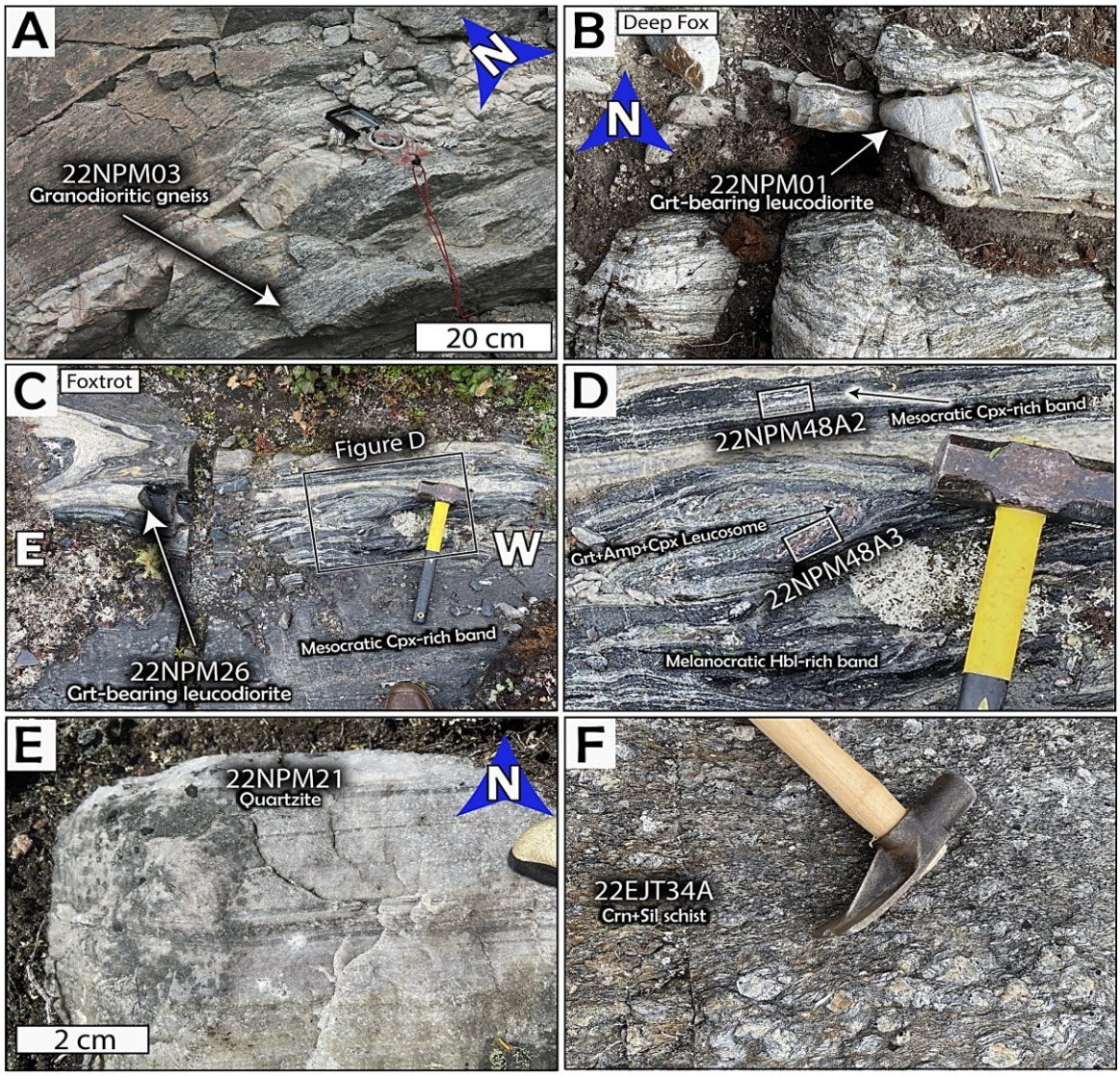

Figure 2.4 *Field photographs of samples from the FHVB domain units analyzed in this study.* ***A)*** *Granodioritic gneiss with some centimetric leucocratic layers parallel to the foliation (22NPM03);* ***B)*** *Folded concordant layer of Grt-bearing leucodiorite in the Foxtrot area (22NPM01).* C) *Outcrop of the Hbl+Cpx schist in the Foxtrot area with folded concordant layers of Grt-bearing leucodiorite (22NPM26) and mesocratic Cpx-rich band. Inset figure D.* ***D)*** *Folded Grt-Amp+Cpx+Qz leucosome within the mafic schist in the Foxtrot area, showing the location of the thin section 22NPM48A2 (Mesocratic band) and 22NPM48A3 (leucosome + Melanocratic band).* ***E)*** *Quartzite layer in the Foxtrot area. F) Outcrop of Crn+Sil schist (22EJT34A), observe the white, beige centimetric Crn porphyroclasts, which are mostly replaced by Ms.*

2.2.1.6 Sample 22NPM48A3: Grt-Hbl-Cpx+Pl+Qz leucosome.

This thin section features part of an anatectic layer primarily composed of Grt+Hbl+Cpx+Pl+Ttn and a part of the restite with a mineral assemblage of Hbl+Pl+Bt+Ttn, with aligned Hbl+Ttn parallel to the $S_{1/2\text{-FHVB}}$ foliation (Figure 2.4D). Clinopyroxene in the anatectic layer is observed as inclusions within the garnet and is replaced by hornblende (Figure 2.5D), suggesting that Grt+Hbl is consuming Cpx during leucosome development. This leucosome contains zircon grains targeted for in-situ U-Pb dating to obtain a crystallization age of the leucosome and peak metamorphism.

Titanite is aligned parallel to $S_{1/2\text{-FHVB}}$ in the gneissic banding and the leucosome. However, late seams of titanite (~100 µm width) crosscut and intersect the garnets in the leucosome and Hbl-rich band, running parallel to the foliation $S_{1/2\text{-FHVB}}$ but formed post-$S_{2\text{-FHVB}}$ in more localized, discrete bands ($S_{3\text{-FHVB}}$; Figure 2.5D). To understand the timing of deformation in-situ titanite U-Pb and trace elements analyses were conducted in titanite crystals aligned with $S_{1/2\text{-FHVB}}$ in the Amp-rich band (Ttn_1) and the late titanite seams $S_{3\text{-FHVB}}$ (Ttn_2).

2.2.1.7 Sample 22NPM21: Quartzite.

This sample represents a presumed quartzite (Figure 2.4E) interlayered with the FHVB and the mafic schist (Figure 2.3). The rock is composed of Qz+Pl+Ms+Bt and exhibits a steep foliation parallel to $S_{1/2\text{-FHVB}}$ defined by aligned muscovite and stretched quartz crystals. The rock is fine-grained with quartz grains with straight-grain boundaries and elongated (6:1) monocrystalline ribbons product of subgrain rotation and surrounded by smaller (50 µm) quartz bulges (BLG) (Figure 2.5E). However, these dynamic

recrystallization microstructures are largely overprinted by later GBAR polygonal static recrystallization textures, characteristic of medium-to-high-temperature mylonites forming between 500 and 650° C (Trouw and Passchier, 2009). This sample was collected for detrital zircon analysis to test for depositional age equivalence to the FHVB.

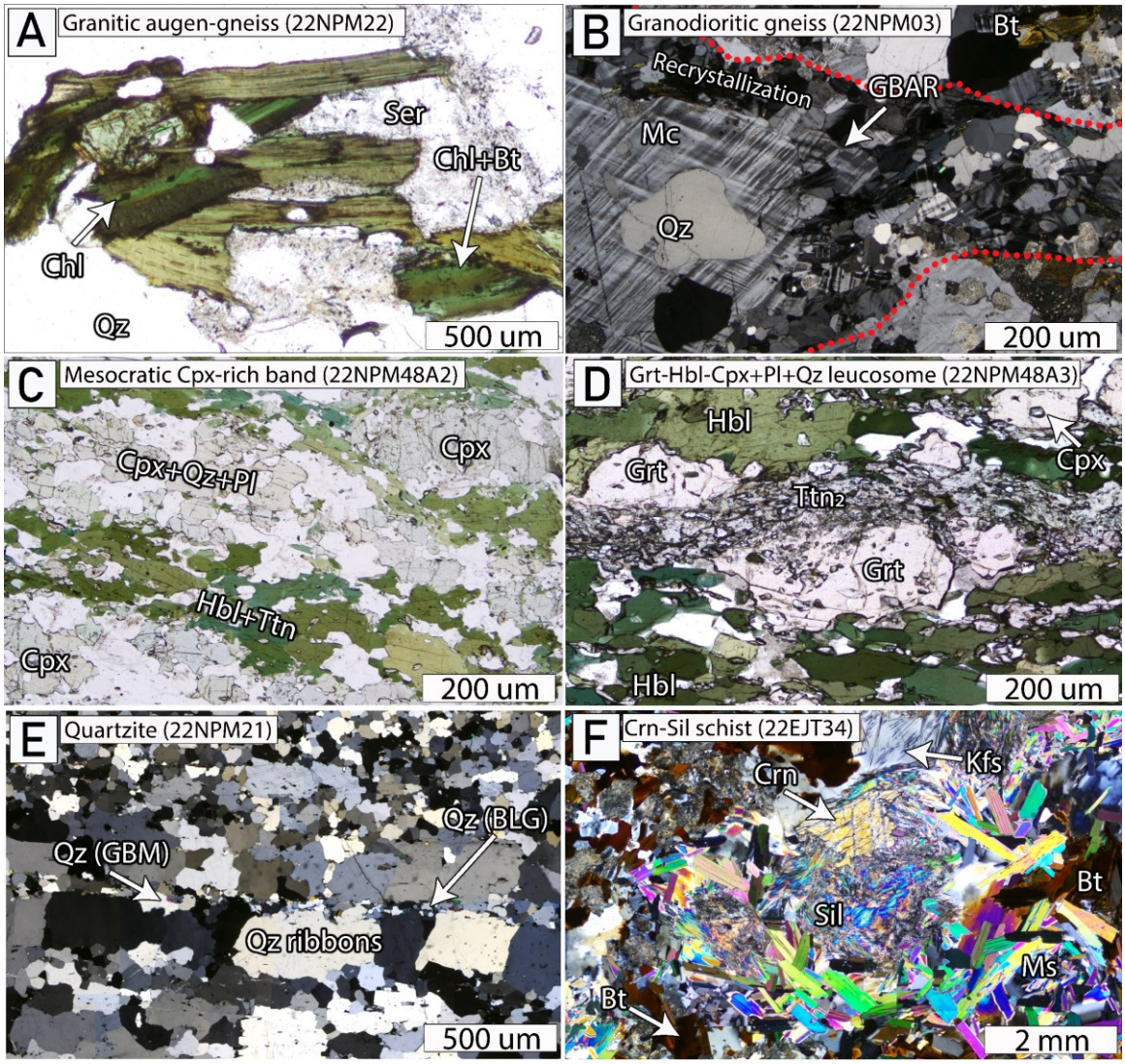

Figure 2.5 A) *Aligned-Bt is replaced by Chl in the augen-gneiss, and Ser replaces Pl, indicating a retrograde event.* ***B)*** *Medium-grade mylonitic augen-gneiss showing microcline porphyroclast mantled by 50 µm size recrystallized Kfs and some Qz overprinted by static recrystallization (GBAR).* ***C)*** *Cpx-rich mesocratic band in mafic schist displaying subhedral unaligned clinopyroxene crystals, and Hbl-rich melanocratic band exhibiting the aligned Hbl+Ttn* $S_{1/2\text{-}FHVB}$. ***D)*** *Discrete veinlets of* Ttn_2 *cross-cutting the Grt+Cpx+Hbl+Pl leucosome, indicating a deformational event post-leucosome folding.* ***E)*** *Quartzite showing elongated ribbons with static recrystallization overprinting grain boundary migration, and bulging textures.* ***F)*** *Millimetre-sized Crn crystal surrounded by randomly oriented Sil, which is overprinted by euhedral tabular Ms.*

2.2.1.8 Sample 22EJT34: Crn-Sil schist.

The sample collected from the northern boundary of the FHVB domain with the FHsz (Figure 1.3 and Figure 2.1), shows no clear contact relationships with the FHVB or the augen-gneiss. The rock exhibits brown to grey weathering colour, medium to coarse-grain texture, and is composed of Crn+Ms+Bt+Grt+Sil+Pl+Qz (Figure 2.4F). The rock displays centimeter-sized Crn+Grt porphyroblasts with a light green hue, where randomly oriented sillimanite partially replaces small, resorbed corundum cores, suggesting high-temperature metamorphism consistent with the amphibolite-facies (sillimanite zone). The foliation ($S_{1\text{-FHVB}}$), defined by coarse-grained aligned biotite, wraps around the Crn-Sil porphyroblasts. Additionally, muscovite replacing sillimanite indicates retrograde cooling and hydration during the latest foliation development, possibly $S_{2\text{-FHVB}}$ (Figure 2.5F). The sample 22EJT34 was collected for U-Pb monazite to determine the timing of regional metamorphism from a non-FHVB pelitic rock.

2.3 The Long Harbour shear zone (LHsz)

The LHsz is defined by a northwest-trending magnetic lineament at the northern edge of the Pinware domain; the LHsz curves SW along strike to the west and spans over 50 km in the study area (Figure 2.1). With the aid of new magnetic maps (Search Minerals, 2010), the newly interpreted LHsz trace suggests a slight modification from previous interpretations (Scott et al., 1993; Gower, 2005), which placed the LHsz 2-3 km northward of the St. Lewis Inlet with an EW-strike (Figure 1.3). This shear zone was examined along the Trans-Canada highway, near the St. Lewis Inlet, from Wood Island to Port Hope Simpson (Figure 2.1).

Relative to adjacent domains, the LHsz exhibits higher strain intensity, a consistent foliation attitude, and a discrete linear magnetic signature, suggesting the LHsz foliation likely represents a transposition foliation which may be younger than the FHVB domain, where no earlier fabrics are visible. This presumed distinct age and fabric style in the LHsz is referred to herein as $S_{T\text{-}LHsz}$. Moderate to steep stretching lineations ($L_{T\text{-}LHsz}$) are defined by stretched Qz+Pl in the mylonitic orthogneiss, with a mean orientation of 49-309 (Figure 2.6A). Viewing the X-Z sense-of-shear plane, asymmetric Kfs σ-porphyroclasts show dextral shear or a north-side-up to the south (reverse) movement (Figure 2.6C).

The LHsz consists of interlayered medium to coarse-grained mafic and intermediate mylonitic orthogneiss, characterized by gneissic banding with centimetric dark bands of Amp+Bt and light bands of Pl+Qz+Kfs. These bands define a consistent gneissic foliation with a mean attitude of 281/68 (Figure 2.6A-B and Figure 2.7A). These orthogneisses exhibit stretched Qz+Pl crystals with rounded and lobate margins, indicative of an igneous protolith modified by deformation. The quartz grains exhibit undulose extinction and irregular serrated boundaries (GBM), indicative of dynamic recrystallization processes, overprinted by polygonal shapes indicating static recrystallization (GBAR) (Figure 2.7C). Mica-rich orthogneiss varieties feature Amp+Pl+Qz+Bt+Ms+Chl, with Bt and Ms bands crosscutting earlier weakly aligned amphibole fabrics ($S_{T\text{-}LHsz}$). Amphibole-rich orthogneiss shows Amp+Bt+Ttn defining the $S_{T\text{-}LHsz}$ foliation, which are replaced by randomly Chl+Ep+Aln+Czo with sericitized plagioclase indicating greenschist-facies conditions (Figure 2.7B).

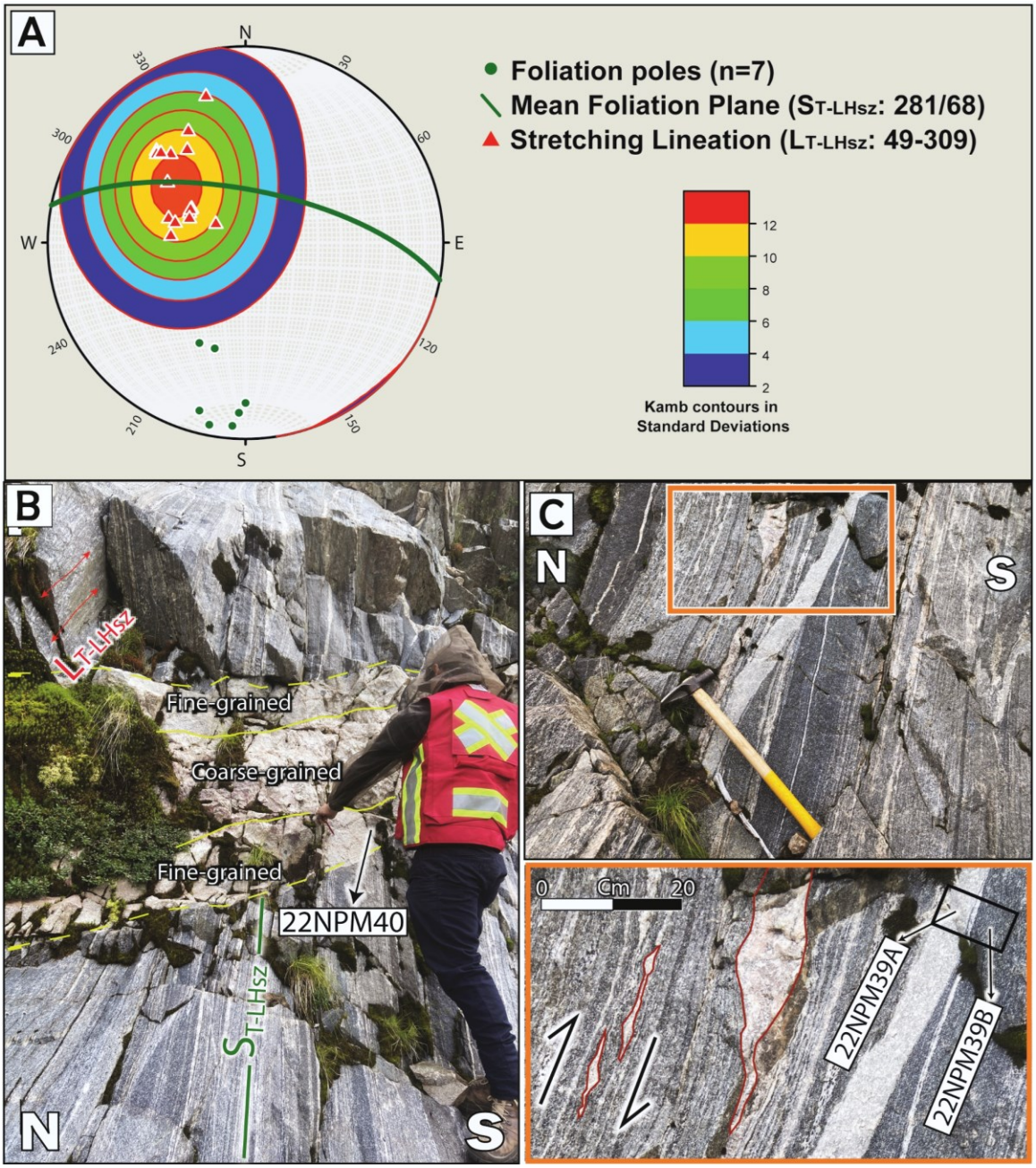

Figure 2.6 A) *Stereoplot of the Long Harbour shear zone displaying the mean foliation plane* $S_{T\text{-}LHsz}$ *(281/68) that encompasses moderate stretching lineations* $L_{T\text{-}LHsz}$ *(49-309);* ***B)*** *The granodioritic gneiss intruded by a meter-wide undeformed felsic dyke; this dyke exhibits a grain size variation from coarse at the center to fine-grained at the outer border;* ***C)*** *a 10 cm-wide quartz monzonitic aplitic dyke, which cuts the mylonite and contains* $S_{T\text{-}LHsz}$ *parallel foliation. The inset represents the zoom-in of the outcrop, showing a north side up to the south shear.*

The $S_{T\text{-}LHsz}$ foliation in the host rock is crosscut by syn-to-post deformational granitic dykes, which range from fine to coarse-grained in texture (Figure 2.6C). Some 15-20 cm thick oblique dykes exhibit similar fabric development as $S_{T\text{-}LHsz}$ foliation and $L_{T\text{-}LHsz}$, suggesting syn-deformational emplacement. Additionally, late undeformed, pink fine- to pegmatitic felsic dykes cut through the main $S_{T/2\text{-}LHsz}$ foliation (Figure 2.6B). They are not internally deformed, suggesting post-deformation emplacement.

2.3.1 Sample Description and Petrography

Three samples were collected to determine the crystallization age of the protolith and the age of shearing within this structure. Sample 22NPM39B was collected from the orthogneiss to determine the crystallization (U-Pb zircon) and deformational age (U-Pb titanite) of the host rock; sample 22NPM39A was gathered from a syn-deformational dyke to ascertain the syn-deformation age (U-Pb zircon). Finally, a sample (22NPM40) was obtained from the post-deformational felsic dyke to establish the crystallization age and to constrain a minimum age when deformation ceased within this shear zone (Figure 2.6B).

2.3.1.1 Sample 22NPM39B: Granodiorite gneiss

This sample is a medium to coarse-grained rock characterized by distinct centimetric gneissic and mylonitic banding with granoblastic texture at the microscale. The dark bands are composed of Amp+Bt+Pl with accessory minerals Aln+Ttn+Ap+Ep. Subhedral amphibole crystals exhibit a prismatic habit in these dark bands, while euhedral tabular Bt+Ttn aligns with the $S_{T\text{-}LHsz}$ foliation. A second textural phase of randomly oriented secondary minerals such as Aln+Chl+Ep+Ser replace and surround the borders of

the aligned amphiboles and feldspar crystals of $S_{T\text{-}LHsz}$ (Figure 2.6B and Figure 2.7B). Zircon was dated in the granodiorite gneiss (22NPM39B) to obtain protolith ages, while titanite was analyzed to attain syn-deformation ages for amphibolite to greenschist-facies shearing.

2.3.1.2 Sample 22NPM39A: Syn-deformational quartz-monzonitic dyke.

The rock is fine-grained with a granular texture and is mostly composed of Kfs+Pl+Qz+Bt+Ms. It is classified as a quartz monzonite with interlaminated euhedral-aligned Bt+Ms tabular crystals, which define a foliation parallel to $S_{T\text{-}LHsz}$. Chl+Ep+Zo crystals are observed surrounding and replacing the biotite, likely a product of hydration reactions. Quartz grains exhibit undulous extinction and incipient GBM overprinted by polygonal static recrystallization GBAR (Figure 2.7C), indicating deformation in this quartz monzonitic dyke. Zircon was targeted in this dyke to obtain a crystallization age-related to syn-deformational shearing.

2.3.1.3 Sample 22NPM40: Post-deformational monzogranitic dyke.

The sample represents a fine to medium-grained rock collected near the margin of a 70 cm wide monzogranitic dyke (Figure 2.6B). The rock displays holocrystalline and graphic textures with subhedral to euhedral interlocking Kfs+Pl+Qz+Bt+Ms and accessory Ttn+Aln+Py+REE carbonates. Bt+Ms are partially replaced by Chl+Ep. Plagioclase displays polysynthetic twinning and perthitic texture with myrmekitic intergrowth, indicating slow cooling from high temperatures and subsequent exsolution of feldspar phases (Winter, 2014). Equigranular quartz grains (~400 μm) are anhedral with undulous extinction and some fractures (Figure 2.7D). This sample was analyzed using U-Pb zircon

dating to determine the crystallization age of the dyke and to constrain a minimum age of cessation of deformation in the LHsz.

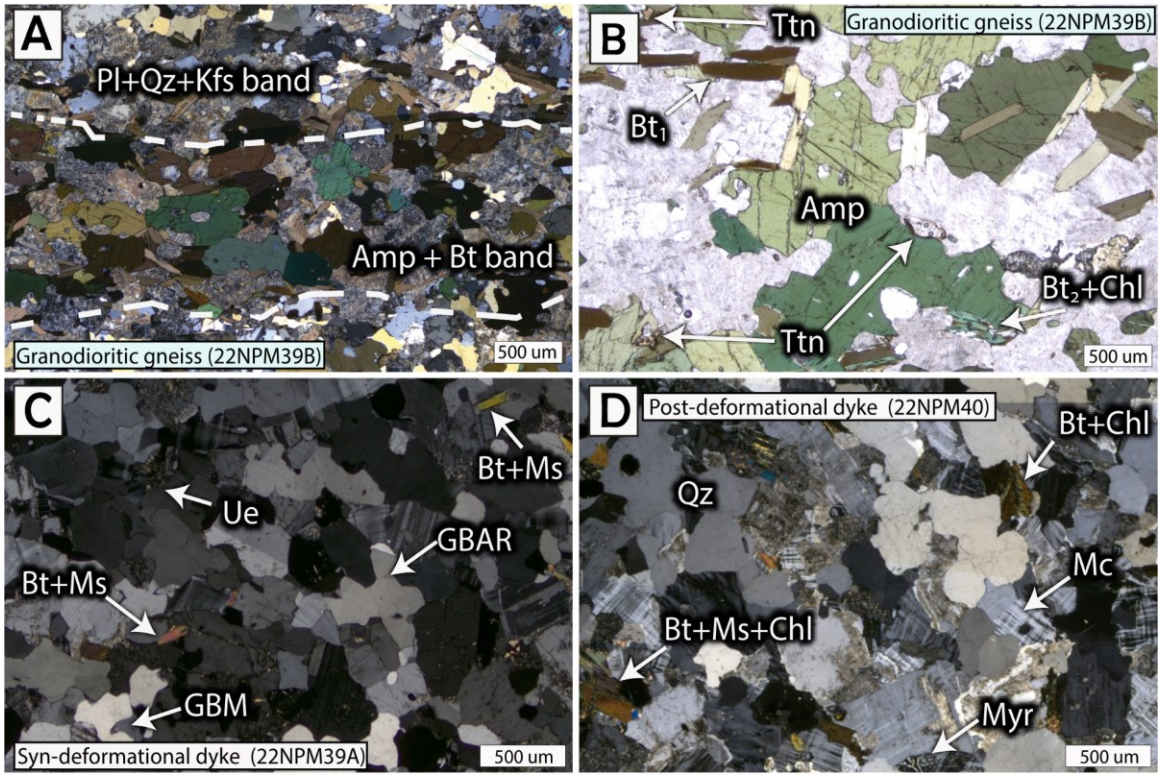

Figure 2.7 A) *Granodioritic gneiss (sample 22NPM39B), exhibiting the mafic and felsic gneissic bands where mafic bands are comprised of Amp+Bt+Ttn and the felsic bands by Pl(Ser)+Qz+Kfs.* ***B)*** *Titanite crystals are at the edge of the amphibole and biotite, which is aligned with the* $S_{T\text{-}LHsz}$ *foliation.* ***C)*** *Syn-deformational quartz-monzogranitic dyke exhibiting Carlsbad twinning in feldspar (center of the image) and deformed Qz crystals with Ue, and GBM overprinted by static recrystallization GBAR.* ***D)*** *Post-deformational felsic dyke, consisting of fine-grained, equigranular quartz, feldspar (microcline twining Mc) exhibiting a holocrystalline and perthitic texture with myrmekitic overgrowing.*

2.4 The St. Lewis shear zone (SLsz)

This structure runs parallel to and is situated 2 km north of the LHsz, characterized by linear magnetic patterns extending over 60 km along the strike. Towards the St. Lewis coastline, the SLsz trace becomes more diffuse, displaying a broad low magnetic anomaly south of the FHVB domain with some low linear magnetic anomalies that bifurcate in the central part between the LHsz and the SLsz (Figure 2.1). The SLsz linear anomaly could

indicate a splay or en-echelon parallel shear structure related to the LHsz, but the exact relationship remains unclear. Gower (2005) mapped a portion of this structure as a strike-slip splay of the LHsz, connecting with the LHsz southwest of St. Lewis (Figure 1.3). However, new geophysical data reveal that the LHsz and SLsz are distinct linear magnetic features separated by FHVB domain magnetic patterns, and this relationship continues along strike within the study area (Figure 2.1).

The rocks outcropping along the St. Lewis coast consist of mylonitic to ultra-mylonitic granodiorite intercalated with mafic schist dykes and pelitic rocks. This granodiorite serves as the main host rock of the shear zone and exhibits a foliation defined by layers of Bt+Ms, alongside millimetric Kfs+Qz porphyroclasts. These minerals define a localized mylonitic foliation $S_{T\text{-}SLsz}$ with a mean attitude of 289/66. Moderate to steep $L_{T\text{-}SLsz}$ stretching lineations (48-330) are defined by Qz+Fsp within the shear plane, plunging northwest, and parallel to the measured fold axes (53-328) of the tight folds $F_{T\text{-}SLsz}$. (Figure 2.8A-C).

Viewing the X-Z sense-of-shear plane perpendicular to the stretching lineation, some sigmoids, and σ-type porphyroblasts composed of Qz+Fsp+Ep display a top-to-the-southeast reverse shear sense (Figure 2.8D). Additionally, the shear zone in the St. Lewis shoreline exhibits centimeter-scale elongated and closed sheath folds when viewed down the fold axis and stretching direction. This suggests high finite simple shear strain in a northwest-plunging direction (Figure 2.8E). The top-to-the-southeast reverse-sense of movement is supported by microstructures where S-C folia display a north-side-up movement evident in some Qz+Ms schist and Amp+Bt schist (Figure 2.9E-F).

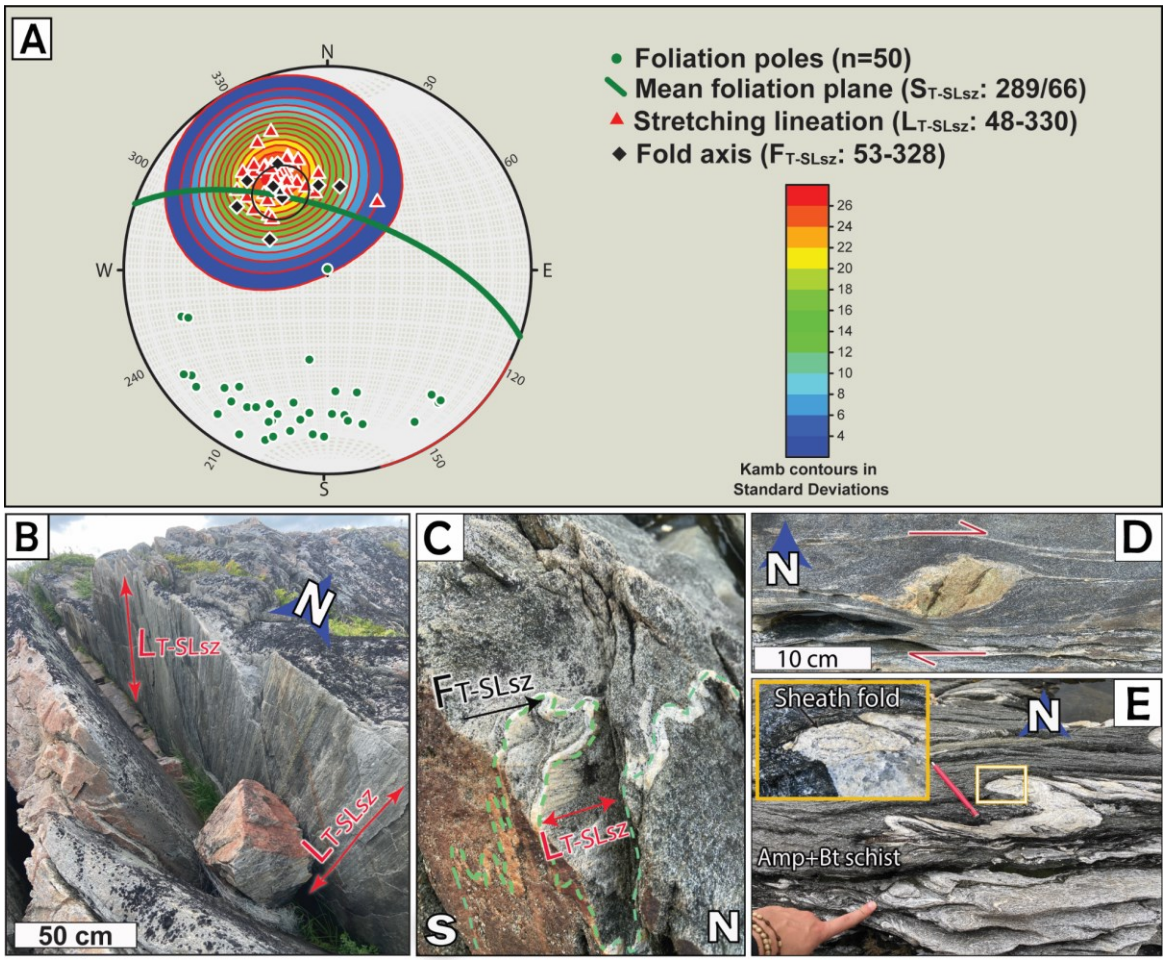

Figure 2.8 A) *Stereoplot of structures in the St. Lewis shear zone displaying the mean foliation plane $S_{T\text{-}SLsz}$ (289/66) that encompasses steep stretching lineations $L_{T\text{-}SLsz}$ (48-330) parallel to the fold axes $F_{T\text{-}SLsz}$ (53-328).* ***B and C)*** *Moderately to steeply plunging stretching lineations $L_{T\text{-}SLsz}$ defined by Qz+Fsp plunging NW parallel to the ptygmatic and tight to closed fold axes $F_{2\text{-}SLsz}$.* ***D)*** *σ-type porphyroclast composed of feldspar and plagioclase with epidote showing a right-lateral shear-sense.* ***E)*** *vertical centimetric elongated eye structures in some granitic folded layers indicating a near vertical movement.*

The Qz+Ms schist displays a continuous foliation ($S_{T\text{-}SLsz}$) with a lepidoblastic texture defined by Ms and Qz microlithons in a spaced schistosity exhibiting incipient undulose extinction and deformation lamellae overprinted by polygonal static recrystallization (500-600°C) (Figure 2.9E). The Amp+Bt schist, on the other hand, features a fine-grained nematoblastic texture with elongate and tabular Amp+Bt bands (cleavage domains) separated by Pl+Qz microlithons. These domains transition discretely, with banding

averaging 100 μm in width, and exhibit replacement by Chl+Ser+Ep, indicating potential retrograde metamorphism or hydrothermal alteration overprinting earlier reverse-sense fabrics $S_{T\text{-}SLsz}$ (Figure 2.9F).

2.4.1 Sample Description and Petrography

Sample (22NPM11) was collected at the St. Lewis coastline to determine the crystallization age of the mylonite protolith by U-Pb zircon and deformational age by U-Pb titanite.

2.4.1.1 Sample 22NPM11: Mylonitic granodiorite

This sample represents a mylonitic grey-to-black rock composed of Pl+Qz+Kfs+Bt±Amp, exhibiting millimetric to centimetric Kfs porphyroclasts. The rock exhibits a continuous foliation ($S_{T\text{-}SLsz}$) at the thin section scale with lepidoblastic texture defined by subhedral-aligned Bt+Ttn, and by millimetric layers of Pl+Qz crystals. Biotite shares irregular grain boundaries and is overprinted and surrounded by un-aligned Chl+Ep, while sericite replaces some Pl+Kfs (Figure 2.9A). Furthermore, titanite defines winged δ-porphyroclasts (0.2-0.5 μm size) in the $S_{T\text{-}SLsz}$ foliation exhibiting a brown core and a lighter rim (10-50 μm size) with asymmetric Bt+Qz wings displaying a north side up to the southeast movement (Figure 2.9A-B).

The quartz grains in this sample exhibit undulose extinction and dynamic recrystallization microstructures, such as possible GBM, overprinted by static polygonal recrystallization GBAR (Figure 2.9B) in elongated, tabular Qz ribbons with polygonal crystalloblastic fabric (Figure 2.9C). Furthermore, Kfs porphyroclasts exhibit dynamic recrystallization and grain size reduction in Qz+Kfs grains (~50 μm size) near the rims of the porphyroclasts (Figure

2.9D), resulting from dynamic recrystallization that shows polygonal textures overprinted (GBAR). These Qz+Fsp microstructures are typical of medium to high-temperature mylonites (500-600 °C), as described by Trouw and Passchier (2009).

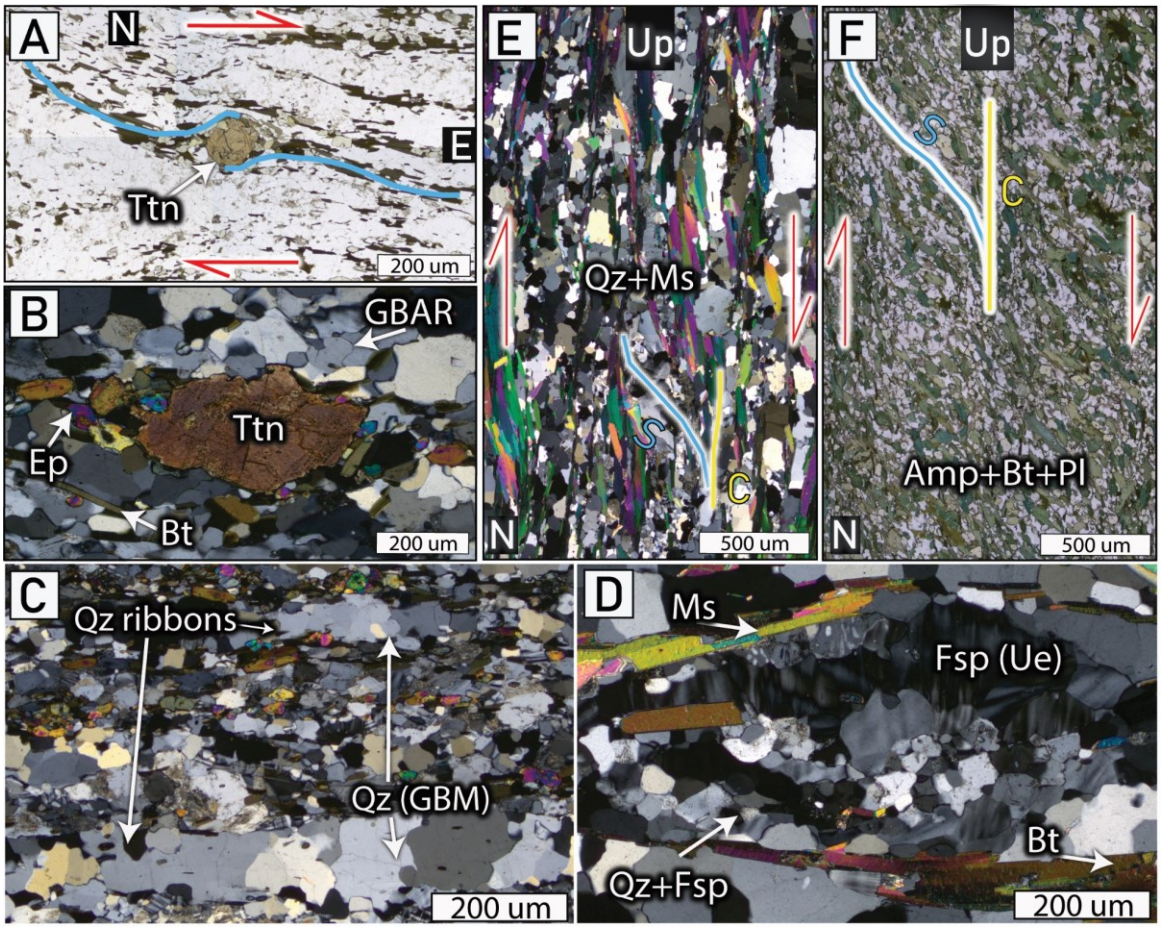

Figure 2.9 *Petrographic and microstructural relations in the St. Lewis shear zone.* ***A)*** *Rotated δ-porphyroclasts of Ttn within the mylonitic granodiorite, showing a dextral sense movement.* ***B)*** *Quartz grains with polygonal static recrystallization overprinted (GBAR), Ttn porphyroclast and Bt+Ep defining the foliation* $S_{T\text{-}SLsz}$. ***C)*** *Quartz ribbons with polygonal granoblastic texture, resulting from static grain growth overprinting microstructures in medium to high-temperature mylonitic granodiorite.* ***D)*** *Fsp porphyroclast showing undulose extinction and deformation lamella surrounded by aligned Ms+Bt+Qz.* ***E and F)*** *Qz+Ms and Amp+Bt schists with S-C folia exhibiting a north-side-up to the southeast, reverse-sense movement.*

The mylonite exhibits alteration minerals such as Ms+Chl+Ep+Ser overprinting but aligned within the $S_{T\text{-}SLsz}$ foliation. This indicates retrograde greenschists-facies conditions at lower temperatures (~300-400 °C) within the same kinematic framework as $S_{T\text{-}SLsz}$. This

mylonitic granodiorite was collected to perform U-Pb zircon geochronology to obtain crystallization ages of the protolith and in-situ U-Pb titanite dating to constrain the amphibolite- to greenschist-facies deformation.

2.5 The Fox Harbour shear zone (FHsz)

The FHsz is the boundary structure between the FHVB domain and the LMT to the north. It displays ~ 50 km wide NW-trending low magnetic anomaly from Port Hope Simpson to St. Lewis. This feature aligns parallel to and is presumed to be linked with the other NW-trending magnetic anomalies of the LMT (Figure 2.1). Rocks near the FHsz trace along Highway 510 consist of gneissic diorite to gabbro, fine to medium-grained Bt schist, granitic pegmatites, and remnants of amphibolitic mafic dykes, all with pervasive foliation development and high finite strain. Given the intense strain and low magnetic signature, the FHsz foliation likely represents a transposition foliation that may also be younger, overprinting earlier structures of the FHVB domain and the LMT. However, the relationship of the deformation history between the FHsz and the LHsz/SLsz remains unclear.

The attitude of the mean mylonitic foliation plane ($S_{T\text{-}FHsz}$) depicted in the stereographic projection is 285/71. The mylonitic rocks of the FHsz display distinct sub-horizontal stretching lineations ($L_{T\text{-}FHsz}$), oriented at 03-105 and 03-285 (Figure 2.10A-B), where elongated and oriented amphibole defines the $L_{T\text{-}FHsz}$ and locally forms L/S-tectonites in the Amp-tonalites with elongation direction 10-102 (Figure 2.10C). In plan view, the sense-of-shear plane (X-Z) shows a dextral shear from feldspathic sigmoids within the granitic mylonitic rocks (Figure 2.10D). Additionally, local zones of high finite

strain exhibit sheath folds when viewed parallel to the prominent, near-horizontal stretching lineation $L_{T\text{-}FHsz}$ (Figure 2.10E). Deformed mafic dykes intrude the orthogneiss host rock, including a Cpx+Amp+Grt dyke, which is crosscut by an aphanitic dyke containing Amp+Bt+Ttn (Figure 2.1 and Figure 2.10B and F).

2.5.1 Sample Description and Petrography

In the FHsz, the granodioritic host rock displays an $S_{T\text{-}FHsz}$ foliation defined by Pl+Qz+Bt+Amp+Ttn (Figure 2.10E) and exhibiting compositional banding defined by Amp+Bt and Qz+Pl microlithons. Elongated quartz grains (3:1) in tabular ribbons display a polygonal crystalloblastic texture with incipient bulging recrystallization along lobate contacts, forming smaller grains (Figure 2.11A). Additionally, myrmekitic intergrowths of quartz and feldspar are observed adjacent to some Kfs porphyroclasts (Figure 2.11B). These textures are characteristic of medium to high-temperature mylonites, ranging from 500-600 °C. However, mineral overgrowths of Chl+Ser+Ep+Ttn are observed replacing the aligned biotite and plagioclase (Figure 2.11C), indicating retrograde greenschist-facies metamorphism.

Samples from two deformed mafic dykes transecting the dioritic orthogneiss were collected to ascertain their crystallization or deformation ages (Figure 2.10F). Although zircon grains were not recovered from the Grt-bearing dyke, they were successfully obtained from the Amp+Bt+Ttn dyke. The detailed description of this sample (22NPM33) is as follows:

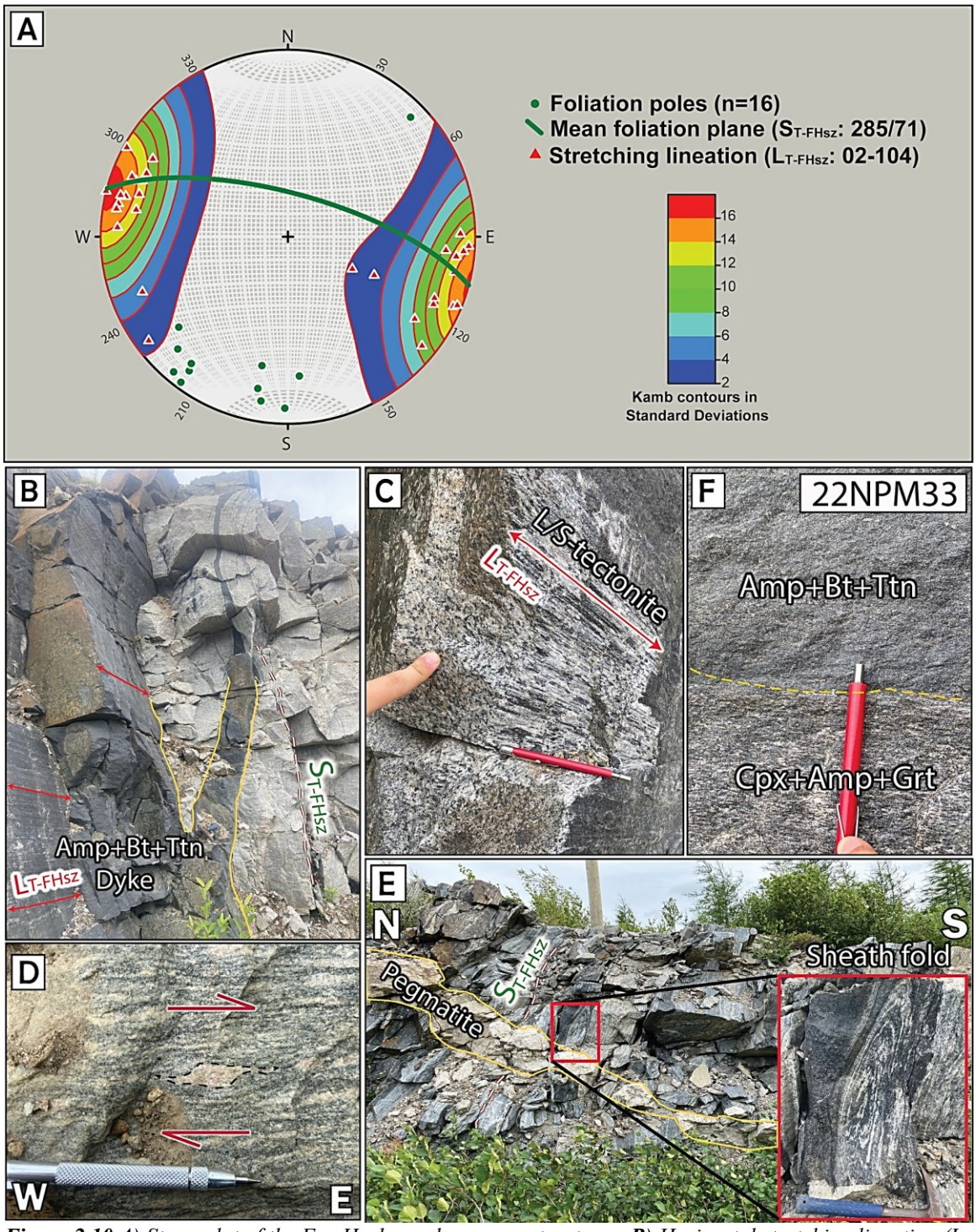

Figure 2.10 A) *Stereoplot of the Fox Harbour shear zone structures.* ***B)*** *Horizontal stretching lineation ($L_{T\text{-}FHsz}$) in dyke plunging less than 10°.* ***C)*** *Elongated and oriented Amp defining ($L_{T\text{-}FHsz}$) in L/S-tectonites exhibited in Amp-tonalites.* ***D)*** *Feldspathic sigmoid in granitic mylonite showing a dextral shear sense in plan view.* ***E)*** *Elongated sheath folds in some leucocratic folded layers that show a dextral shear sense in plan view.* ***F)*** *Contact between Grt-bearing and aphanitic (Amp+Bt+Ttn) mafic dyke (sample 22NPM33).*

2.5.1.1 Sample 22NPM33: Mylonitic diorite dyke

The sample is a mafic dyke composed of Amp+Bt+Pl+Qz+Ttn, classified as a mylonitic diorite. The foliation ($S_{T\text{-}FHsz}$) is primarily defined by the alignment of Amp+Pl, with aligned biotite partially contributing to the foliation as it replaces some amphibole crystals. Additionally, this tabular biotite contains euhedral wedge-shaped titanite grains, suggesting a co-genetic relationship due to their textural equilibrium (Figure 2.11D). Randomly oriented retrograde minerals (Chl+Ep) are observed replacing the prismatic Bt, indicating chlorite formation in a low-strain, hydrated environment. Zircon grains in this sample were analyzed to constrain a crystallization age and maximum age of shearing.

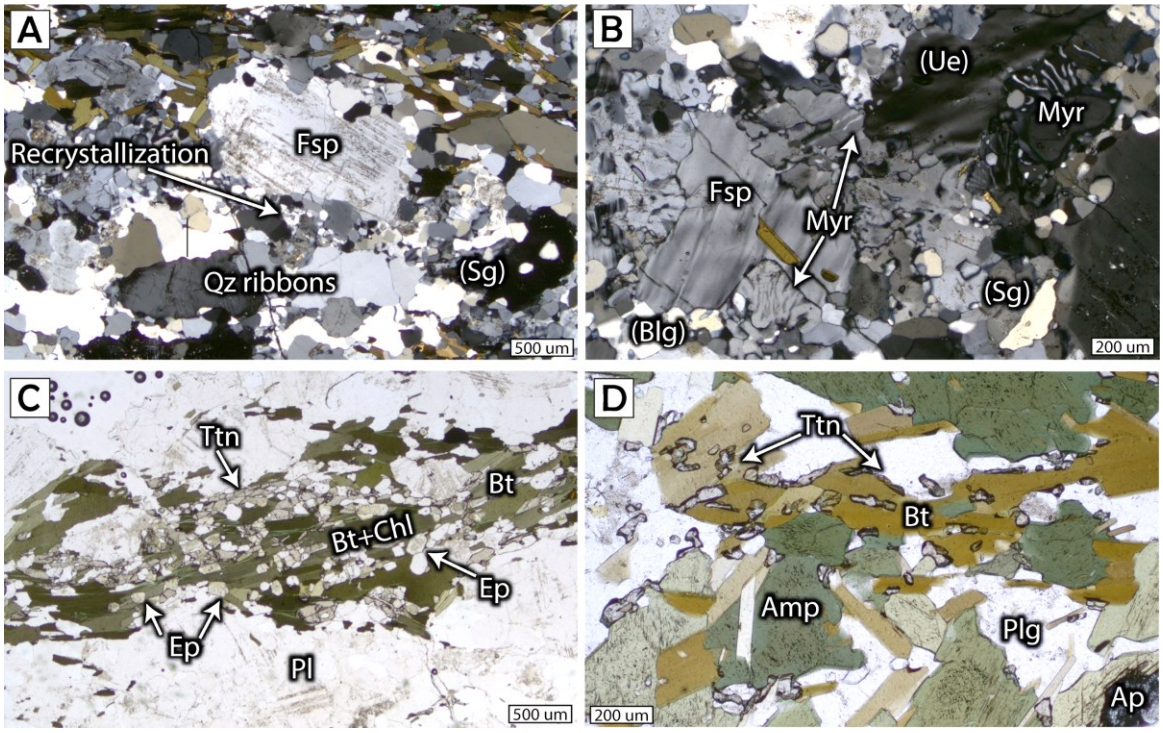

Figure 2.11 *Petrographic features of Fox Harbour shear zone rocks.* ***A)*** *Quartz ribbon with polygonal granoblastic fabric overprinting earlier ameboid shaped crystal boundaries. Kfs porphyroclast surrounded by grain size reduction of Kfs+Qz in granodioritic host rock.* ***B)*** *Myrmekitic texture adjacent to some feldspathic porphyroclasts with undulose extinction (Ue) and subgrain formation (Sg).* ***C)*** *Bt+Chl+Ep+Ttn aligned and defining the $S_{T\text{-}FHsz}$ foliation during greenschist-facies deformation in mediμm-temperature mylonitic granodiorite.* ***D)*** *Biotite partly replacing aligned Amp crystals along their cleavages and edges. Titanite is in textural equilibriμm with Bt, and both define the foliation $S_{T\text{-}FHsz}$ in sample 22NPM33.*

Chapter 3 Analytical Results

3.1Methods and Preparation

3.1.1 U-Pb Zircon

Zircon U-Pb isotopic data were acquired from 12 strategically selected samples (Table 3-1) in the FHVB domain and its shear zone boundaries, including the LHsz, SLsz, and the FHsz. These samples were analyzed to determine protolith and metamorphic ages and timing of deformation using the U-Pb Chemical Abrasion (CA) LA-ICP-MS method for zircon.

ODM and UQAM Analyses:

- Six samples were processed using Electric Pulse Disaggregation (EPD) at Overburden Drilling Management (ODM) in Ottawa, ON. This method induces extensional forces within the planes of weakness of the rock, disaggregating it in water, thereby preparing mineral separates (such as zircon) while avoiding airborne dust and contamination.
- The processed samples (Table 3-1 and Table S1) underwent U-Pb geochronology at the GEOTOP laboratory (UQAM) using a Nu Attom single-collector mass spectrometer attached to a photon machine G2 193 nm excimer laser. The procedure was adapted from Perrot et al. (2017), employing an output energy of 3.18 J/cm², a pulse rate of 6 Hz, and an ablation duration of 30 seconds in 25 μm spots. Data reduction and down-hole fractionation correction were performed using Iolite 4 software, with zircon 91500 (1062 ± 0.8 Ma; Wiedenbeck et al., 1995) as the

primary reference material and Plešovice zircon (337 ± 0.4 Ma; Sláma et al., 2008) as the secondary reference for quality control and validation. The weighted mean age obtained for Plešovice was 344 ± 0.8 (2σ) Ma in a single analytical session.

MUN Analyses:

- Another four samples (Table 3-1 and Table S2) were processed at Memorial University of Newfoundland (MUN) using conventional crushing with a steel jaw crusher and disc mill, followed by sieving with a 400-µm mesh, Wilfley water table density sorting, magnetic separation (Frantz), and heavy liquid separation (methylene iodide, d = 3.32 g/cm³).
- These samples underwent U-Pb zircon analyses at MUN's Core Research Equipment and Instrument Training Network (CREAIT) laboratory using a GEOLAS 193 nm excimer laser ablation system coupled to a Thermo Finningan ELEMENT XR magnetic sector ICP-MS. Analyses utilized an output energy of 4 J/cm², with 200 pulses at a rate of 5 Hz, and an ablation time of 30 seconds in 30 µm spots. The primary standard used to calibrate U-Pb ages was zircon 91500 (1062 ± 0.8 Ma; Wiedenbeck et al., 1995), and the secondary zircon standard was 02123 (295 ± 1 Ma; Ketchum et al., 2001) yielding $^{206}Pb/^{238}U$ ages of 303 ± 2 Ma, 297 ± 2 Ma and 294 ± 2 Ma in three different sessions, with an average of 297 ± 2 Ma. These reference materials were measured every 13 unknown analyses. Data reduction was performed in Igor-Pro Iolite using the VisualAge data reduction scheme of Petrus and Kamber (2012).

Chemical Abrasion (CA) and Imaging:

Zircon fractions from both processing methods underwent thermal annealing at MUN in a muffle furnace at 1000 °C for 36 hours. Subsequently, they were etched in concentrated HF acid within TEFLON pressure vessels at 200 °C for 5-6 hours to reduce radiation damage areas. The zircon grains were mounted in 2.5 cm epoxy pucks (EpoThin epoxy) and polished to expose grain interiors. Imaging was performed using a JEOL JSM 7100F Scanning Electron Microscope (SEM) at MUN, equipped with a Deben Centaurus cathodoluminescent (CL) detector for panchromatic CL imaging, a Thermo energy dispersive spectrometer (EDS) for elemental analysis, and backscatter electron (BSE) imaging. The CL images obtained were used to characterize the morphology, textures, and internal domains of the zircon grains (e.g., Pidgeon, 1992; Rubatto, 2000; Schaltegger & Davies, 2017) followed by selection of typically 25 or 30 μm spots for U-Pb analyses.

SEM-MLA Analysis and Quantitative Mineral Studies:

Quantitative mineral studies were conducted on two thin sections using an FEI Quanta field emission gun 650 scanning electron microscope (SEM) equipped with Mineral Liberation Analysis (MLA) software version 3.14 at MUN. These SEM-MLA maps were performed to identify and locate zircon grains within the thin section to conduct in-situ U-Pb geochronology further. MLA maps (false colour phase maps) were created using GXMAP mode by acquiring energy-dispersive X-ray spectra in a grid every 10 pixels, with a spectral dwell time of 12 ms, and comparing these against a list of mineral reference

spectra. The MLA frames were 1.5 mm by 1.5 mm with a resolution of 500 pixels × 500 pixels. The ablation spot size in these zircon grains was 20 μm.

Age Calculation and Data Interpretation:

Despite the chemical abrasion of zircon grains, discordant ages may arise due to common Pb contamination or isotopic mixing between different age domains. As a result, all the discordant data (> 5%) was excluded from the age estimates in this thesis. Different approaches have been proposed for selecting the best age and cutoff point to switch between the $^{206}Pb/^{238}Pb$ and $^{207}Pb/^{206}Pb$ isotopic systems (e.g., Gehrels et al., 2008; Spencer et al., 2016; Vermeesch, 2021). Generally, the $^{206}Pb/^{238}U$ method is more precise for younger samples, whereas the $^{207}Pb/^{206}Pb$ method is better suited for older samples. This thesis calculated weighted average ages using the $^{206}Pb/^{238}Pb$ age for zircons younger than 1.2 Ga and $^{207}Pb/^{206}Pb$ for those older than 1.2 Ga, as Gehrels et al. (2008) suggested. Because only concordant analyses are considered, the difference in the isotopic ratio used is not significant. For the one detrital sample (quartzite 22NPM21), age maxima were determined using radial plots (finite mixtures set to auto, Vermeesch, 2018), which calculates five age maxima for the dataset. Maximum depositional ages (MDA) were calculated using two methods: 1) the 'maximum likelihood age' (MLA) algorithm (Vermeesch, 2021), which is the most statistically robust method, and 2) a weighted mean of the youngest grain cluster of three or more analyses overlapping at 2σ intervals (YG2σ (3+), Dickinson and Gehrels, 2009), which is a commonly used method for determining robust maximum ages (e.g., Coutts et al., 2019). Isotopic ratio uncertainties are reported at the 2σ level, and concordia diagrams and weighted mean ages were plotted using IsoplotR (Vermeesch, 2018).

3.1.2 U-Pb Monazite

Monazite is a common accessory REE phosphate mineral found across various pressure and temperature settings in sedimentary, metamorphic, and igneous rocks. Monazite is a radioactive mineral that hosts notable concentrations of Th and U (with Th/U>1), forming the basis of its utility as a geochronometer (Engi, 2017). Monazite does not favor the incorporation of Pb in its structure, making single monazite grains suitable for in-situ U-Th/Pb dating (Richter et al., 2019). Also, monazite has the potential to preserve chemical and geochronological information due to its slow diffusion of major and trace components (Williams and Jercinovic, 2002), developing a range of complex textural and compositional zoning as evidence of dissolution and recrystallization (Hetherington et al., 2017).

A monazite U-Pb LA-ICPMS age was acquired from the Crn-Sil schist (22EJT34A). Petrographic and Mineral Liberation analyses were performed to identify monazite grains within this sample. The monazite separation and preparation were performed at MUN using the same procedure described in the zircon methodology. Subsequently, three large hand-picked monazite crystals were polished and mounted in a 2.5 cm epoxy puck. These crystals were then analyzed on the JEOL JXA-8230 Supraprobe EPMA at MUN to acquire qualitative X-ray elemental maps with a 200 msec dwell time, 15 kV accelerating voltage, and a 250 nA beam current. The elements mapped were Th, Y, Pb, U, and Nd, with step sizes between (0.6 µm x 0.6 µm) to (1.3 µm x 1.3 µm) for total run times of 3.5 hours. The maps were collected and edited using JEOL proprietary software. These analyses aimed to identify compositionally distinct domains within the crystals, as variations in growth

sectors or chemical zoning could indicate different REE absorption rates (Engi, 2017). This process facilitated the selection of 25 μm ablation spots to target individual domains.

Monazite U-Pb geochronology was performed at the FiLTER laboratory of the University of British Columbia Okanagan (UBCO) using an Excimer 193 nm laser coupled to an Agilent 8900 ICP-MS, collecting both trace element and U-Pb isotopic ratios from each spot location within an individual grain. The raw data was initially reduced, and downhole fractionation was corrected using Iolite V4 software, using 44069 (424.9 ± 0.4 Ma; Aleinikoff et al., 2006) as a primary reference material for calibration, and three secondary reference materials: Stern (513 ± 1.2 Ma; Goncalves et al., 2016) Steenkamp (1046 ± 7.5 Ma; Knoper et al., 2000; Basson et al., 2016) and Trebilcock (272 ± 4 Ma; Tomascak et al., 1996) for quality control and validation purposes. During the analytical session, the $^{206}Pb/^{238}Pb$ weighted mean age obtained for Stern was 508 ± 2.5 Ma (2σ), for Steenkamp 1049 ± 8 Ma (2σ), and for Trebilcock 274 ± 1 Ma, which are respectively in good agreement with their known age. In the case of trace elements, the reference material NIST610 was used (Jochum et al., 2011), yielding uncertainties associated with measurements around 11% of known values.

3.1.3 U-Pb Titanite

Titanite is a common accessory mineral that can be utilized as a petrochronometer for dating high-temperature tectonic processes, particularly in cases where zircon or monazite fail to crystallize due to unsuitable temperatures, metamorphic conditions or the chemical composition of the rock (Rubatto et al., 2001). This mineral incorporates trace

elements into its crystal structure, which can be linked to different P-T conditions and metamorphic assemblages (Kohn, 2017; Olierook et al., 2019). Titanite could remain unaffected by diffusion of Pb at temperatures as high as 750 °C (Spencer et al., 2013) and can undergo crystal-plastic deformation (e.g., Gordon et al., 2021; Silerova et al., 2023) and recrystallization via dissolution-reprecipitation at greenschist- to granulite-facies conditions, resulting in the preservation of numerous generations of compositional zoning and microstructures, providing rich record of superimposed metamorphism in complex orogenic belts (Olierook et al., 2019; Scibiorski et al., 2019; Moser et al., 2022 and references therein).

In-situ titanite U-Pb dates, trace elements, zoning, and microstructures were combined to understand deformation and metamorphism from four samples collected from the FHVB domain (2), LHsz (1), and SLsz (1). Titanite was identified after petrographic and Mineral Liberation analysis conducted on four (4) distinct polished thin sections, revealing various petrochronological relationships within the FHVB and its main shear zone boundaries.

Targeted titanite grains were imaged on the JEOL JSM 7100F Scanning Electron Microscope (SEM) using high-contrast BSE imaging to identify any zoning within every grain. These grains were also analyzed on an EPMA JEOL JXA-8230 superprobe with a W filament and 5 WDS spectrometers at MUN to generate X-ray element maps of Al, Fe, Zr, Ti, and Ce, with a 200 ms dwell time, 20 kV accelerating voltage, and a 200 nA beam current (Moser et al., 2022), titanites were run for 3-4 hours for each map with step sizes between (0.4 μm x 0.4 μm) and (1.4 μm x 1.4 μm) to identify any compositional zoning. The maps were collected and edited using JEOL proprietary software. Then, strategic

ablation spots with a diameter of 30 μm were selected, considering the different elemental domains.

In-situ titanite U-Pb and trace-element compositions were obtained at the CREAIT laboratory of MUN using the GeoLas 193nm excimer laser ablation system coupled to a Thermo Finningan ELEMENT XR magnetic sector-ICPMS. The analyses utilized an output energy of 4 J/cm^2, 200 pulses with a rate of 5 Hz, with an ablation analysis time of 40 seconds. Titanite standards used to calibrate U-Pb ages were Bear Lake (1039 ± 23 Ma, Fisher et al., 2020) as a primary reference material. In-house Bancroft - Ontario (comparable to Ontario titanite, 1053 ± 3 Ma, Sun et al., 2012; Spencer et al., 2013; Ma et al., 2019) was used as a secondary external standard for quality control and yielded an age of 1060 ± 8 Ma. These reference materials were measured twice every 13 unknown analyses, including the trace elements reference materials NIST610 and NIST612.

Trace elements geochemistry in titanite is particularly effective for differentiating whether a grain is igneous, recrystallized, or metamorphic, using Th/U, Al/Fe, Th/Pb, Al/(Al+Fe), REE patterns, and Eu anomalies (Kowallis et al., 1997; Aleinikoff et al., 2002; Olierook et al., 2019; Scibiorski et al., 2019; Kirkland et al., 2020, Scibiorski and Cawood, 2022; Sullivan et al., 2024). Trace elements (Al, Si, Ti, V, Cr, Mn, Fe, Hf, Y, Zr, Nb, Ta, La, Lu) and U-Pb isotopic data were collected during each spot analysis. To differentiate between igneous, recrystallized, and metamorphic titanite, some indices such as Al/(Al+Fe), Th/U and Th/Pb ratios, REE gradients, and Eu anomalies (Aleinikoff et al., 2002; Olierook et al., 2019; Kirkland et al., 2020; Scibiorski and Cawood, 2022) were used for every sample.

Titanite often contains significant amounts of common lead (Pb_c Cherniak, 1993), complicating measurements due to the mixture of radiogenic Pb and Pb_c. Therefore, correcting for Pb_c is generally essential for obtaining meaningful U-Pb ages in titanite. The most widely used method for this correction is the ^{207}Pb-correction (Spencer et al., 2013; Kirkland et al., 2016), which assumes that each measured data point lies on a mixing line between radiogenic Pb and Pb_c based on a known composition of common Pb derived on a global lead evolution model (e.g., Stacey-Kramers, 1975) or from matrix minerals. However, due to variable Pb_c in samples herein, this thesis employs the method of free regressing of the uncorrected U-Pb data on a Terra-Waserburg diagram, where the upper intercept represents the Pb_c composition, and the lower intercept represents an age.

3.2 U-Pb Geochronological Results

Interpretations related to magmatic crystallization, maximum depositional age (MDA), deformation, and metamorphism are summarized in Table 3-1. Concordia and weighted average plots in Figure 3.9 display the EPMA morphology, texture, and trace element data for monazite from the corundum mica schist (22EJT34). Additionally, petrochronological analyses of titanite are provided, including Mineral Liberation analyses, EPMA imaging of selected titanite grains, and in-situ U-Pb and trace element data via LA-ICPMS.

3.2.1 The Fox Harbour Volcanic Belt domain

3.2.1.1 U-Pb Zircon

3.2.1.1.1 Sample 22NPM22: Granitic augen-gneiss.

Zircon crystals in this granitic augen-gneiss range from 30 to 300 μm in length and 50 to 120 μm width, exhibiting idiomorphic shapes. The morphologies vary from prismatic (elongation ratio 2:1 to 5:1) to stubby sub-rounded crystals, which are colorless to light pink. CL imaging revealed spaced oscillatory zoning (OZ) and patchy patterns (e.g., Figure 3.1A, spots #5, # 51, #57, #59), along with resorbed textures (#71) in the central parts of the grains, mantled by a finer oscillatory texture (e.g., Figure 3.1A, #28, #52, #60) and bright patchy zoning (#6) on the outer margins. Furthermore, thin (15 μm wide) and bright homogeneous rims surround these whole grains but were too small to analyze (e.g., near spots #28, #52, and #60 in Figure 3.1A). Oscillatory and patchy patterns in the external margins of the zircon commonly exhibited faded zoning (e.g., #52, #60) as well as well-defined zoning (#28, #6). Bright-CL zones and rims exhibited homogeneous zones truncating patchy/sector zoning to gradational boundaries within the zoned zircon.

Eighty-seven analyses were performed on 73 individual grains, targeting the oscillatory/patchy zoning of the central and outer margins of the grains, with 61 out of 87 analyses being concordant. The concordant analyses yielded $^{207}Pb/^{206}Pb$ dates ranging from 1607 to 1452 Ma (Figure 3.1B), with Th/U ratios varying from 0.51 to 2.14, which are typical of magmatic zircons (Corfu et al., 2003). The data spread along a linear concordant array, suggesting Pb-loss, isotopic mixing, or protracted crystallization.

A free regression (discordia model 1 of Vermeesch, 2018) yielded an upper intercept age of 1516 ± 11 Ma and a lower intercept age of 875 ± 215 Ma (MSWD = 1.3; $p(x^2) = 0.05$). The lower intercept date points towards a Grenvillian age (~1.0 Ga), which is a known metamorphic age in the study area. Due to the spread in data, the oldest concordant dates likely reflect the crystallization age with minimal Pb-loss effects; therefore, 1.6 Ga is the best estimate for the crystallization of this sample.

3.2.1.1.2 Sample 22NPM03: Granodioritic Gneiss

The zircon crystals are brownish to uncolored and vary in size, ranging from 20 to 250 μm; their idiomorphic shapes range from prismatic subhedral with an elongation ratio of 2:1 to 5:1 to stubby subrounded forms. These zircon crystals display broad oscillatory and patchy zoning (e.g., Figure 3.1C, spots #13, #29, #31) in CL typical of magmatic zircons. Additionally, a thinner bright rim (10 μm) is observable in some grains (close to spot #20, #31, #37). However, ablating this rim was not possible because of its size (Figure 3.1C).

Thirty-nine analyses were performed on 34 grains, with nineteen analyses excluded due to discordance and >5 % uncertainty values. The remaining 20 concordant analyses span $^{207}Pb/^{206}Pb$ dates between 1560 and 1468 Ma, exhibiting oscillatory and patchy zoning with Th/U ratios varying from 0.35 to 1.11, typical of igneous zircons (Corfu et al., 2003). These igneous zircon grains yielded a weighted mean $^{207}Pb/^{206}Pb$ age at 1516 ± 12 Ma (MSWD = 0.98), which is considered to represent the crystallization age of the granodiorite Figure 3.1D).

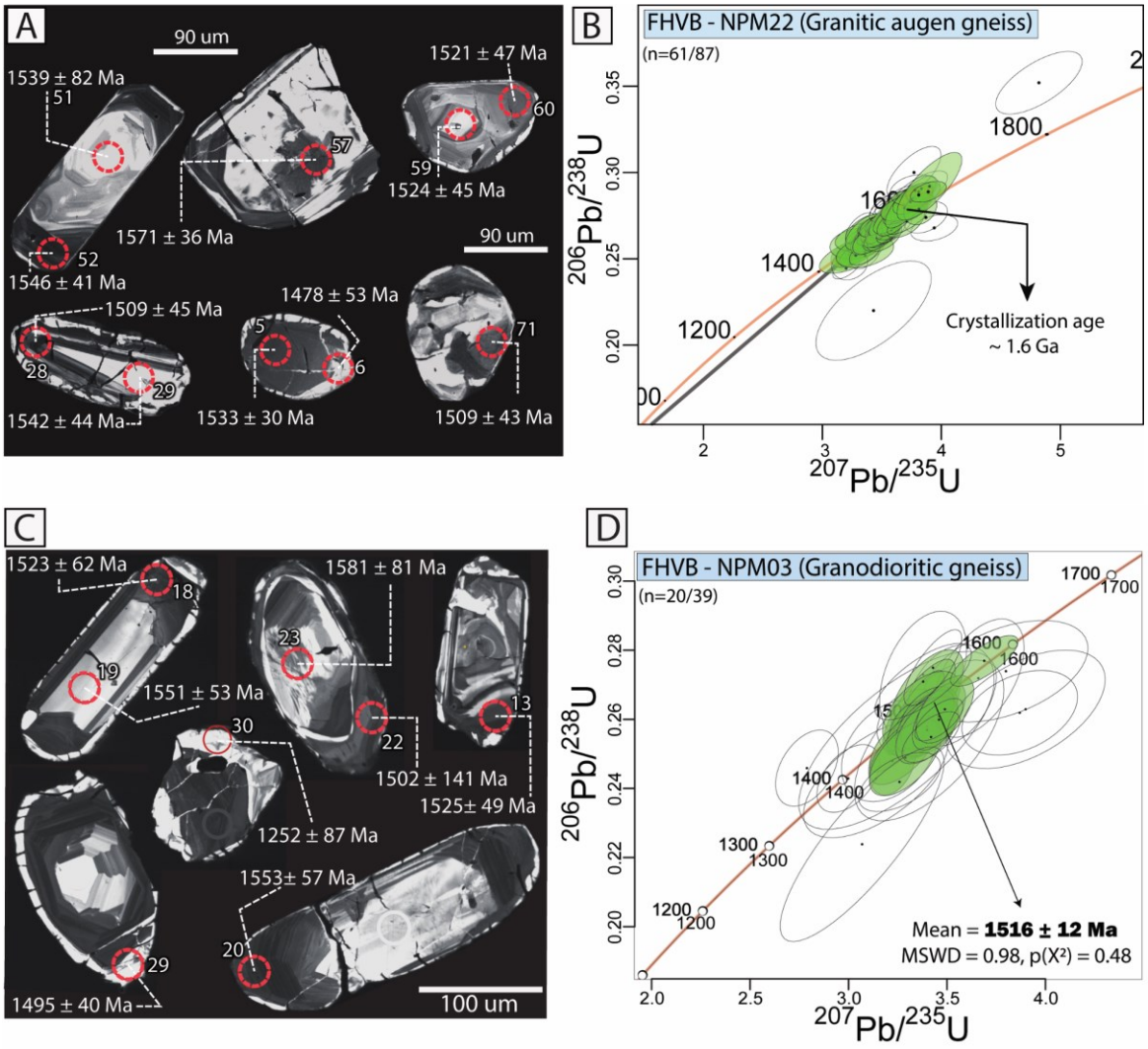

Figure 3.1. *Composite Wetherill plot of zircon geochronological data from the orthogneisses within the FHVB domain. A-B) Sample 22NPM22 (Granitic augen-gneiss), C-D) Sample 22NPM03 (Granodioritic gneiss). A and C) Representative CL zircon images where the red dashed circles denote the ablation pits (30 µm). B) U-Pb zircon data for sample 22NPM22. Green ellipses represent analyses used in age calculation, while white ellipses represent discordant and excluded data. D) U-Pb zircon data for sample 22NPM03 (white ellipses: discordant data and concordant data with high uncertainties). Green ellipses represent data used for the weighted mean $^{206}Pb/^{207}Pb$ age calculation of 1516 Ma.*

3.2.1.1.3 Sample 22NPM26: Grt-bearing leucodiorite

Zircon crystals exhibit subhedral to euhedral morphologies, ranging from dark brown to colorless in stubby shapes, and elongated crystals (elongation ratio 3:1 to 5:1).

The grain sizes vary from 25 to 200 μm. Under CL, the cores of the zircon grains display distinctive patchy zoning and a bright, fine to broad oscillatory growing texture. By contrast, the outer margins of the grains reveal a fine oscillatory texture. Additionally, a rim is exhibited with a patchy zoning pattern (Figure 3.2A).

Forty-six analyses were conducted in 42 zircon grains, with 38 analyses yielding concordant ages ranging from 1526 to 1111 Ma with Th/U ratios varying from 1.41 to 0.01. Within this concordant dataset, eight spread out analyses do not display age clustering: seven older analyses range from 1526 to 1371 Ma and represent the central part of grains with patchy and oscillatory zoning displaying Th/U values from 1.18 to 0.46, interpreted as inherited igneous zircons. One younger analysis (1111 Ma) corresponds to a rim with bright, patchy homogeneous zoning and a low Th/U ratio (0.01), indicating possible metamorphic overgrowth around 1.0 Ga.

Table 3-1. *Location and description of samples analyzed by U-Pb CA-LA-ICPMS and in-situ LA-ICPMS. Reference system UTM NAD83, 21N*

Domain	Sample Name	Coordinates		Lithology	Mineral	Interpreted age	Age[a]	2σ[b]	MSWD	n	Type
		Easting	Northing								
FHVB	22NPM22[1]	580047	5805808	Granitic augen-gneiss	Zircon	Crystallization	**~ 1.60 Ga**	-	-	34/61	$^{207}Pb/^{206}Pb$ Weighted Mean
	22NPM03[1]	582113	5806090	Granodioritic Gneiss	Zircon	Crystallization	**1516**	12	0.98	20(39)	$^{207}Pb/^{206}Pb$ Weighted Mean
	22NPM26[2]	587965	5803661	Grt-bearing leucodiorite	Zircon	Crystallization	**1324**	8	1.7	30(46)	$^{207}Pb/^{206}Pb$ Weighted Mean
	22NPM01[2]	589925	5802970	Grt-bearing leucodiorite	Zircon	Crystallization	**~ 1.30 Ga**	-	-	30(55)	$^{207}Pb/^{206}Pb$ Weighted Mean
	22NPM21[1]	579895	5805949	Quartzite	Zircon	Max. Dep.	**~ 1.30 Ga**	-	-	215(220)	MLA - Concordant age
					Zircon	Metamorphism	**~1.06 Ga**	-	-	3(5)	$^{206}Pb/^{238}U$ Weighted Mean
	22NPM48A2[1](*)	587965	5803661	Mesocratic Cpx-rich band	Titanite	Metamorphism	**1058**	85	1.6	17(18)	Discordia lower intercept
	22NPM48A3[1](*)	587965	5803661	Grt-Hbl-Cpx+Pl+Qz Leucosome	Zircon	Metamorphism	**1041**	39	1.6	4(5)	$^{206}Pb/^{238}U$ Weighted Mean
					Titanite	Deformation	**987**	74	2.5	23(28)	Discordia lower intercept
	22EJT34[3]	558233	5813351	Crn-Sil schist	Monazite	Metamorphism	**1044**	5	0.69	9(11)	$^{206}Pb/^{238}U$ Weighted Mean
LHsz	22NPM39B[2]	561907	5807834	Granodiorite Gneiss	Zircon	Crystallization	**1696**	13	1.8	5(20)	$^{207}Pb/^{206}Pb$ Weighted Mean
					Zircon	Metamorphism	**~ 1.0 Ga**	-	-	-	Weighted Mean 206/238 age
					Titanite	Metamorphism	**996**	17	5.2	14(17)	Discordia lower intercept
	22NPM39A[2]	561907	5807834	Syn-deformational quartz-monzonitic dyke	Zircon	Crystallization	**~ 1.0 Ga**	-	-	-	Discordia lower intercept
	22NPM40[2]	561654	5807913	Post-deformational monzogranitic dyke	Zircon	Crystallization	**0.95 Ga**	-	-	-	Discordia lower intercept
SLsz	22NPM11[2]	589926	5802969	Mylonitic granodiorite	Zircon	Crystallization	**1700**	2.7	2.3	132(133)	Discordia upper intercept
					Titanite	Metamorphism	**~ 1.0 Ga**	-	-	-	Discordia upper intercept
FHsz	22NPM33[1]	554794	5810345	Mylonitic diorite dyke	Zircon	Crystallization	**1079**	9	1.6	26(47)	$^{206}Pb/^{238}U$ Weighted Mean

(*) Thin section in-situ U-Pb zircon analysis (20 um spot size), in-situ U-Pb titanite analysis (30 um spot size)
[1]Samples analyzed at CREAIT laboratory - Memorial University of Newfoundland
[2]Samples analyzed at GEOTOP laboratory - University of Quebec in Montreal
[3]Samples analyzed at FiLTER laboratory - University of British Columbia Okanagan
[a]Mean weighted values or Discordia age per sample in Ma unless stated.
[b]Reported uncertainties are propagated at 2σ level

However, these eight analyses are not considered further for the crystallization age. The remaining 30 concordant analyses show a strong age cluster around 1.32 Ga, representing oscillatory zoned zircon with Th/U ratio ranging from 1.41 to 0.21 (typical of magmatic zircons). This cluster yielded a weighted mean $^{207}Pb/^{206}Pb$ age of 1324 ± 8 Ma (MSWD = 1.7), interpreted as the crystallization age of the Grt-bearing leucodiorite (Figure 3.2A).

3.2.1.1.4 Sample 22NPM01: Grt-bearing leucodiorite

The zircons in this sample vary in size from 25 to 150 μm and exhibit stubby to prismatic elongated shapes (length/width 5:1 and 3:1). Their colours range from clear to dark brown. Under CL imaging, most grains display zonation sectors, convolute zoning in the cores, and oscillatory texture in both the cores and outer margins of the whole grain typical of igneous growth textures (e.g., Hoskin and Schaltegger, 2003). A bright patchy homogeneous rim is also exhibited in some of the grains (e.g., #17 and #22, Figure 3.2B: in the case of spot # 22, it overlaps an oscillatory and patchy domain, yielding a young age of around 1.2 Ga, possibly a mixed age between 1.3 and 1.0 Ga.

A total of fifty-five analyses were performed in fifty-five grains, with twenty-one analyses being excluded because of discordance. The remaining 35 concordant analyses span a broad age spectrum from 1715 to 1007 Ma with Th/U ratios varying from 1.86 to 0.03, displaying a dominant cluster from ca. 1.3 to 1.2 Ga (Figure 3.2B).

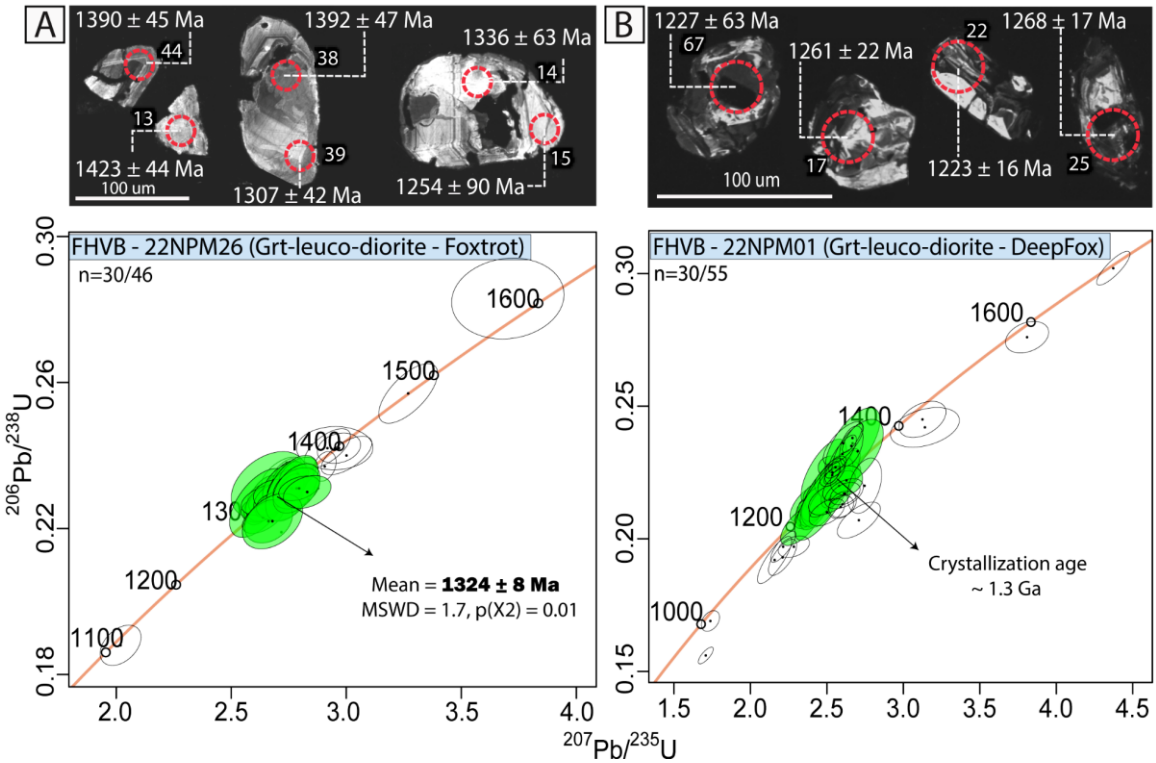

Figure 3.2. *CL images and composite plot of zircon U-Pb CA-LA-ICPMS geochronological data from the folded Grt-bearing leucodiorite layers in the mafic rocks of the FHVB. Red dashed circles represent 25 µm ablation spots, while white ellipses on concordia plots represent excluded data. A) Sample (22NPM26) where green ellipses define the crystallization age at 1324 ± 8 Ma. B) Sample (22NPM01) where green ellipses represent a concordant spread where older 1.3 Ga analyses are interpreted as the age of igneous crystallization.*

Among these 35 analyses, four analyses with cores show bright sector zoning and an average Th/U of 0.83 yielded $^{206}Pb/^{207}Pb$ ages varying from 1715 to 1478 Ma; these analyses were excluded and interpreted as inherited grains since they are individual sporadic dates older than the main cluster. Additionally, one significantly younger analysis, yielding a date of 1007 Ma in a blurry core with convolute zoning and a Th/U ratio of 0.39, was excluded (Figure 3.2B, grey ellipses). The remaining 30 analyses represent grains with patchy zoning, oscillatory overgrowths, and convolute textures, forming a cluster around 1.3 Ga with an average Th/U ratio of 0.74 (characteristic of magmatic zircons). These 30 analyses spread between 1332 and 1195 Ma where the younger analyses are likely

isotopically disturbed (mixing or Pb loss) while the older analyses approximate the crystallization age of the sample ~ 1.3 Ga.

3.2.1.1.5 Sample 22NPM21: Quartzite

Zircon grains are euhedral to subhedral, varying from colourless to dark brown, with stubby subrounded shapes and an aspect ratio of 3:1. Grain sizes vary from 50 to 250 μm. Internal textures exhibit clear core-rim relationships including a bright to dark patchy zoning and fine-to-broad oscillatory zoning patterns in rounded core domains. These are surrounded by 15-50 μm rims displaying bright, homogeneous patchy zoning and OZ. The transition from cores to the rims is marked by a very dark CL zone (Figure 3.3, # 79-80).

A total of 295 analyses were conducted in 278 zircon grains, targeting both core and rim domains. Of these, two hundred fifteen (n=215) analyses were concordant, with dates ranging from 3511 to 1056 Ma. Within this age range, the youngest five analyses correspond to 30-60 μm rims with bright homogenous patchy zoning, spanning dates from 1135 to 1056 Ma and a Th/U ratio < 0.1, characteristic of metamorphic zircon (Rubatto, 2017). This cluster of Grenvillian ages was removed from the detrital age calculation due to its age, chemistry, and zonation, which likely represents in situ growth after deposition (Figure 3.3). All interpreted in-situ rim analyses fall on a mixing line where the youngest 1.06 Ga analysis is likely closer to the age of the metamorphic rim growth.

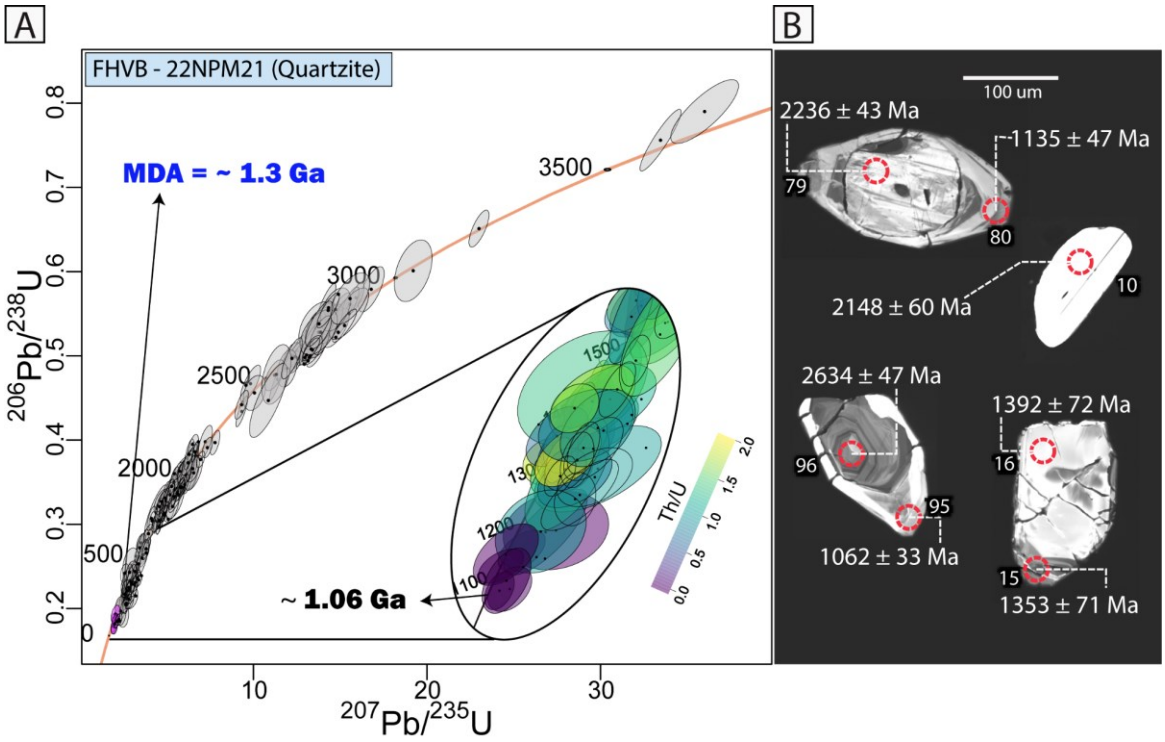

Figure 3.3. *Composite plot displaying zircon U-Pb CA-LA-ICPMS geochronological data from quartzite sample (22NPM21) in the Foxtrot area. A) Detrital zircon crystals are plotted in grey ellipses, and the ~ 1.0 Ga metamorphic population is in purple ellipses. Zoom-in shows the difference in Th/U ratio between the ~1.0 Ga and the ~1.3 Ga zircon population. B) CL images show bright patchy zoned cores with younger bright patchy rims. Red dashed circles represent 30-micron ablation spots.*

The remaining concordant analyses (n=215) represent the detrital zircon grains and include older patchy zoned cores (183) and fine to broad oscillatory zoned rims (32). The $^{207}Pb/^{206}Pb$ dates range from 3511 to 1245 Ma, with Th/U ratios ranging from 3.75 to 0.01. Age maxima from detrital zircon in this sample occur at ~ 3469 Ma (prop 1.4 %), ~ 2713 Ma (prop 24%), ~ 1989 Ma (prop 23%), ~ 1795 Ma (prop 27%), and ~ 1418 Ma (prop 24%) (Vermeesch, 2018). MDA estimates for the 215 detrital zircon grains include a weighted mean $^{207}Pb/^{206}Pb$ age of 1327 ± 16 Ma (MSWD = 0.81, n = 24; YC2σ (3+)) and 1302 ± 23 Ma (MLA), which overlap within uncertainty. Thus, the maximum deposition age for the sample is ~1.30 Ga.

3.2.1.1.6 Sample 22NPM48A3: Grt-Hbl-Cpx+Pl+Qz Leucosome

Zircon crystals herein have an average size of 50 µm, an anhedral to subhedral shape, and display a bright, homogeneous patchy texture in CL (Figure 3.5, white stars). Some zircon grains occur as inclusions in the aligned-titanite grains that define the $S_{3\text{-FHVB}}$ foliation. Others were observed as small, rounded grains adjacent to the Amp+Cpx+Grt+Qz+Pl leucosome.

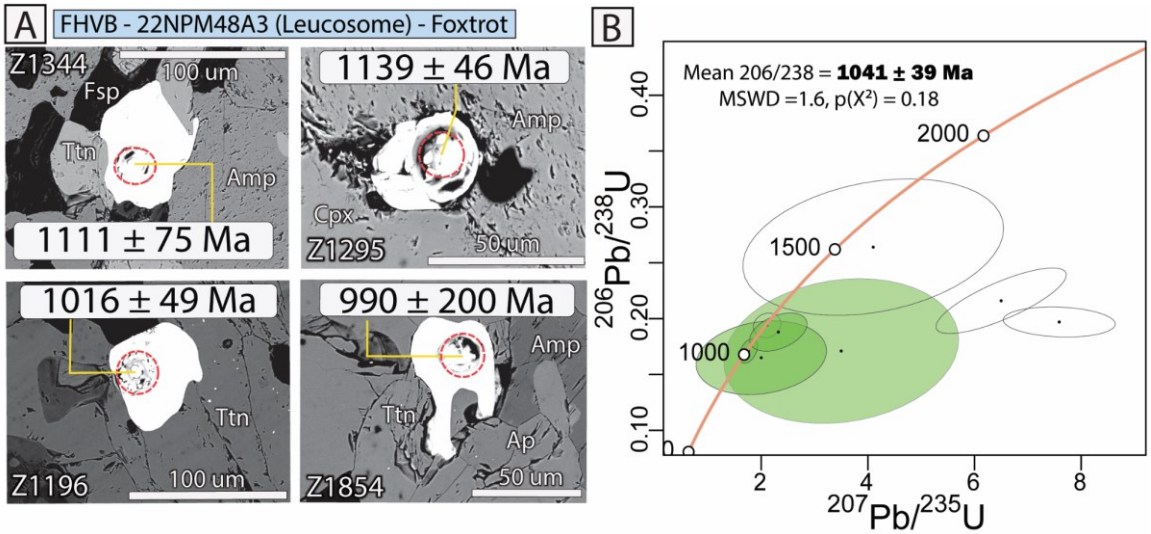

Figure 3.4*. In-situ zircon U-Pb LA-ICPMS geochronological data from leucosome sample (22NPM48A3). A) BSE images exhibiting some of the zircon grains analyzed with a red circle representing the 20-µm ablation spot size performed. B) Concordia diagram showing an imprecise age cluster around 1.0 Ga representing the leucosome crystallization age.*

Eight analyses were performed (20 µm spot ablation size) on eight zircon grains within the leucosome (Figure 3.4A). Of these, three analyses were excluded due to discordance and high uncertainties (including two concordant analyses); upon later inspection these spots intersected minerals other than zircon, such as titanite or garnet. The remaining five concordant analyses represent homogeneous patchy grains spanning $^{206}Pb/^{238}U$ dates from 1143 to 985 Ma. Four of these five grains exhibit a Th/U ratio lower than 0.1, while the

fifth grain, associated with Cpx+Amp exhibits a Th/U ratio of 1.24 and yielded a date of 1143 Ma. The four concordant grains with a Th/U ratio below 0.1 yielded a $^{206}Pb/^{238}U$ weighted mean age of 1041 ± 39 Ma (MSWD = 1.6), interpreted as the crystallization age of the leucosome Figure 3.4B).

3.2.1.2 U-Pb Titanite

3.2.1.2.1 Sample 22NPM48A3: Grt-bearing leucosome and melanocratic Amp-rich band

Most titanite grains in this thin section appear homogeneous in BSE or exhibit irregular, patchy zoning with no clearly defined domains. However, qualitative EPMA X-ray maps of Al and Fe (Figure 3.5A) reveal concentric growth zoning in all the analyzed titanites, characterized by low-Al and low-Fe cores transitioning to high-Al and high-Fe rims, defining compositional domains with sharp to gradational boundaries.

Twenty-eight U-Pb and trace element analyses were conducted in six titanite crystals aligned with $S_{1/2\text{-}FHVB}$ in the Amp-rich band (Ttn_1) and the late titanite seams $S_{3\text{-}FHVB}$ (Ttn_2). Five out of twenty-eight analyses were excluded due to zircon/apatite inclusions (spots #3 and #17), indicated by elevated P (5900 ppm) and Zr (4770 ppm) content, or due to mineral mixing during ablation with Hbl or Qz (spots #28 and 29). Therefore, the remaining 23 analyses were divided into two petrographic and morphological titanite populations, Ttn_1 (n=10) and Ttn_2 (n=13). Ttn_1 crystals within the Amp-rich band range in size from 40 to 300 μm in sphenoidal and irregular subrounded grains, some of which show fracturing (e.g., Figure 3.5A, T1, T5, and T13), while the Ttn_2 crystals within the cross-cutting seams

are smaller (~ 40 µm) and contain zircon and apatite inclusions (e.g., Figure 3.5B, T14, T16, and T22).

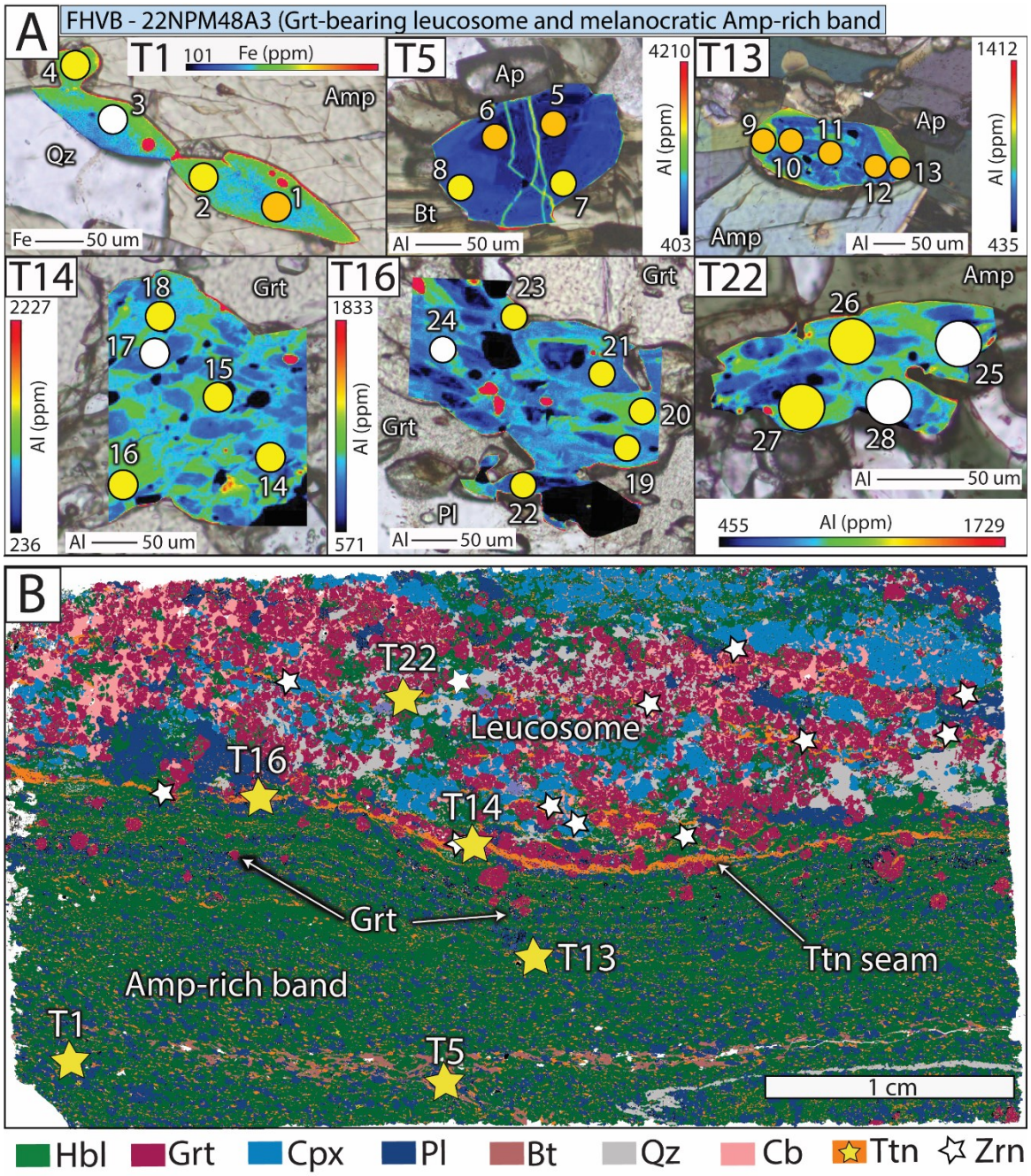

Figure 3.5. *A) EPMA X-ray elemental mapping in titanite grains displaying aluminum (Al) and iron (Fe) zoning. Some titanite grains exhibit Fe and Al-rich mineral inclusions (red colour). Scale bars are qualitatively relative to Al and Fe in the grains. Orange (Ttn1) and yellow (Ttn2) circles represent the 30-µm size spots ablation; white circles are the excluded analyses. B) SEM-MLA phase map of the thin section showing the location of the titanite grains in yellow stars and zircon grains in white stars.*

Ttn_1 within the Amp-rich band exhibit sector zoning in Al-Fe maps (Figure 3.5, T1, T5, and T13). Their central portions have average U concentration of 27 ppm, Th/U ratios of 0.08, Th/Pb ratios of 0.04, and Al/Fe ratio of 3.37, with Al and Fe contents of 9533 ppm and 2885 ppm, respectively. These values, along with an Al/Al+Fe ratio of 0.77, are consistent with metamorphic titanites (e.g., Aleinikoff et al., 2002; Olierook et al., 2019). The REE pattern shows a parabolic trend characterized by a steep positive LREE/MREE slope ($[La/Sm]_N$ of 0.21), a positive Eu anomaly ($[Eu/Eu^*]_N$ = 1.17), and a moderate to negative HREE slope (Inset Figure 3.6), typical of metamorphic titanites (e.g., Olierook et al., 2019; Scibiorski et al., 2019; Kirkland et al., 2020). Although the outer margins in T1 and T5 display higher Al (15622 ppm) and Fe (13255 ppm) concentrations than their central parts, their REE parabolic patterns remain similar, including a positive Eu anomaly ($[Eu/Eu^*]_N$ = 1.26). The positive Eu anomaly suggests Ttn_1 growth at the expense of reactants Pl or Cpx. This suggests a single titanite population (Ttn_1) with a metamorphic signature that grew aligned parallel to $S_{1/2\text{-FHVB}}$ and $S_{3\text{-FHVB}}$. This population yielded a free regression age of 1050 ± 203 Ma (MSWD = 0.89, $p(x^2)$ = 0.52; n=10, Figure 3.6).

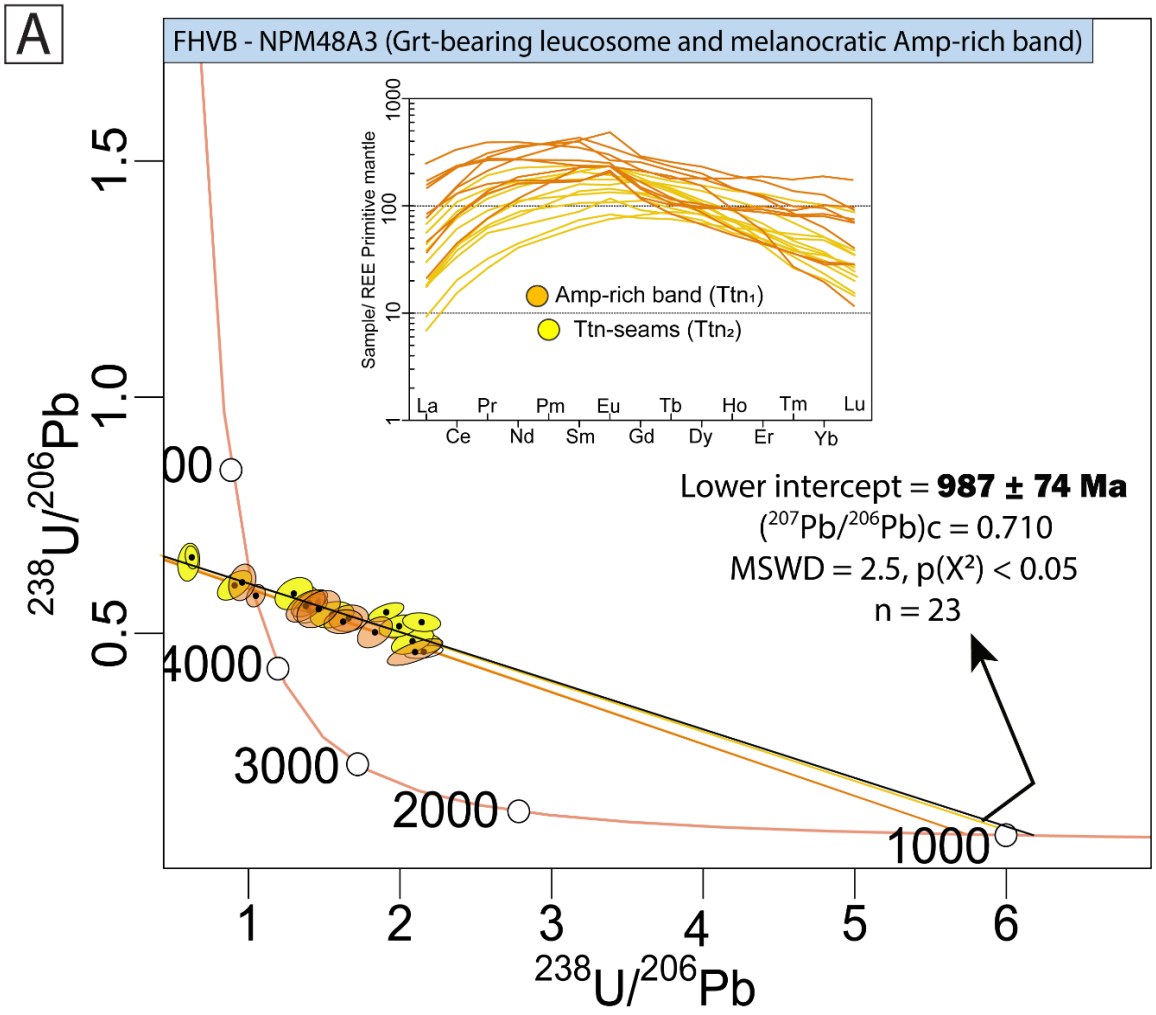

Figure 3.6. A) *Sample 22NPM48A3 titanite plotted on a Tera-Wasserburg concordia plot colour-coded for the petrographic group (Ttn_1 and Ttn_2). Inset shows the REE plot of similar patterns for the two petrographic groups (yellow and orange).*

The remaining thirteen analyses of Ttn_2 within the cross-cutting seams (T14, T16, and T22) have a mean U content of 17 ppm, a Th/U ratio of 0.09, a Th/Pb of 0.06, and an Al/Fe ratio of 3.90, with Al content of 14118 ppm and Fe content of 3819 ppm. The Al/Al+Fe ratio is 0.79, consistent with trace element characteristics of a metamorphic or recrystallized titanite (Aleinikoff et al., 2002; Olierook et al., 2019). Additionally, although the REE patterns display a steep positive slope in LREE/MREE ($[La/Sm]_N$ of 0.19), this pattern is depleted compared to the LREE/MREE pattern in Ttn_1, which may reflect the

compositional location of the two populations. A positive Eu anomaly with an average $[Eu/Eu^*]_N$ = 1.07 and a negative slope and depletion in HREE (Figure 3.6) is typical of titanite growth at the expense of Pl and after available HREE were preferentially partitioned into garnet (Olierook et al., 2019; Scibiorski., 2019; Kirkland et al., 2020). The Ttn_2, which directly relate to $S_{3\text{-FHVB}}$, yielded a free regression age of 993 ± 79 Ma (MSWD = 3.4, $p(x^2)$ < 0.05, n=13, Figure 3.6).

Both Ttn_1 and Ttn_2 are defined by their distinct mineralogical domains, but both follow parallel the $S_{1/2\text{-FHVB}}$ foliation and exhibit similar trace element and REE patterns and overlapping dates and are likely coeval with the minor chemical differences being due to local compositional domains. Therefore, all of the 23 analyses were combined into a free regression that yielded a lower intercept age of 987 ± 74 Ma (MSWD = 2.5, $p(x^2) < 0.05$; n=23), interpreted as the age of titanite growth after Pl related to $S_{2\text{-FHVB}}$ or a younger $S_{3\text{-FHVB}}$.

3.2.1.2.2 Sample 22NPM48A2: Mesocratic Cpx-rich band

Titanite grains are aligned parallel to $S_{1\text{-FHVB}}$, range from 40 to 400 μm, and exhibit a subhedral to euhedral wedge to elongated rhomb shape. The titanites display homogeneity and brightness in BSE images with limited evidence for zoning. However, the EPMA X-ray mapping reveals sector and concentric zoning within the Al, Fe, and Ti maps. Titanites were separated and analyzed into two petrographic domains: Ttn_1, represents titanites located in the clinopyroxene-rich bands (T3, T4, and T20), which display concentric zonation of low to high aluminum content; Ttn_2 exhibits sector zoning in the titanite grains

within the Qz+Pl-rich bands (T11 and T14), (Figure 3.7A) these grains are fractured and exhibit inclusions of clinopyroxene and zircon.

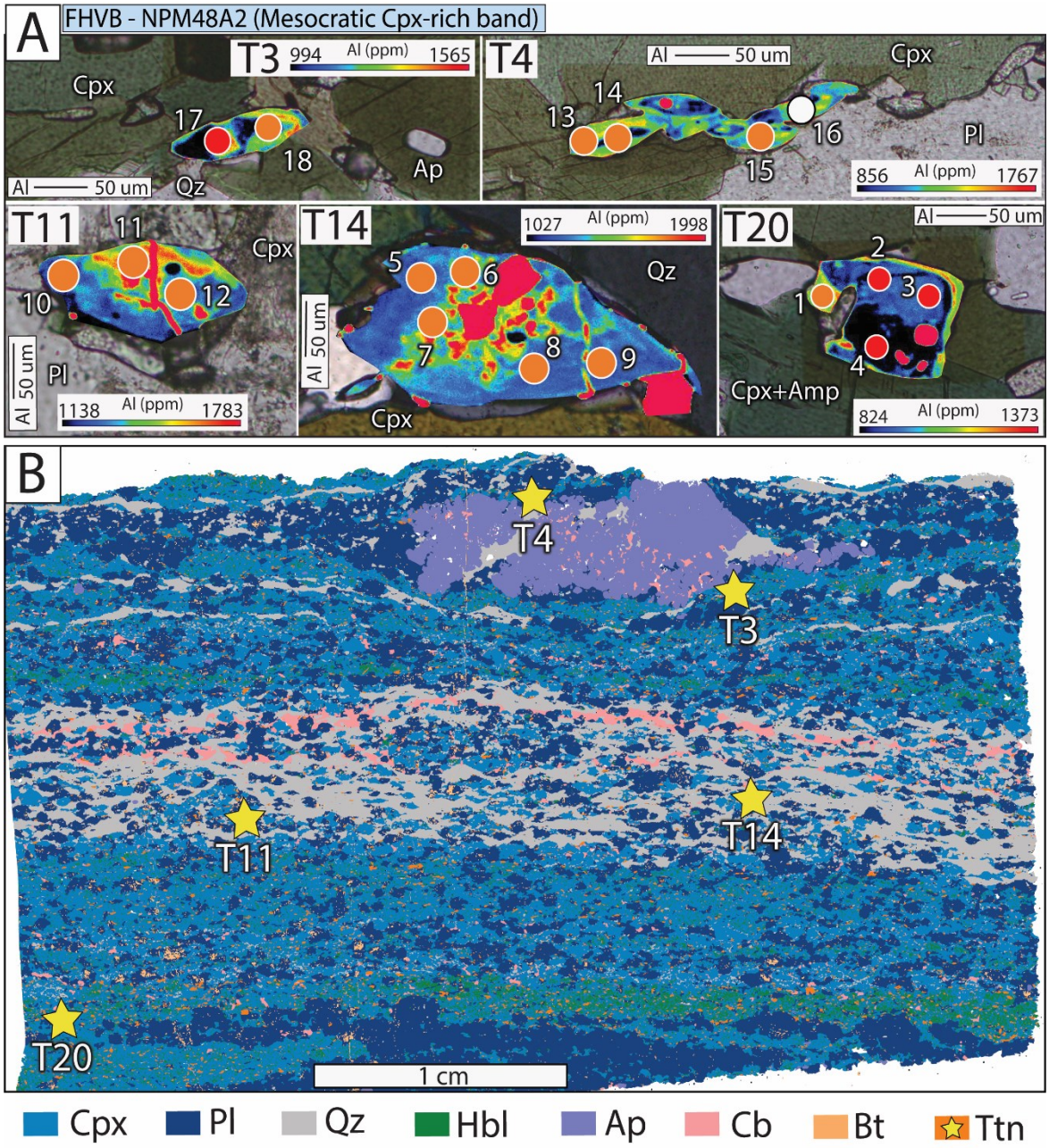

Figure 3.7. *A) EPMA phase mapping shows aluminum (Al) concentric zonation (T3, T4, and T20) and sector zoning (T11 and T14) within Ttn grains. B) SEM-MLA phase map showing titanite grains analyzed in thin section 22NPM48A2 (yellow stars).*

For this sample, eighteen spots were targeted in the five selected grains of the Cpx-rich and the Qz+Pl-rich bands (Figure 3.7B). One analysis with high uncertainty (Figure 3.7A. spot #15) was excluded after verification of contamination with Cpx and/or Qz. Titanite grains (Ttn_1) within the Cpx-rich band (T3, T4, and T20; n=9/17) show low-Al cores with U concentrations of 2-7 ppm (average 4 ppm), a mean Th/U of 0.02, and an Al/Fe ratio of 3.91. These grains display a positive LREE/MREE slope ($[La/Sm]_N$ = 0.05) and flat to slightly negative HREE, indicative of metamorphic titanite (e.g., Aleinikoff et al., 2002; Olierook et al., 2019). The Eu anomaly in these grains is weakly negative to non-existent.

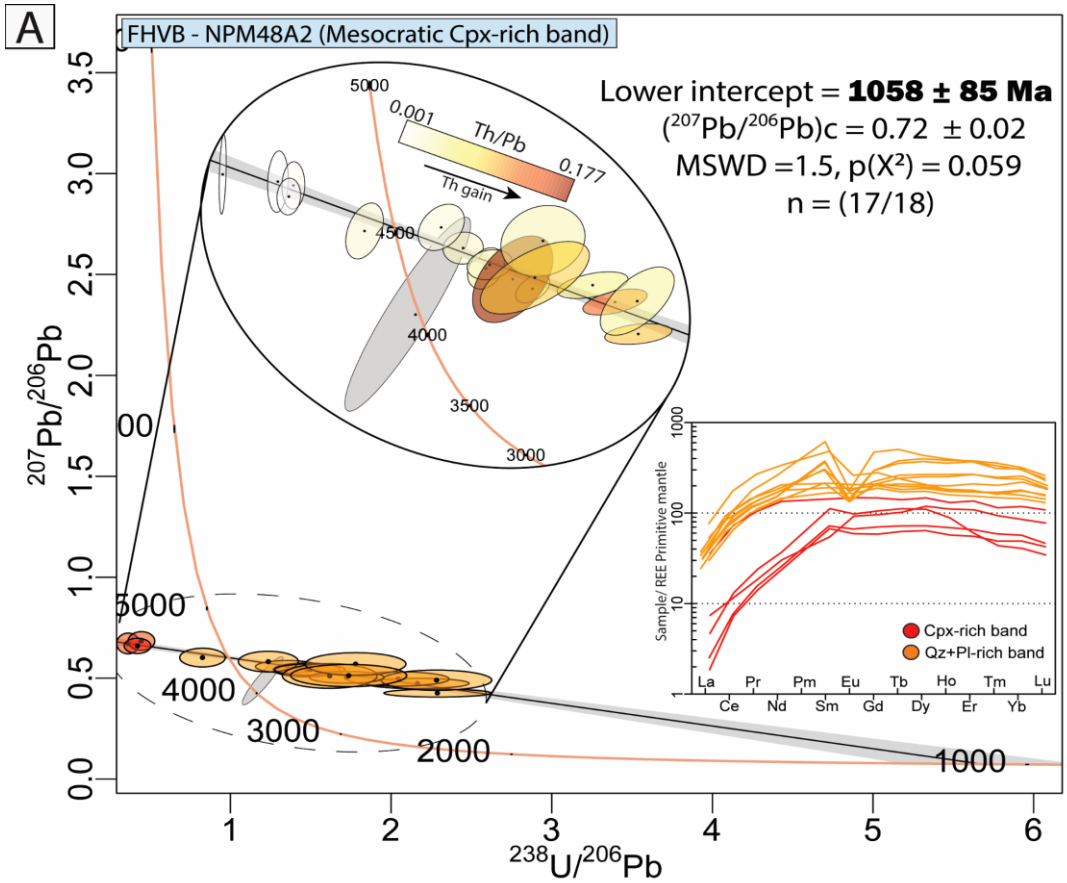

Figure 3.8. *A) Mesocratic Cpx-rich band (22NPM48A2) from the Hbl-Cpx schist of the FHVB domain; Tera-Wasserburg concordia plot colour-coded for LREE/HREE group. Inset: REE plot showing two chemical groups (red and orange) of titanite in the sample and Th/Pb ratio displaying an increase of Th toward the titanite located within the felsic bands, which display a negative Eu anomaly in the REE pattern. The grey ellipse represents excluded data because of high uncertainty.*

In the Qz+Pl-rich band (T11 and T14; n=8/17), titanites (Ttn_2) exhibit U levels of 26-51 ppm (average 37.77 ppm), a mean Th/U of 0.12, and an Al/Fe ratio of 5.13. These grains show a positive LREE/MREE trend ($[La/Sm]_N$ = 0.095) but with a distinct negative Eu anomaly ($[Eu/Eu^*]_N$ = 0.487), likely due to growth during Pl crystallization. These patterns are characteristic of metamorphic titanites (Aleinikoff et al., 2002; Olierook et al., 2019; and Kirkland et al., 2020) coeval with stable Pl. However, all titanite grains (both Ttn_1 and Ttn_2) analyzed in this sample yielded a lower intercept date of 1058 ± 85 Ma (MSWD = 1.6, $p(x^2)$ = 0.06) (Figure 3.8), interpreted as the age for the amphibolite-facies $S_{1\text{-}FHVB}$, Pl stable metamorphism in the mafic schist.

3.2.1.3 U-Pb Monazite

3.2.1.3.1 Sample 22EJT34A: Crn-Sil schist

The three monazite crystals are light brown to yellowish, with a subhedral, subrounded stubby shape, ranging from 150 to 250 μm in size. Compositional mapping (Th) reveals sector chemical and oscillatory zoning throughout the grains (M1, M2, and M3), with a rare resorption texture observed in the outer portion of grain M2 (Figure 3.9B). Such chemical zoning could indicate multiple growth episodes or compositional changes during metamorphism (Williams et al., 2007; Cherniak et al., 2008), while oscillatory zoning in monazite can result from fluctuations during mineral growth under metamorphic conditions (Engi, 2017).

Eleven analyses were carried out on the three grains, targeting the oscillatory zoning and outer portions; two discordant analyses were excluded. The remaining nine (n=9/11)

analyses yielded $^{206}Pb/^{238}U$ ages ranging from 1061 to 1034 Ma (Figure 3.9B). U content varies from 3002 to 6479 ppm, with the Th/U ratio ranging between 3.48 to 7.55, while trace elements exhibit a chondrite-normalized flat HREE pattern, likely attributed to Grt breakdown that enables HREE incorporation in monazite (Pyle et al., 2001; Kohn et al., 2004; Rubatto et al., 2006). The Eu anomaly reflects the Eu^{2+} retention in plagioclase during amphibolite-facies conditions (Bingen et al., 2001; Finger et al., 2009). These patterns are typical of metamorphic monazite (Williams et al., 2007). All nine concordant analyses yielded a $^{206}Pb/^{238}U$ weighted mean age of 1044 ± 5.1 Ma (n=9, MSWD=0.68), which is interpreted to represent growth during high-grade metamorphism in the FHVB domain.

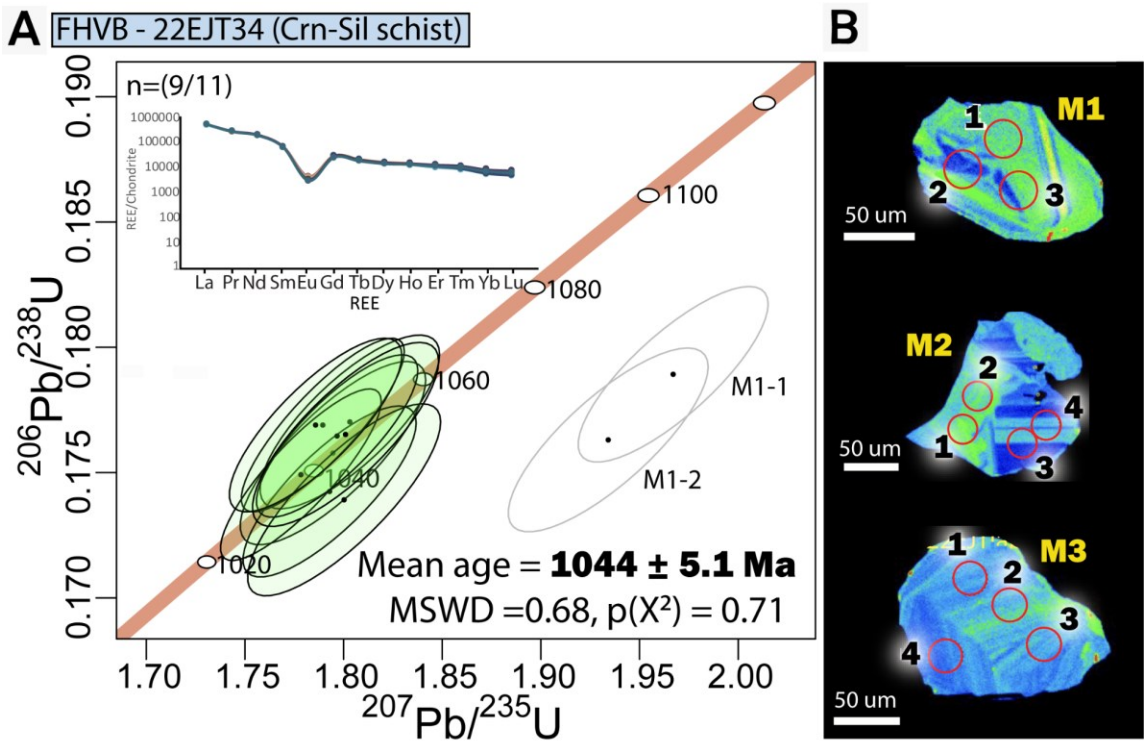

***Figure 3.9**. A) Wetherill concordia plot for monazite analyzed in the Crn-Sil schist (22EJT34), which defines a conspicuous cluster around 1.04 Ga. Inset REE data exhibiting a typical metamorphic pattern. B) Thorium maps displaying relative low (blue colour) and high (green colour) Th values, (red circles are ~25 µm in size). White ellipses are discordant and were removed from consideration.*

3.2.2 The Long Harbour shear zone (LHsz)

3.2.2.1 U-Pb Zircon

3.2.2.1.1 Sample 22NPM39B: Granodiorite gneiss

Zircon crystals range in size from 25 to 800 μm, occurring in colourless elongated tabular to acicular forms (aspect ratios between 3:1 and 7:1) and dark brown subrounded to subhedral crystals (3:1 and 2:1). Internal textures reveal clear core-rim relationships in the grains. The cores display rounded and resorbed composite margins with fine to broad-oscillatory texture (e.g., Figure 3.10A, #19, #30, #46) and patchy zoning (#61, #84, core close to spot #81). The rims, by contrast, overgrow cores and have a finer oscillatory texture (e.g., #18), as well as dark/bright patchy homogenous zoning, varying from 20 to 80 μm wide (e.g., #47, #60, #81, #85).

Eighty-four analyses were conducted on 71 zircon grains, targeting cores and rims. Of these, 45 analyses were concordant and considered further. Twenty-five of these 45 analyses represent cores, two displaying patchy zoning and low Th/U ratios (< 0.01) at 1621 and 1278 Ma, respectively. The remaining 23 cores exhibit broad sector/oscillatory zoning as well as homogeneous textures, with a concordant spread of $^{207}Pb/^{206}Pb$ dates ranging from 1792 to 1601 Ma and Th/U ratios between 1.06 and 0.40. Due to older dates and larger age spreading, the zircon cores are interpreted as inherited grains that experienced variable Pb-loss or isotopic mixing in a later overprint.

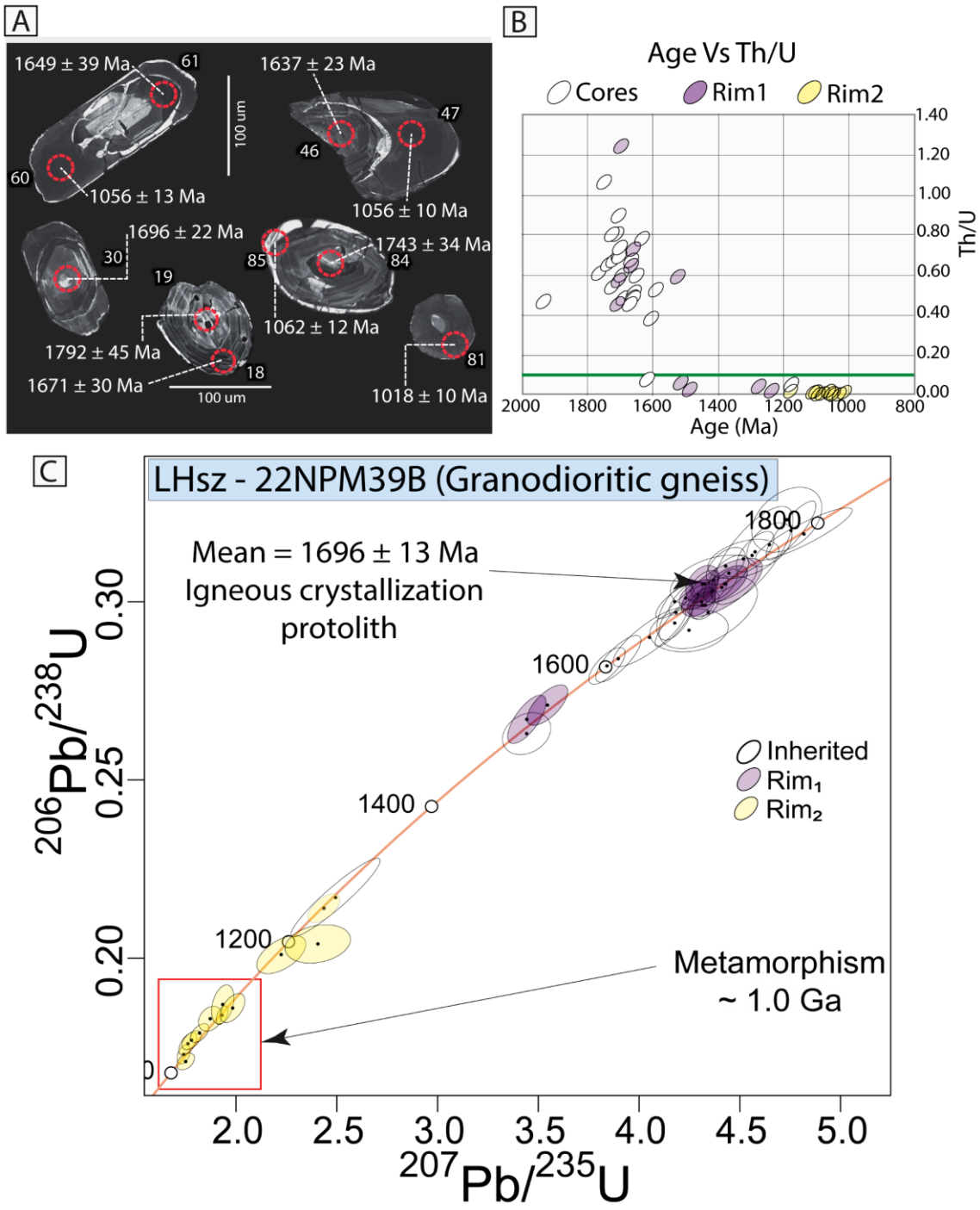

Figure 3.10. *Zircon U-Pb data from granodioritic gneiss 22NPM39B in the LHsz. A) Cathodoluminescence images of representative zircon grains displaying inherited cores, oscillatory overgrowths (rim$_1$), and dark patchy homogeneous Grenvillian (c.a. 1.0 Ga) rims (rim$_2$). Red dashed circles show the site of the 25 µm ablation pits. B) Age versus Th/U showing the decrease in both age and Th/U ratio, which suggests the spread in data reflects both igneous crystallization and a metamorphic overprint. C) Concordia plot showing the inherited igneous cores (unfilled ellipses) with associated age spread. The oscillatory zoned rims (rim$_1$, purple ellipses) show a cluster around 1.7 Ga and two analyses at 1.5 Ga. Homogenous younger rim$_2$ zircon (yellow ellipses) spread towards 1.0 Ga and have a metamorphic signature.*

Surrounding these core domains are oscillatory zoned rims (rim_1) (Figure 3.10A, #18 and #19), which display a conspicuous cluster around 1.7 Ga and spread to younger dates. The cluster around 1.7 Ga is defined by six of eight rim analyses (rim_1), with Th/U ratios ranging from 0.453 to 1.236 with dates ranging from 1720 to 1671 Ma. A weighted mean $^{207}Pb/^{206}Pb$ age of 1696 ± 13 Ma (MSWD=1.5, $p(x^2)$ =0.2, Figure 3.10C) is interpreted as the age of protolith crystallization due to tight age clustering and igneous elemental signatures. The two younger rim_1 analyses cluster around 1.5 Ga, possibly resulting from Pb-loss of the rim_1 population.

A younger grouping comprises 12 rims (rim_2) with dates that decrease with decreasing Th/U (Figure 3.10B) these rims display dark/bright patchy homogenous zoning with Th/U ratios below 0.1, suggesting metamorphic recrystallization. These rims include dates spanning from 1328 to 1018 Ma, showing a concordant array with a young cluster around 1.0 Ga. The spread in dates in this population may be the product of mixing with older zones; thus, the crystallization age of these metamorphic rims is approximated at 1.0 Ga (Figure 3.10C).

3.2.2.1.2 Sample 22NPM39A: Syn-deformational quartz-monzonitic dyke

Zircon crystals in this felsic dyke occur as light brown, subhedral crystals with aspect ratios of 5:1 to 3:1. Additionally, dark brown subrounded to subhedral crystals (4:1 and 2:1) and some stubby colourless grains; the grains vary in size from 25 to 200 µm. CL images reveal a clear core-rim relationship: cores appear bright and dark, exhibiting sector zoning (e.g., Figure 3.11B, #1, #11, #33), convolute texture (#4), and fine to broad

oscillatory overgrowths (#18, #34). The 20 to 40 μm wide rims display a patchy light-to-dark appearance (#2, #46) with a fine to broad oscillatory pattern (close to spot #11 and #44), while a resorption and rounding texture is visible at the boundary between the core and rims (close to spot #4).

Forty-nine analyses were conducted on 45 individual zircon grains, targeting both the cores and rims. Nineteen analyses were excluded due to discordance and high uncertainties, leaving 30 concordant analyses with dates ranging from 1791 and 1034 Ma (Figure 3.11A). Of these, 26 analyses correspond to cores with oscillatory zoning, bright/dark homogeneous patchy patterns, and convolute textures of blurred primary zoning, which span in $^{207}Pb/^{206}Pb$ dates from 1738 to 1331 Ma, with Th/U ratios between 1.50 and 0.07, suggesting an igneous origin based on their zonation and Th/U ratios.

The remaining four concordant analyses correspond to rims and fragments of whole grains (4/29), with ages ranging from 1.7 to 1.0 Ga. Two of these rims display broad oscillatory sector zoning, yielding dates of 1791 and 1316 Ma, with Th/U ratios of 0.54 and 0.56, respectively. The remaining rim and fragment exhibit a dark, homogeneous patchy pattern, with $^{207}Pb/^{206}Pb$ dates of 1383 and 1034 Ma, respectively, and Th/U ratios below 0.1.

Overall, all these dates spanning from 1.7 to 1.0 Ga in the cores and rims are likely inherited because they closely resemble the zircon ages, textures, and populations in the host rock sample (22NPM39B), and no obvious igneous crystallization zircon population can be inferred for these dykes. Thus, the crystallization age is constrained to around 1.0 Ga, in

which 1.0 Ga rims could have grown around inherited cores during metamorphism before or after dyke emplacement in the host rock.

3.2.2.1.3 Sample 22NPM40: Post-deformational monzogranitic dyke

Zircon crystals in this sample include thin, colourless to light brown acicular crystals with aspect ratios from 5:1 to 7:1, measuring 10 to 25 μm, as well as darker brown subhedral crystals with stubbier aspect ratios (4:1 to 2:1), varying from 20 to 300 μm (**Figure 3.11**D). Only a few acicular zircons survived the chemical abrasion and polishing process, making this population underrepresented. CL imaging reveals grains with clear core-rim relations; some display bright homogenous patchy zoning (e.g., Figure 3.11D, #9, #15, and #17) mantled by oscillatory zoning (e.g., #10). Other cores display sector zoning (#3) surrounded by patchy rims averaging 30 μm (#2). Most analyses correspond to zircon fragments, likely representing distinct cores or rims.

Fourteen analyses were conducted on 12 fragments and/or grains, yielded dates from 1885 to 951 Ma and defining a broad array with no distinct age clusters (Figure 3.11C). Of the seven concordant analyses, five correspond to cores with oscillatory and patchy zoning: four oscillatory cores yielded dates between 1748 and 951 Ma with Th/U ratio varying from 0.65 to 1.49, typical of igneous zircons. The youngest date (951 Ma) was obtained from a small acicular grain with the highest Th/U (1.48). The fifth core, with homogeneous patchy zoning, yielded a date of 1001 Ma and a Th/U of 0.09. The remaining two concordant analyses represent rims: one with oscillatory/patchy zoning and Th/U ratio of 0.70, with a

date of 1633 Ma, and the other with dark, patchy zoning and a Th/U < 0.1, and a date of 1040 Ma.

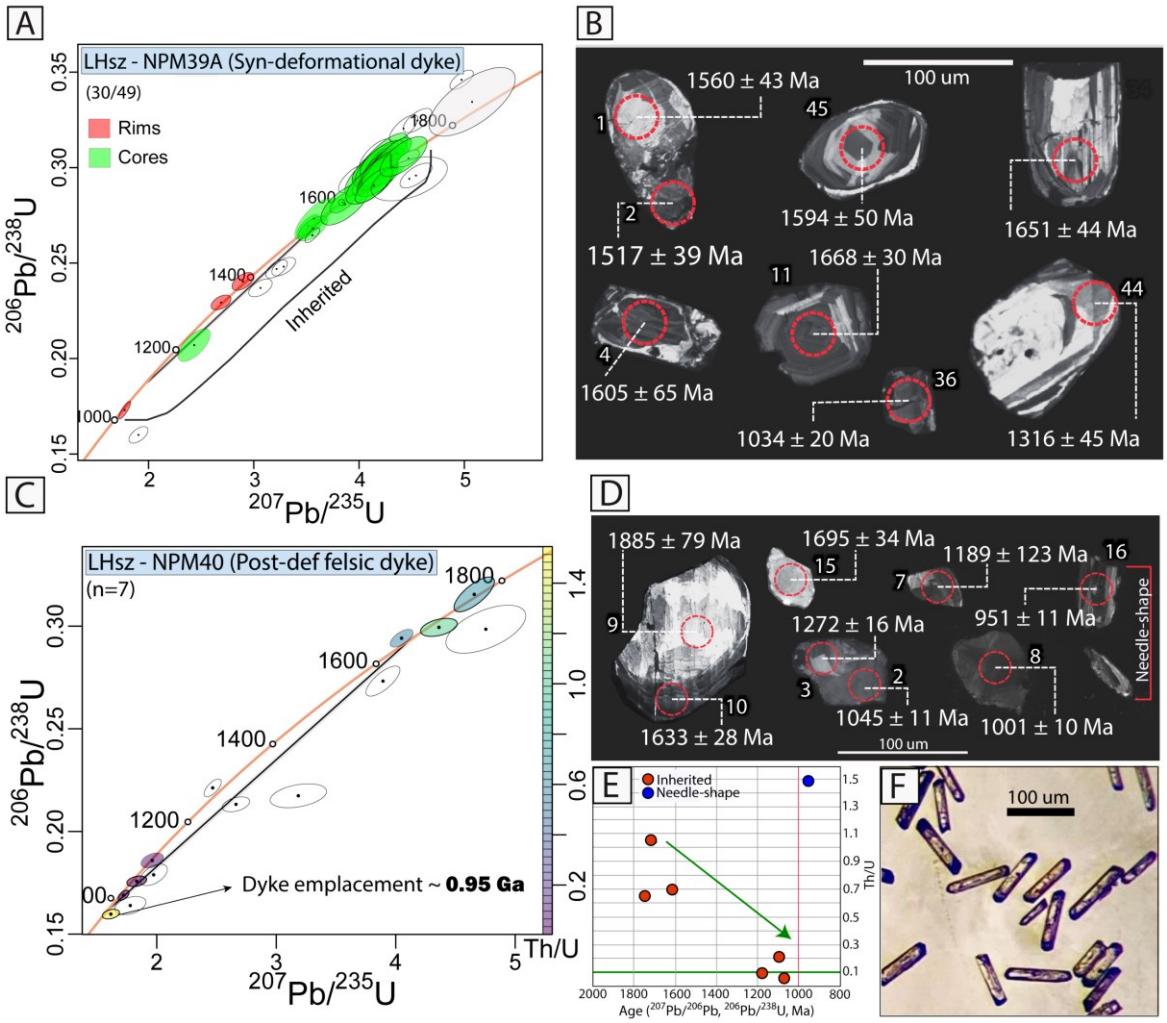

Figure 3.11. *Composite plot of zircon U-Pb CA-LA-ICPMS geochronological data and zircon CL images from the syn-deformational and post-deformational dykes in the LHsz. A) U-Pb zircon data for sample 22NPM39A plotted on a concordia diagram, showing a spread of inherited zircon grains that match host rock zircon (sample 22NPM39B) dates. Discordant and high-uncertainty data are shown in white ellipses. B) CL images showing the prismatic, stubby shapes along with oscillatory and patchy domains in inherited zircon grains. The red dashed circles denote the ablation pits (25 µm). C) U-Pb zircon data for sample 22NPM40 plotted on a concordia diagram, showing a large spread of dates likely inherited from the host rock, with dyke emplacement ca. 0.95 Ga. D) CL images showing domains of inherited grains and needle shapes with oscillatory domains in zircon. E) Age versus Th/U ratio of inherited grains from 22NPM40, exhibiting the high Th/U ratio for the needle-shape zircon. F) Small, thin, needle-shaped zircon grains related to the youngest igneous crystallization zircon population.*

The six oldest analyses roughly match the ages and population in the host granodiorite and are considered inherited grains. These analyses reflect a decrease in age and Th/U (indicated by the green arrow in Figure 3.11E). Only one needle-shaped grain exhibits a Th/U ratio value of 1.49 (reflecting an igneous composition), and the youngest age of 951 Ma; therefore, an age around 0.95 Ga is interpreted as dyke's emplacement age.

3.2.2.2 U-Pb Titanite

3.2.2.2.1 Sample 22NPM39B: Granodioritic gneiss.

Titanite grains range from 100 to 500 μm and exhibit a subhedral wedge to elongated rhomb shape. In BSE imaging and X-ray maps, Al, Fe, Ti, and Ce show various microstructures, such as sector zoning (e.g., Figure 3.12, T3, and T15), and complex lobate domains that penetrate inward from the grain edges (T8 and T13). Cerium and Fe maps in $S_{T\text{-}SLsz}$ parallel grains (T3 and T8) have low-Ce central regions and high-Ce outer margins (opposite pattern is observed in the Al and Ti maps) reflective of sector zoning (Figure 3.12, T15).

Seventeen spots targeted four grains along the Amp+Bt-rich and the Qz+Pl-rich bands. The central sector zoned domains from T3, T8, and T13 (light green circles in Figure 3.13) exhibit U content ranging from 96 to 619 ppm (average 241 ppm), Th/U ratio of 0.01, and a Th/Pb ratio of 0.04. The mean Al/Fe ratio is 2.13, with Al and Fe contents of 11428 ppm and 5359 ppm, respectively, resulting in an Al/Al+Fe ratio of 0.68; the REE patterns display a positive slope in LREE/MREE ($[La/Sm]_N = 0.09$) and a negative Eu anomaly ($[Eu/Eu^*]N = 0.61$), followed by a positive HREE slope (light green REE patterns in Figure 3.13).

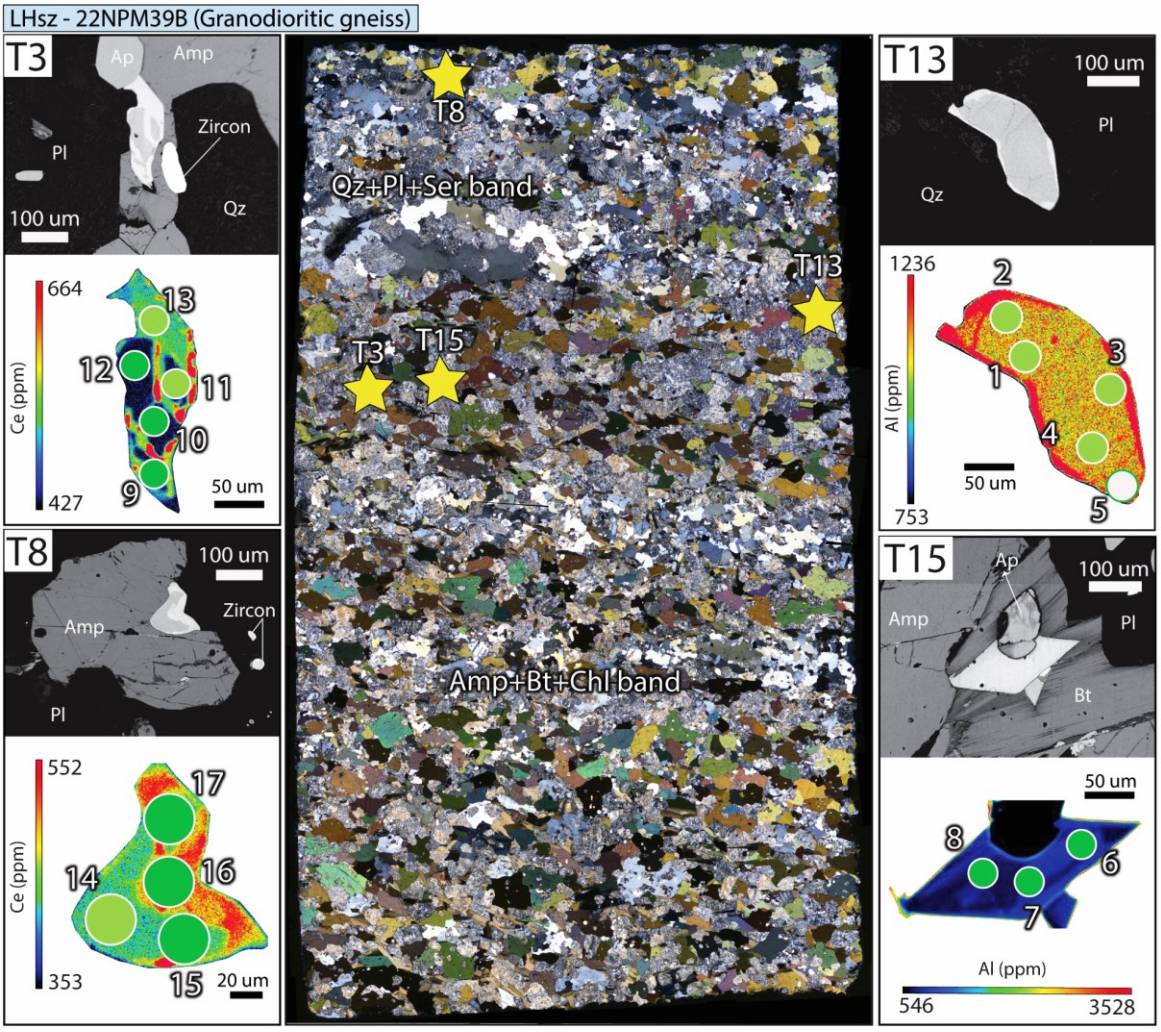

Figure 3.12. *Scan of the whole thin section in crossed polar (XPL) exhibiting the location of Ttn grains in the Bt+Amp-rich bands parallel to ST-LHsz (sample 22NPM39B, yellow stars); BSE images and EPMA X-ray elemental mapping of Ttn borders the photomicrograph. Scale bars are qualitatively relative to Al and Ce in the grains, while green spots are 30 µm diameter.*

The arbitrarily shaped outer margins of T3 and T8 (dark green circles in Figure 3.13) display higher Ce levels (861 ppm), a flatter to slightly negative slope in the HREE (dark green REE pattern Figure 3.13) within a more enriched LREE-HREE pattern (total REE of 6694 ppm), significantly higher than the central parts (1900 ppm). The Eu anomaly could be related to Pl growth and stability during metamorphism, while the concentration of the LREEs in titanite correlates with stable minerals containing LREEs as trace elements

(Scibiorski and Cawood, (2002), and references therein); in this sample, the alignment of allanite parallel to $S_{T\text{-}LHsz}$ likely influenced the crystallization process since Aln preferentially incorporates LREEs (Janots et al., 2008), leaving titanite with lower LREE. This geochemical variability in the sector-zoned grains is consistent with metamorphic or recrystallized titanite based on the geochemical discriminators used by Kowallis., et al. (1997), Aleinikoff et al. (2002), Olierook et al. (2019), and Scibiorski and Cawood, (2022).

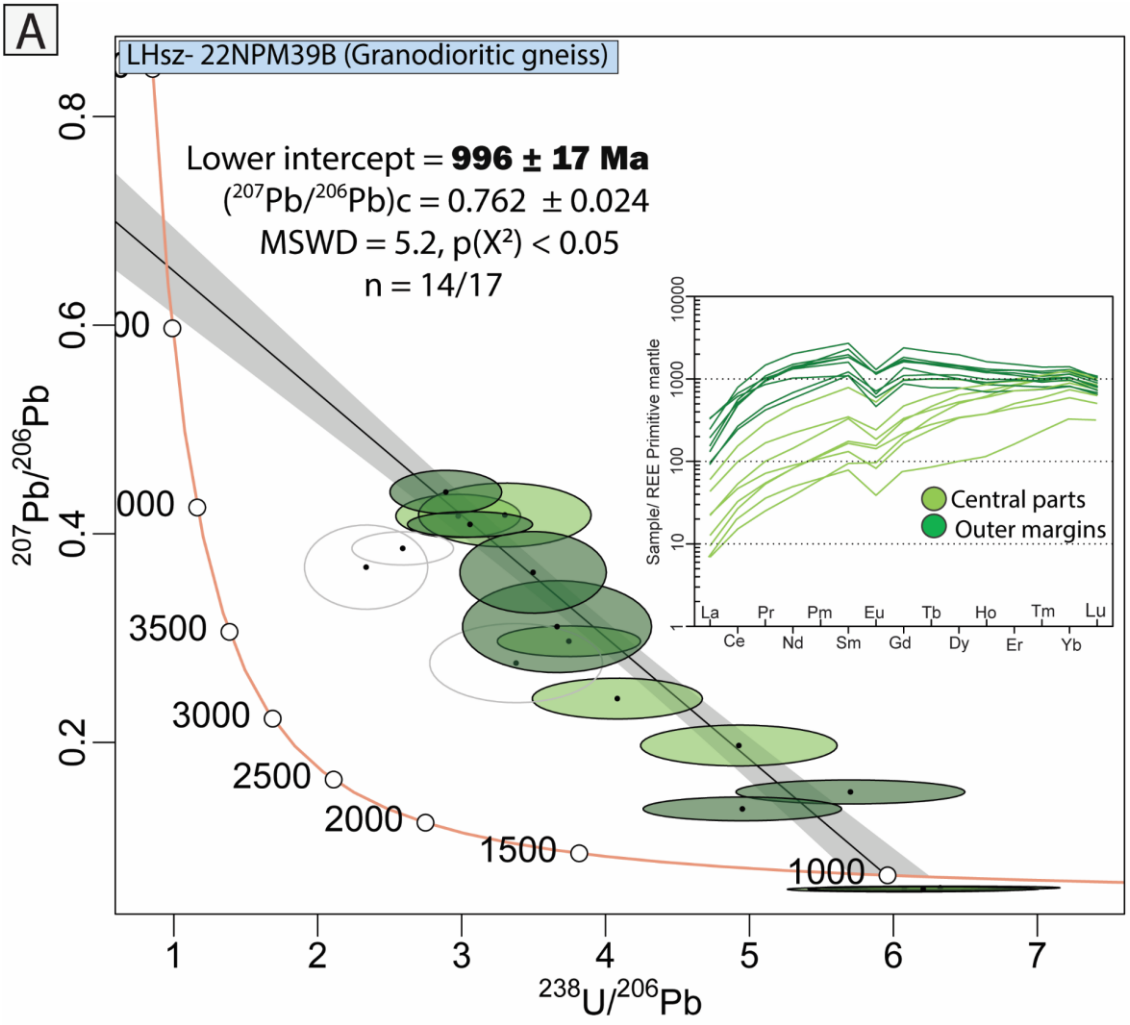

Figure 3.13. *Granodioritic gneiss (22NPM39B) from the LHsz; Tera-Wasserburg concordia plot colour-coded for LREE/HREE group. Inset: REE plot showing the central parts and outer margins from the Ttn analyzed (dark and light green). White ellipses represent the discordant analyses excluded.*

Even though all the titanites exhibit distinct geochemical zonation and trace element composition, the two chemical groups (inset Figure 3.13) plotted together form a linear trend in a Tera-Wasserburg diagram, with a lower intercept age of 1001 ± 18 Ma (MSWD = 15, $p(x^2) < 0.05$), suggesting Grenvillian crystallization but with significant overdispersion. After removing three older analyses, a regression line and a lower intercept age yields 996 ± 17 Ma (MSWD = 5.2, n=14/17). This age, around 1.0 Ga, is tentatively interpreted as the age of the titanite growth related to $S_{T\text{-}LHsz}$ during amphibolite to greenschist-facies shearing.

3.2.3 The St. Lewis shear zone (SLsz)

3.2.3.1 U-Pb Zircon

3.2.3.1.1 Sample 22NPM11: Mylonitic granodiorite

The zircon crystals vary from light to dark brown to colourless and exhibit subrounded, stubby to elongated crystals, with aspect ratios between 5:1 and 3:1. Their sizes vary from 25 to 400 μm. CL images reveal mostly a fine to broad sector/oscillatory and patchy zoning in the central part and outer margins of the grains (Figure 3.14B), typical of igneous growth. Some of these grains develop irregular bright domains that cut across oscillatory-zoned domains (e.g., Figure 3.14B, #57, #183). Nonetheless, a thinner (< 10 μm), bright, patchy rim is exhibited at the border of some of the grains, but they were not possible to ablate (e.g., Figure 3.14B, zircon grains exhibiting the spots # 10, # 63, and #183).

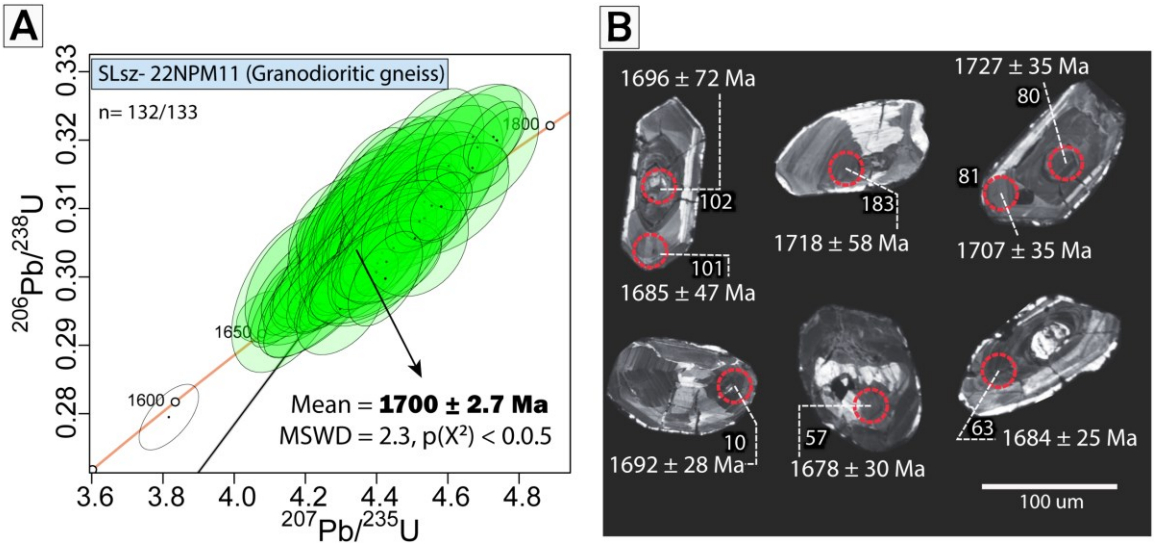

Figure 3.14. *A) Concordia diagram showing zircon U-Pb data from the SLsz granodioritic gneiss; the white ellipse was excluded from the age calculation. B) CL images of mostly oscillatory zoned zircon (red ellipse is ~25µm diametre).*

A total of one hundred eighty-two (182) analyses were conducted in 154 grains, targeting the central parts and outer margins of the grains. Forty-nine analyses were excluded from age calculation due to discordance. The remaining 133 concordant analyses exhibit sector and fine-to-broad oscillatory zoning, with dates clustering between 1756 and 1609 Ma (**Figure 3.14**A) and Th/U ratios varying from 1.43 to 0.26. The youngest concordant date of 1604 Ma was excluded (Grey ellipse) due to lack of age clustering. The final set of 132 analyses yielded a weighted mean $^{207}Pb/^{206}Pb$ age of 1700 ± 2.7 Ma (n=132, MSWD = 2.3) with an average Th/U ratio of 0.72, which is interpreted to represent the protolith crystallization age of the granodiorite.

3.2.3.2 U-Pb Titanite

3.2.3.2.1 Sample 22NPM11: Mylonitic granodiorite.

Titanite grains occur as large subhedral porphyroclasts aligned parallel with the $S_{T\text{-}SLsz}$ fabric (Figure 3.15B), ranging from 100 to 800 μm in size and form subrounded to elongated rhombic shapes. Titanites display internal fluid-assisted dissolution-reprecipitation textures (i.e., Moser et al., 2022) between brown cores and lighter rims. The cores feature convex, lobate, and cuspate borders extending inward from the grain edges (e.g., Figure 3.15A, T7, T14, and T26). BSE images and EPMA X-ray mapping of five titanite grains (n=5) reveal sector zoning and dissolution-reprecipitation microstructures. The cores exhibit sharp to transitional compositional domains, with elevated concentrations of Ce, Fe, and Zr, which decrease toward the rims (T18 and T26), while Al-mapping shows an inverse pattern, with low-Al cores transitioning to high-Al rims.

Forty-six U-Pb and trace elements analyses were conducted on the sector zones and reprecipitated domains of the selected titanite grains across the thin section. The sector zone domains (n=32/46) exhibit an average Ce concentration of 4875 ppm, with high LREE displaying a flat to negative slope (mean $[La/Sm]_N$ of 1.61) and a negative Eu anomaly ([Eu/Eu*]N = 0.82). HREE concentrations exhibit a flat pattern, with a mean $[Eu/Yb]_N$ of 1.09 and a total REE average of 11996 ppm. U content of 701.4 ppm, and Th concentrations of 305 ppm, yielding a Th/U ratio of 0.51, and a Th/Pb ratio of 1.80. The Al/Fe ratio is 1.15, with Al and Fe contents of 10910 ppm and 12385 ppm, respectively, resulting in an Al/Al+Fe ratio of 0.47 and a Zr content of 693 ppm. All these trace element signatures are

typical of igneous titanites (e.g., Aleinikoff et al., 2002; Olierook et al., 2019; Kirkland et al., 2020).

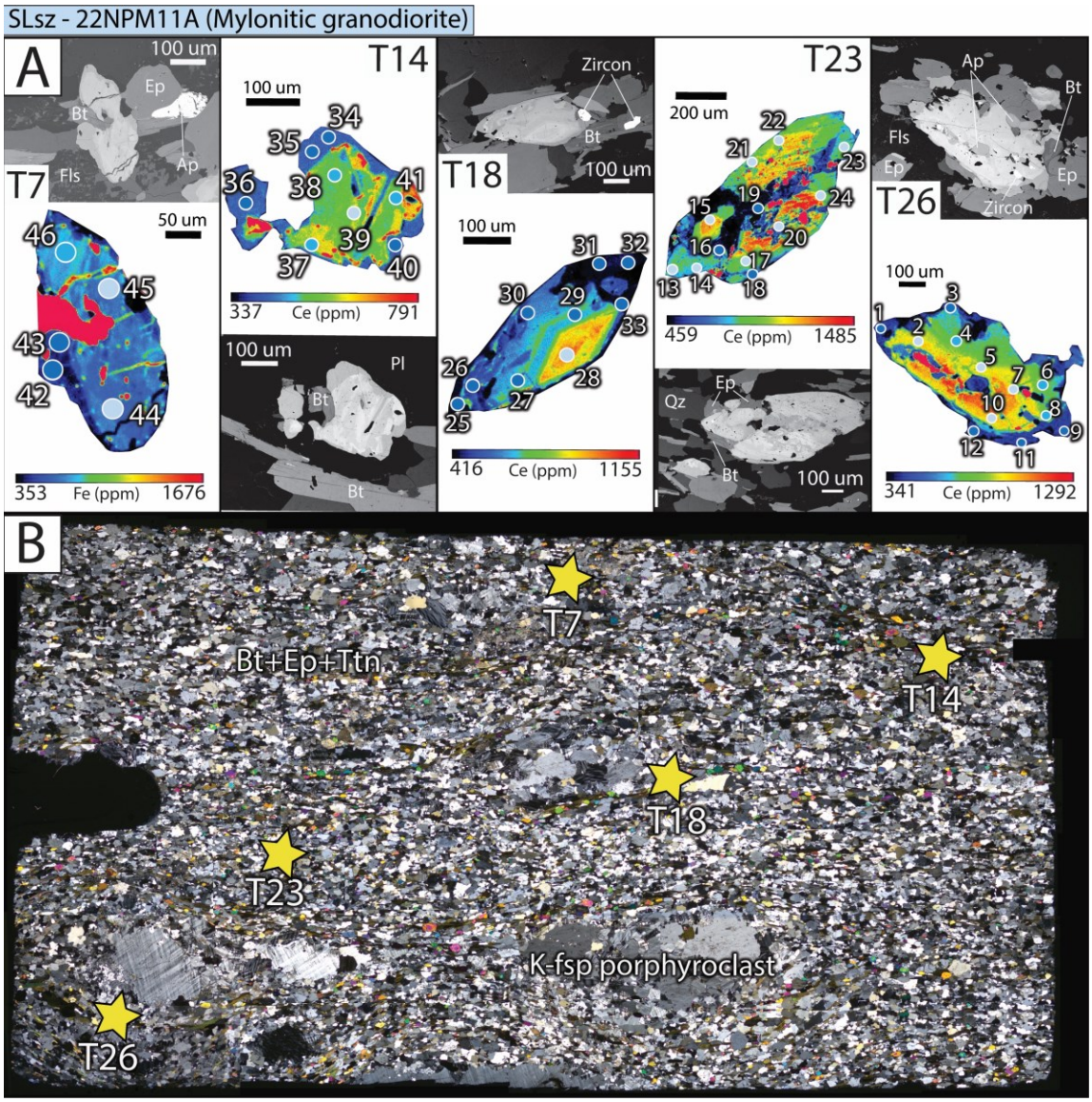

Figure 3.15. *A) BSE images and EPMA X-ray elemental mapping in Ttn grains (sample 22NPM11A) display Cerium (Ce) zonation with growth zoning (T18 and T26) and dissolution-reprecipitation (T7, T14 and T26) microstructures. BSE images show the mineralogical relationship of Ttn to Bt, Ap, and Zrn inclusions (T26). B) Scan of the whole thin section in crossed polar (XPL) exhibiting location of the titanite grains analyzed in the mylonitic granodiorite from the SLsz (Ttn = yellow stars).*

Regarding the outer reprecipitated domains (n=13/46), they exhibit a lower Ce concentration (422.6 ppm) and LREE with a flat to positive slope ($[La/Sm]_N$ of 1.65). A positive Eu anomaly ($[Eu/Eu^*]_N = 2.2$) and a positive MREE/HREE slope (dark blue circles and REE pattern in inset Figure 3.16). The average total of REE is 1202 ppm, significantly lower than the sector zone domains (11996 ppm). U content of 118 ppm, Th/U ratio of 0.156, lower Th/Pb ratio of 0.39, and the mean Al/Fe ratio is 1.74, with Al and Fe contents of 15766 ppm and 9796 ppm, respectively, resulting in an Al/Al+Fe ratio of 0.63 and a lower Zr content of 89 ppm. The positive Eu anomaly could be attributed to the breakdown of Pl during titanite growth, while the transition from flat HREE to a positive slope suggests that titanite rims grew in conjunction with another LREE-bearing phase like epidote or apatite, which both are aligned and parallel to $S_{T\text{-}SLsz.}$

The spread of U-Pb data (n=46) shows an array where most sector-zoned cores are concordant, and spread in dates from c.a. 1.7 to 1.1 Ga, while the reprecipitated outer margins exhibit a more discordant array (light and dark blue ellipses, Figure 3.16). One anomalous rim analysis at ~ 3.8 Ga was excluded due to contamination with epidote (T26, spot #9). The remaining 45 analyses form a triangular array, similar to that described by Olierook et al. (2019), with a $^{207}Pb/^{206}Pb$ ordinate common-Pb intercept and two discordia intercepts. Based on the textural and chemical grouping, previously described sector-zoned cores with an igneous signature represent the first discordia intercept at ~ 1.7 Ga, consistent with the protolith zircon age of 1700 ± 2.7 Ma. This entire array is variably modified to higher $^{238}U/^{206}Pb$ ratios resulting in a mixing zone enveloped by the ~1.7 Ga and 1.1 Ga arrays. This suggests that sector-zoned cores and outer margins of all the igneous ~1.7 Ga

titanite grains have undergone isotopic resetting to a maximum age of 1.1 Ga or younger (Figure 3.16).

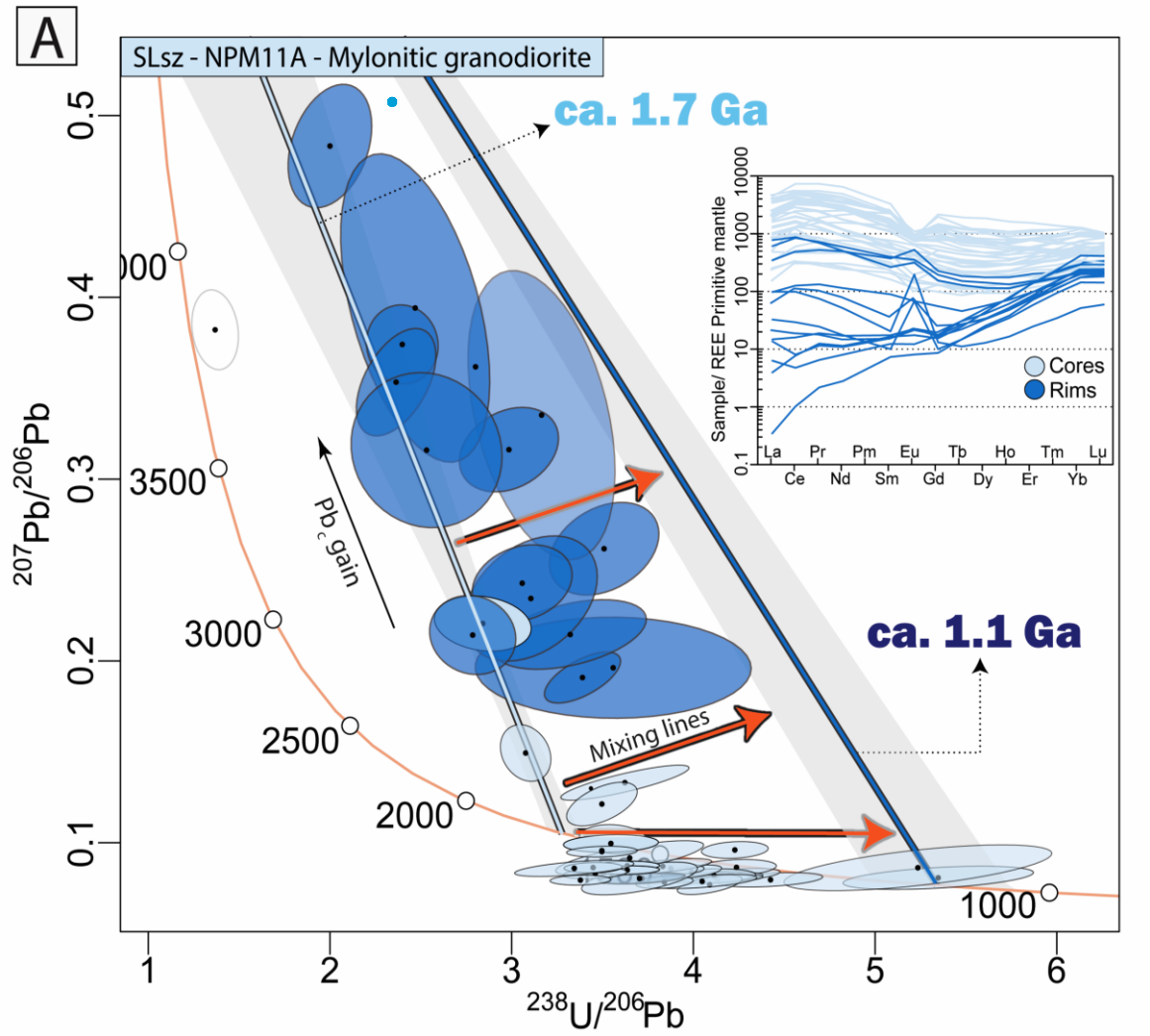

Figure 3.16. *A) Sample 22NPM11A from the St. Lewis shear zone; Tera-Wasserburg concordia plot colour-coded for LREE/HREE group. Inset: Titanite REE plot pattern showing the igneous cores (light blue) and the reprecipitated rims (dark blue). Both populations are reset and display an array of crystallization around 1.7 Ga and younger Grenvillian recrystallization.*

3.2.4 The Fox Harbour shear zone (FHsz)

3.2.4.1 U-Pb Zircon

3.2.4.1.2 Sample 22NPM33: Mylonitic diorite dyke

The zircon crystals are light brown to colourless and show sub-rounded stubby and elongated morphologies (aspect ratio 3:1) ranging in size from 40 to 200 μm. CL images reveal bright sector oscillatory zoning in the central parts of the grains transitioning to fine oscillatory texture towards the outer margins, typical of decreasing Zr saturation during igneous growth (e.g., Figure 3.17B, spot #17, #27). Moreover, dark sector/oscillatory zoning is also exhibited with irregular growth-zoned domains in some cores or central parts mantled by rims or outer margins displaying a light grey fine oscillatory zoning (e.g., spot #9, #42, #43). However, a bright white-to-grey, homogeneous patchy rim of 10 to 15 μm surrounds the oscillatory zoned grains (e.g., grains with spots #18 and #19).

Forty-seven analyses were carried out on 52 grains, targeting the central and outer margins of the zircon grains. Twenty-one analyses were excluded due to discordance. The remaining 26 analyses yielded $^{206}Pb/^{238}U$ dates ranging from 1127 to 1045 Ma (Figure 3.17A), exhibiting a bright fine-to-broad oscillatory sector zoning and a dark sector zoning with Th/U ratios ranging from 1.76 to 0.10 (igneous zircons). Based on textures and Th/U contents, these analyses represent a single population that yielded a weighted mean $^{206}Pb/^{238}Pb$ date of 1079 ± 9 Ma (MSWD = 1.6, p(x2) = 0.03, **Figure 3.17**). This date is interpreted as the crystallization age of zircon and the emplacement of the mafic dyke.

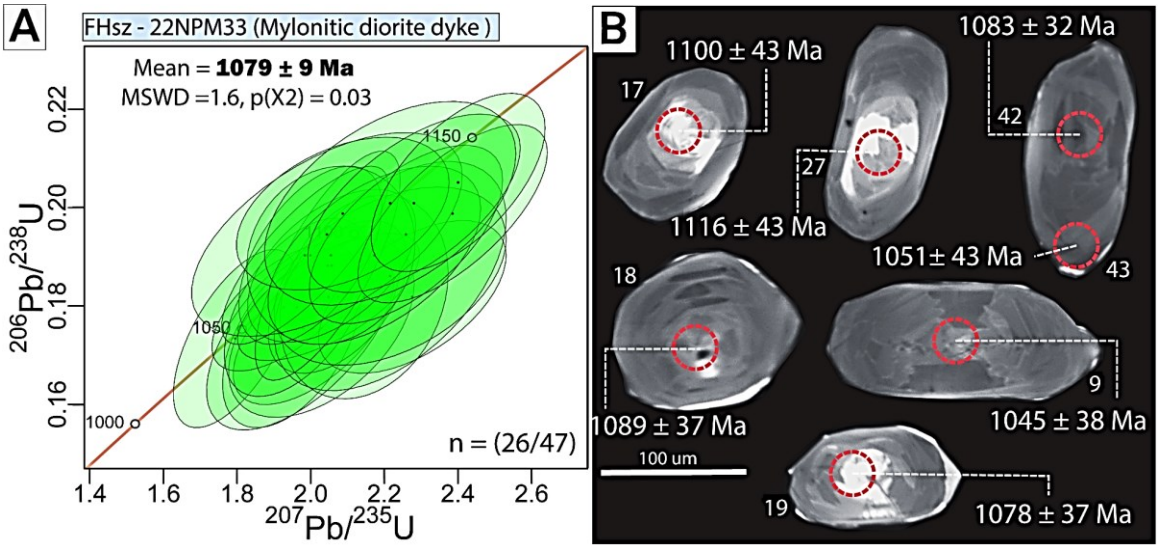

Figure 3.17. *A) Concordia diagram showing zircon U-Pb CA LA-ICPMS from the deformed diorite dyke; green ellipses representing the central parts and outer margins of the whole grains with oscillatory zoning with a weighted mean $^{206}Pb/^{238}Pb$ crystallization age of 1079 Ma. B) CL images of whole grains with their respective $^{206}Pb/^{238}Pb$ dates (red ellipses are ~30μm). Grains display bright and dark sector oscillatory zoning (#17, #27), some mantled by a thin, bright white-to-grey patchy homogenous rim that was not analyzed.*

Chapter 4 Discussion and Interpretation

4.1.1 Basement Ages (1.7 - 1.5 Ga)

Zircon geochronology of the LHsz and SLsz host rocks (22NPM39B and 22NPM11) indicate these rocks were predominantly formed during early Labradorian orogenesis at approximately 1.7 Ga (Figure 3.10 and Figure 3.14). This protolith age is further corroborated by the U-Pb dating of titanite grains from mylonitic granodiorite in the SLsz, which yielded a weighted mean crystallization age of ~ 1.7 Ga (Figure 3.16). These titanites display sector zoning and trace element patterns characteristic of igneous growth (e.g., Aleinikoff et al., 2002; Olierook et al., 2019; Kirkland et al., 2020) and currently manifest as rotated porphyroclasts within the $S_{T\text{-}SLsz}$, indicating growth prior to pervasive dynamic recrystallization. The protolith-aged titanite in the SLsz is enriched in LREE and exhibits a negative Eu anomaly (Figure 3.16), reflecting titanite growth in conjunction with stable plagioclase during the protolith crystallization. Furthermore, igneous titanite typically forms late in the crystallization sequence, by which time LREEs are incorporated into titanite after being concentrated in the residual melt (Kohn, 2017; Scibiorski and Cawood, 2022).

Previously, the only reported early Labradorian basement rock in Eastern Grenville was a 1709 Ma granodiorite with anatectic melt pods at Cuff Island in the Groswater Bay terrane (Scharer et al., 1986), approximately 75 km east of Rigolet and 230 km to the N-NW of St. Lewis (Figure 1.1). However, the new zircon and titanite ages herein suggest early Labradorian magmatic activity extended to the southeastern LMT/MMT, specifically up to

the northern PT boundary. Additionally, Labradorian ages within the LMT have been previously reported in orthogneiss with protolith ages of 1678 and 1677 Ma (Gower et al., 1992) and minor Labradorian granitic intrusions (1664-1644 Ma) that underwent amphibolite-facies deformation similar to their host rocks (Scott et al., 1993).

In the FHVB domain, foliated to gneissic megacrystic/porphyritic granitic to granodioritic augen-gneiss represents part of the basement to the FHVB. Protolith crystallization ages from samples collected to the north and south of the three mineralized horizons are 1516 ± 12 Ma (22NPM03) and around 1.6 Ga (22NPM22), respectively (Figure 3.1and Figure 4.1). Miller (2015) proposed that these gneissic rocks belong to the FHVB and called the entire package the Fox Harbour domain. However, Gower (2019) argued that the FHVB rocks intruded into an older gneissic basement based on the similarities of these gneissic rocks with other gneisses in the MMT and LMT. The crystallization ages obtained in this work (~1.6-1.5 Ga) further support the interpretation that the FHVB basement formed during late Labradorian to Pinwarian magmatic events (Figure 4.2), consistent with protolith ages in the broader LMT and MMT.

4.1.2 The Fox Harbour Volcanic Belt (~ 1.3 Ga)

The FHVB rocks exhibit pervasive mylonitization and metamorphism, obscuring their original volcanic textures and complicating protolith identification. However, Haley (2014) and Gower (2019) proposed a volcanic protolith based on the presence of mafic and felsic units, quartzite, metasedimentary layers interpreted as volcaniclastic deposits, and epidote pods in the mafic sequences, which may signify alteration pipes or pillow

structures. Haley (2014) classified the felsic rocks as peralkaline rhyolites enriched in REE, which crystallized ~ 1.3 Ga (Haley, 2014; Magyarosi and Rayner, 2023). However, the crystallization and deposition ages of the associated mafic units and quartzite layers were not constrained, leaving some ambiguity to the supracrustal nature of the package.

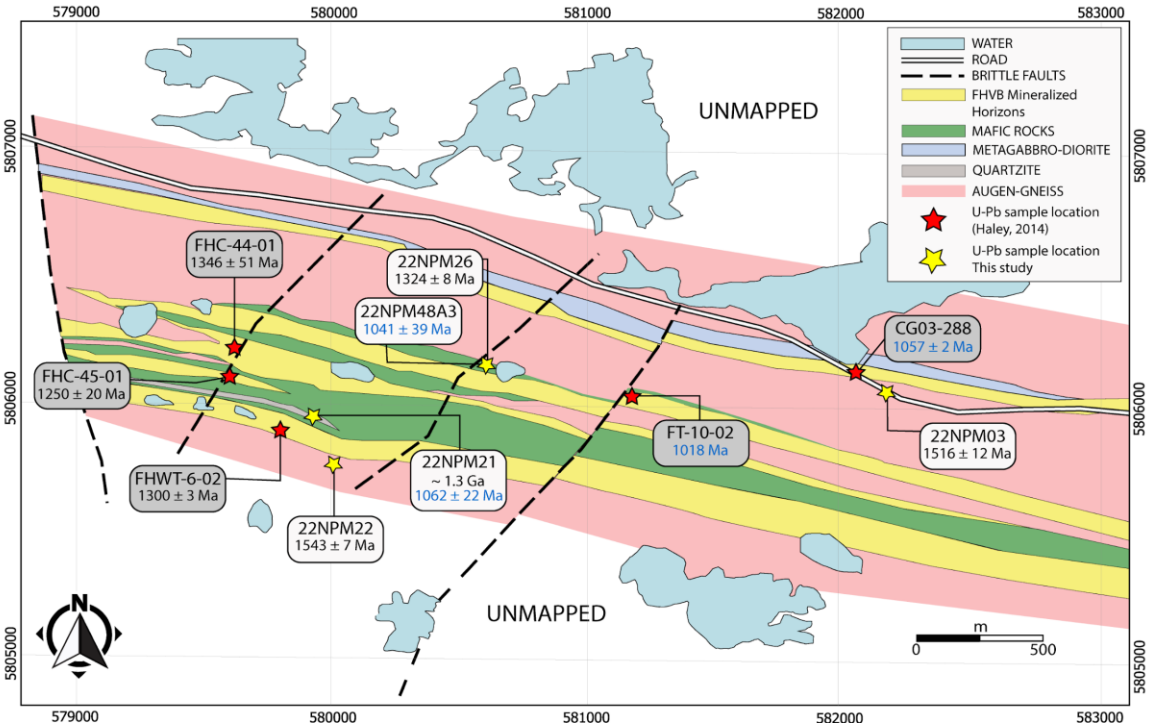

Figure 4.1. *Geology map of the Foxtrot Deposit displaying the mineralized FHVB (yellow) intercalated with the mafic and siliciclastic related units (Modified from Haley, 2014). U-Pb zircon ages in black colour represent igneous crystallization, and the blue text represents metamorphic ages.*

New ages presented herein from Grt-bearing leucodiorite layers that intrude these mafic schists (22NPM26 and 22NPM01) yielded minimum crystallization ages of 1324 ± 8 Ma in the Foxtrot area and ~ 1.3 Ga in the Deep Fox area (Figure 3.2 and Figure 4.1). These new minimum ages for mafic schists overlap with most of the previously reported felsic ages including a CA-TIMS age of 1300 ± 2.5 Ma in the southern zone, LA-ICP-MS ages 1346 ± 51 Ma and 1250 ± 20 Ma in the central and northern zone of the Foxtrot area (Haley

2014), and 1314 ± 12 Ma and 1269 ± 10 Ma for rhyolites (Magyarosi and Rayner, 2023) ~ 10 km farther east in the Deep Fox area. The approximately 50-million-year age difference (from ~ 1.31 to 1.26 Ga), evidenced in the leucodiorites and the mineralized felsic FHVB indicates more than one magmatic pulse in a long-lived and reactivated magmatic system associated with REE-enriched magmas (Magyarosi and Rayner, 2023). Additionally, the meter-thick quartzite layer (22NPM21) from the southern portion of the FHVB yielded a maximum depositional age of approximately 1.3 Ga, further supporting a supracrustal origin for the FHVB (Figure 3.3 and Figure 4.1).

Provenance analysis from the quartzite reveals a Laurentian margin signature, with Archean (3.4 and 2.7 Ga), Paleoproterozoic (1.98 and 1.80 Ga), and Mesoproterozoic populations at around 1.42 Ga. These ages are attributed to the basement terranes throughout Labrador and Quebec (e.g., Gower et al., 1997; Gower, 2019). Such a wide range of ages is also characteristic of extensional environments, where detritus is sourced broadly from the surrounding region (e.g., Cawood et al., 2012).

The overlapping ages of quartzite deposition, leucodiorite emplacement, and rhyolite deposition (Haley, 2014; Magyarosi and Rayner, 2023), along with their lithological, textural, and geochemical similarities, suggest the FHVB represents a supracrustal bimodal volcano-sedimentary sequence deposited around 1.3 Ga in an extensional environment along the Laurentian margin atop the Labradorian-Pinwarian basement (Figure 3.3 and Figure 4.3A). Regionally, the ~ 1.3 Ga activity is coeval with the 1296 Ma Upper North River syenite (Brooks, 1984) in the LMT, while the younger deposition age (~ 1260 Ma) overlaps with the 1250 Ma Mealy dykes (Emslie et al., 1984) in the MMT. Both events

align with the anorogenic Elsonian tectonomagmatic episode and are potentially linked to widespread extension and rifting along the Laurentian margin during this period (Gower and Tucker, 1994; Gower, 2019).

4.1.3 Grenvillian Deformation and Metamorphism

4.1.3.1 Peak Metamorphism (D1) and early Deformation (D2)

In the FHVB domain, both the 1.6–1.5 Ga augen-gneiss and the 1.3 Ga FHVB sequence exhibit pervasive mylonitization characterized by aligned Bt+Amp and stretched Qz+Fsp layers. While the augen-gneiss lacks diagnostic mineral assemblages of high-temperature metamorphism, the FHVB rocks reflect peak amphibolite-facies metamorphism ($S_{1\text{-FHVB}}$), evidenced by Grt-bearing leucosomes and Hbl+Bt after primary Cpx within the mafic-schist (22NPM48A3). High-grade metamorphism is also recorded in the Crn+Sil schist (22EJT34) at the boundary between the FHVB domain and the FHsz. While the relationship between this schist and FHVB rocks remains uncertain, monazite growth during retrograde metamorphism, potentially associated with anatectic crystallization during post-peak cooling (e.g., Kohn, 2014), may provide insights into their metamorphic history.

The leucosomes (22NPM48A3) crystallized at 1041 ± 39 Ma, overlapping in age with the metamorphic zircon population in the FHVB quartzite (22NPM21) ~ 1.06 Ga and the monazite age from Crn+Sil schist (22EJT34) at 1044 ± 5 Ma. In the mafic schist, disseminated titanite, associated with Hbl+Bt and aligned with $S_{1\text{-FHVB}}$ in the mesocratic band (22NPM48A2), exhibits metamorphic Al/Fe ratios and REE patterns (e.g., Aleinikoff

et al., 2002; Olierook et al., 2019; Kirkland et al., 2020). The negative Eu anomaly suggests plagioclase stability during peak metamorphism coinciding with the titanite crystallization at 1058 ± 85 Ma (Figure 3.8), which directly records the amphibolite-facies $S_{1\text{-FHVB}}$ fabric formation in the mafic sequence. Together, these metamorphic ages define the early high-temperature metamorphism and $S_{1\text{-FHVB}}$ (D1) around 1.06-1.04 Ga (Figure 4.2 and Table 4-1). These new zircon, titanite, and monazite ages overlap with previously reported U-Pb zircon metamorphic ages of ~ 1.05 Ga in rhyolite of the FHVB (Haley, 2014). They also overlap with metamorphic zircon ages of 1066 ± 8 Ma (mineralized FHVB), 1038 ± 29, and 1031 ± 15 Ma (rhyolite and leucogabbro, respectively), associated with the FHVB in the Deep fox area (Magyarosi and Rayner, 2023).

The 1.06-1.04 Ga high-temperature metamorphism and deformation (D1) in the FHVB domain evolved over time, which is reflected in tight-to-isoclinal folding of the anatectic Grt-bearing leucosomes, with axial planar foliation $S_{2\text{-FHVB}}$ aligned parallel to $S_{1\text{-FHVB}}$ forming a composite $S_{1/2\text{-FHVB}}$ fabric. This post-peak metamorphism (D2) is characterized by a combination of shear folds, buckle-folding geometry, and some later homogenous pure shear strain exhibited by thin and attenuated limbs characteristic of Class 1C folds (e.g., Fossen, 2017).

In the FHVB domain, this D2 event is likely coeval with observed right-lateral simple shear, where $S_{1/2\text{-FHVB}}$ fabric was formed at temperatures ~ 650 °C, based on the medium- to high-grade mylonitic quartz textures. This is evident as well in deformed amazonite-bearing pegmatites (Figure 2.2D), which are texturally similar to, and likely related to the 1024 Ma amazonite pegmatites (Kamo et al., 2011) on Battle Island, located approximately

10 km southeast of the study area. This relationship suggests that pervasive ductile shear during D2 persisted until at least 1.02 Ga. These structural and metamorphic features indicate that the FHVB and its basement rocks were significantly influenced by suprasolidus metamorphism (D1) ~1.06-1.04 and renewed subsolidus folding and homogenous shear strain (D2) sometime between 1.04-1.02 Ga (Table 4-1).

4.1.3.2 Late Grenvillian Deformation (1.02 - 0.98 Ga)

4.1.3.2.1 Thrusting and Strain Localization (D3)

The ~ 1.7 Ga granodioritic host rocks in the LHsz and SLsz (22NPM39B and 22NPM11) exhibit distinct geophysical anomalies and transposition foliations ($S_{T\text{-}LHsz}$ and $S_{T\text{-}SLsz}$) characterized by gneissic banding with aligned amphibole and biotite. These rocks are variably mylonitic and display medium-to-high grade (500–650 °C) quartz microstructures (Figure 2.9C-D). Overprinting these earlier features are randomly oriented and aligned retrograde metamorphic minerals such as Chl+Ep+Ttn±Aln±Czs and sericite replacing Pl+Kfs. These retrograde assemblages define ($S_{T\text{-}LHsz}$ and $S_{T\text{-}SLsz}$) and reflect a lower temperature strain evolution within a later greenschist-facies reverse oblique-slip shear system.

The 1.7 Ga igneous titanites in $S_{T\text{-}SLsz}$ are partially reset to a recrystallization event with a maximum age of 1.1 Ga (Figure 3.16). Lobate outer margins of titanites, consistent with interface-coupled dissolution–reprecipitation textures (e.g., Moser et al., 2022), display a positive Eu anomaly and a lower LREE content (Figure 3.15 and Figure 3.16). These features are attributed to plagioclase breakdown (from $S_{T\text{-}SLsz}$) and the formation of new

minerals, such as Aln+Ep, alongside reprecipitated titanite margins, influencing LREE sequestration during the $S_{T\text{-}SLsz}$ formation.

The granodioritic host rock (22NPM39B) in the LHsz exhibits metamorphic zircon rims with patchy texture and Th/U ratios < 0.1, yielding a spread of Grenvillian ages (~1.0 Ga; Figure 3.10). The quartz-monzonitic syn-deformational dyke (22NPM39A) in the LHsz exhibits a sharp intrusive contact with the mylonitic granodiorite and contains inherited zircon grains with ages, textures, and populations similar to those in the host rock (33NPM39B). This relationship suggests the felsic dyke intruded before the 1.0 Ga metamorphism, and the 1.0 Ga metamorphic zircon rims grew (on inherited grains) after dyke emplacement. Titanites aligned with retrograde lower amphibolite to greenschist-facies deformation $S_{T\text{-}LHsz}$ yielded a U-Pb age around 1.0 Ga and display metamorphic trace element signatures (Figure 3.13), including LREE depletion linked to Aln+Czs growth parallel to $S_{T\text{-}LHsz}$ and a negative Eu anomaly from Pl stability or formation consistent with amphibolite-facies metamorphism.

The LHsz and SLsz are likely coeval shear structures, as evidenced by their parallel orientation, geophysical signatures, spatial proximity, intense high-strain fabrics, similar metamorphic grades, and kinematics (Figure 2.1, Figure 2.6, and Figure 2.8). Both shear zones exhibit high-strain transposition fabrics ($S_{T\text{-}LHsz}$ and $S_{T\text{-}SLsz}$) with moderate NW-plunging transport directions and a reverse oblique shear sense (north-side-up to southeast) at ~1.0 Ga, consistent with previous kinematic interpretations in the LHsz (Hanmer and Scott, 1990; Gower, 2005). Previously, Hanmer & Scott (1990) classified the LHsz as a high-grade mylonite, and Scott et al. (1993) reported a zircon U-Pb lower intercept age of

1509 ± 12 Ma for a syn-deformational aplitic vein in amphibolite-facies straight gneiss (red star S401; Figure 2.1). This age, interpreted as the minimum deformation age along the southern LMT margin, may instead reflect inherited zircon grains (and thus a maximum age) based on the inheritance observed in samples herein of the felsic deformed and undeformed dykes (22NPM39A and 22NPM40).

In the FHVB domain, titanite grains in the Hbl-Cpx schist (22NPM48A3) and the semi-brittle titanite seams that crosscut the Grt-leucosome align with $S_{3\text{-FHVB}}$ formation. Titanites in the Amp-rich bands and late seams exhibit sector zoning (Figure 3.5A) suggesting changes in metamorphic conditions during crystallization at ~ 1.0 Ga due to temperature, pressure, or geochemical variations (e.g., Frost et al., 2000; Kohn, 2017). These titanites show parabolic REE patterns with positive Eu anomalies (Figure 3.6), reflecting Eu^{+2} incorporation from likely Ca-rich Pl and Cpx breakdown during amphibolite-facies metamorphism and associated hydration reactions (e.g., Bucher and Grapes, 2011).

This later D3 Grenvillian deformation (~ 1.0 Ga), characterized by greenschist-facies shearing in the LHsz and SLsz, overlaps with the transition from high-temperature pervasive strain (D1/D2) to localized discrete shear ($S_{3\text{-FHVB}}$) in the FHVB domain. This suggests that post-peak metamorphic conditions and continuous deformation in D2 were succeeded by strain localization ($S_{3\text{-FHVB}}$) in the FHVB domain and reverse oblique shearing at the southern FHVB domain margin under amphibolite- to greenschist-facies conditions. This later D3 event is therefore defined by continued exhumation and strain localization in the FHVB domain overprinting the southeast-verging, thrust-sense LHsz/SLsz system (Table 4-1).

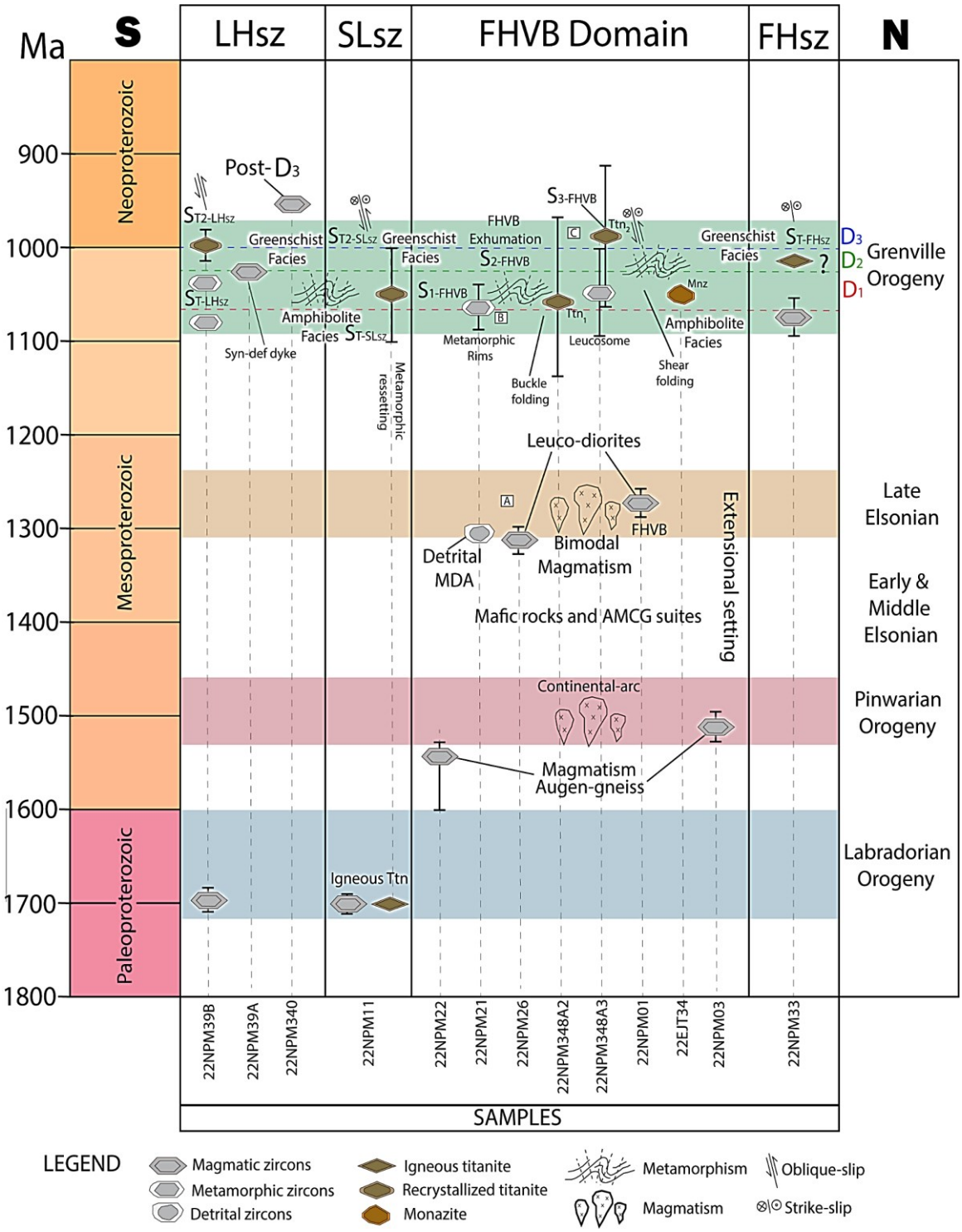

Figure 4.2. *Geochronological summary sketch of the study area, including from south to north the LHsz, the SLsz, the FHVB domain, and the FHsz. Main tectonic and metamorphic events, related magmatic and sedimentary cycles, and significant geochronological crystallization ages of accessory phases are indicated with their respective uncertainties. Tectonic events are based on Gower and Krogh (2002), Haley (2014), and Gower (2019).*

The Fox Harbour shear zone (D3)

In the FHsz, the fine-grained mylonitic diorite dyke (22NPM33) intrudes the host rock at 1079 ± 9 Ma (Figure 2.10 and Figure 3.17). This dyke emplacement age places a maximum age on pervasive amphibolite- to greenschist-facies transposition foliation ($S_{T\text{-}FHsz}$), which is characterized by aligned Amp+Ttn and Pl that are partially replaced by weakly aligned Bt+Chl+Ser (Figure 3.14). The FHsz horizontal stretching lineations ($L_{T\text{-}FHsz}$), defined by elongated Amp crystals that locally form L/S-tectonites, show high finite strain and dextral shear sense in medium to high-temperature mylonites (quartz microstructures 500-600 °C), which are obscured by late static recrystallization.

The distinct strike-slip kinematics in the FHsz could suggest that amphibolite-facies shearing ($S_{T\text{-}FHsz}$) occurred at a distinct time to the thrust-sense $S_{T\text{-}LHsz}$ and $S_{T\text{-}SLsz}$. Alternatively, all amphibolite to greenschist-facies transposition shear zones ($S_{T\text{-}LHsz}$/$S_{T\text{-}SLsz}$ and $S_{T\text{-}FHsz}$) may have operated synchronously with $S_{3\text{-}FHVB}$ in the FHVB in a broader heterogeneous transpressive regime (D3) resulting from a combination of kinematically distinct simple and pure shear components (e.g., Fossen, 2017). However, more precise geochronological dating in the FHsz is required to confirm this speculation (Table 4-1).

Domain	Grenvillian metamorphism and deformation			
	Peak metamorphism (D1) ***1.06 - 1.04 Ga***	*Early deformation (D2)* ***1.04 - 1.02 Ga***	*Thrusting and strain localization (D3)* ***1.0 Ga***	***Post-D3*** ***0.95 Ga***
FHsz	Diorite dyke emplacement 1.07 Ga		Mylonitic Diorite (Ttn; 1.0 Ga) $S_{T\text{-}FHsz}$	
FHVB Domain	Quartzite (Zrn; 1.06 Ga) $S_{1\text{-}FHVB}$	Cooling and folding ($S_{2\ FHVB}$)	Mafic schist (Ttn; 1.0 Ga) $S_{3\text{-}FHVB}$	
	Mafic schist (Ttn; 1.5 Ga) $S_{1\text{-}FHVB}$			
	Leucosome (Zrn; 1.04 Ga) $S_{1\text{-}FHVB}$			
	Crn-Sil schist (Mnz; 1.04 Ga) $S_{1\text{-}FHVB}$			
SLsz			Mylonitic Granodiorite (Ttn*; 1.0 Ga) $S_{T\text{-}SLsz}$	
LHsz			Mylonitic Granodiorite (Ttn; 1.0 Ga) $S_{T\text{-}LHsz}$	Monzogranitic dyke (Zrn; 0.95 Ga)

Table 4-1. *Summary table of Grenvillian structural fabric ages within different domains related to regional deformation episodes. Ttn*: 1.7 Ga Igneous titanite with Grenvillian resetting in the SLsz.*

4.1.3.3 Post D3 (~ 0.95 Ga)

The cessation of deformation in the LHsz is indicated by the appearance of undeformed tabular monzogranitic dykes (Figure 2.6B). This monzogranite (22NPM40) exhibits inherited zircon grains that roughly match the ages and population in the host granodiorite (22NPM39B). However, an acicular zircon population with high Th/U ratios

are interpreted to be related to the crystallization age of the dyke, in which one single grain yielded a date of 951 Ma. This age is coeval with numerous granitic intrusions in the PT, which range in age from 966 to 956 Ma (Gower (2019), and references therein). These intrusions form discrete, circular to elliptical bodies, ranging from 5 to 20 km in diameter in plan view and are associated with prominent positive aeromagnetic anomalies (Gower, 2019).

4.2 Regional interpretation and tectonic evolution

4.2.1 Grenvillian Tectonic Evolution of the FHVB

The Grenvillian orogenesis in the Eastern Grenville Province extends from 1090 to 985 Ma, followed by late- to post-orogenic activity until 950 Ma (Gower, 1996; Gower and Krogh, 2002). This orogeny represents a compressional continental collision regime between Amazonia and the southern margin of Laurentia (Tohver et al., 2004). In the Eastern Grenville province, an indentor tectonism model proposed by Gower et al. (2008a) describes a transition from frontal-thrusting to lateral-ramp tectonics around the indentor corner (syntaxis) in the Rigolet area (Figure 1.1). This produced north-verging reverse-slip shearing, driven by the thrusting of the LMT over pre-Grenvillian Laurentia along the Rigolet shear zone (Corrigan et al., 2000). In the context of the indentor model, the Grenville orogenesis is recorded earlier in the LMT (~ 1090 Ma) compared to other terranes like the Pinware terrane (1030 to 985 Ma, Tucker and Gower, 1994) and the MMT, where only subtle Grenvillian thrusting is recorded around 1010 Ma (Gower, 2019), thus representing likely higher structural levels at ~1090 Ma. Evidence of this earliest Grenvillian deformation includes significant tectonic activity in the LMT by 1.08 to 1.05

Ga (Schärer and Gower, 1988; Scott et al., 1993; Corrigan et al., 2000), whereas in the Rigolet area, NW-verging thrusting and folding at 1.08–1.05 Ga buried the LMT producing high-grade amphibolite- to granulite-facies metamorphism (Corrigan et al., 2000). During this northward-directed convergence, the MMT was likely thrust over the LMT, where the hanging wall remained relatively undeformed. This relationship reflects a tectonic lid scenario, where the MMT remained largely unaffected by metamorphism and deformation, while the footwall (LMT) underwent significant burial, migmatization, and deformation between 1.08 and 1.02 Ga recorded by several 1060-1040 Ma zircon and monazite ages in the LMT (Scott et al., 1993; Wasteneys et al., 1997; Corrigan et al., 2000). This extended period of metamorphism suggests that high-grade conditions in the northern LMT were maintained throughout the entire period rather than indicating any progressive decline in temperature. The end of this event is inferred between 1045 and 1020 Ma, based on the closure temperature of titanites (Scharer et al., 1986) and orogenic collapse in the Grenville hinterland farther southwest during the late Ottawan phase of the Grenville orogeny (1.09 to 1.02 Ga, Rivers, 2012).

Record of this early to peak-metamorphism (1.06-1.04 Ga) is evidenced in the FHVB domain in high-grade amphibolite-facies metamorphism during D1 (Figure 4.2 and Figure 4.3B) and reflects the tectonic burial and peak metamorphism throughout the entirety of the LMT (Scott et al., 1993; Wasteneys et al., 1997; Corrigan et al., 2000). Deformation and (D2) was extended until ~ 1.02 Ga in the FHVB domain, coinciding with the inferred cessation of deformation in the northern LMT around 1020 Ma (Scharer et al., 1986),

associated with lower amphibolite to greenschist facies retrogression (Corrigan et al., 2000).

By contrast, the PT and MMT (orogenic lid) lack evidence of significant Ottawan phase metamorphism, likely because of their hanging wall position during convergence. The N-verging thrusting observed in the Rigolet area (Corrigan et al., 2000) suggests possible contemporaneous northward thrusting in the southeastern part of the LMT. North-verging thrusting of the PT over the FHVB domain and LMT is not preserved in any structures but is consistent with ages and metamorphism in the PT and FHVB domain. D1 events in the FHVB domain could be due to the burial of the LMT while the PT/MMT resided in a hanging wall position in the tectonic pile and largely was unaffected by Ottawan phase deformation.

Regional correlation to FHVB D3

The collapse of the Ottawan phase was followed by the Rigolet phase (1005 to 980 Ma Rivers et al., 2012), which marks the propagation of the orogen against the Archean basement of Laurentia. Most of the strain that developed in the Rigolet shear zone segment is inferred to be Labradorian in age, and only the upper structural levels were reworked during the Grenvillian Orogeny, in which the southerly-dipping mylonitic foliations become progressively overprinted by sub-vertical shear zones with sub-horizontal lineations south of the Rigolet shear zone (Corrigan et al., 2000). In the northern LMT, strain localization from lower-amphibolite to greenschist-facies transcurrent shearing affected the southern part of the domain boundary (English River shear zone, Corrigan et

al., 2000). This 1015-1005 Ma dextral strike-slip shear is associated with a distinctive low magnetic anomaly that extends towards the southeast Labrador coast.

D3 in the southern LMT represents a high-to-low-temperature evolution in which pervasive deformation (D1/D2) transitioned to localized oblique and strike-slip shearing that aided the cooling and exhumation of the FHVB domain around 1.0 Ga. This D3 event aligns with the Ar-Ar and K-Ar ages of ~1000 Ma, known as the 'Grenvillian thermal threshold' by Gower (2003), which coincides with the LMT, meaning that this terrane was tectonically active from 1.08 Ga but had cooled below Bt and Hbl closure temperatures (~350 ºC) by 1.0 Ga (Gower, 2003).

Additionally, this strain localization, marked by D3 retrograde greenschist-facies in the south-directed LHsz/SLsz and the dextral strike-slip shearing FHsz, overlaps in time to the Rigolet phase (1.02-0.98 Ga, Rivers, 2012) of the Grenville Orogeny. This youngest re-partitioning of strain has been reported in thrusting and cooling events between 1010 and 990 Ma in the MMT, including a 1003 Ma titanite from Second Choice Lake pegmatite (Gower et al., 1991) and a 990 Ma titanite from the Lower Brook leucosome (Philippe et al., 1993). In the study area, this strain manifests as an overall transpressive regime involving combinations of coaxial and non-coaxial deformation (e.g., Fossen, 2017) with distinct kinematics. The south-directed thrusting and exhumation in the southern LMT contrasts with strike-slip shear in the northern LMT during D3, highlighting the heterogeneous nature of strain along this long-lived and complex margin (Figure 4.3C). Previous models speculated that north-directed thrusting structures formed during the early

Ottawan Phase and were then overprinted by sub-vertical structures likely attributed to the late Ottawan extension (Rivers, 2008 and 2012).

Cessation of deformation is inferred during a post-Grenvillian magmatic event where felsic intrusions (975-955 Ma) up to a few meters across and plutons several kilometers in diameter in the PT (Gower, 2019) intrude all known Grenvillian fabrics and remain undeformed. The 956 Ma post-deformational monzonitic dyke that crosscuts the mylonitization in the LHsz; marks the cessation of the deformation in the study area (Figure 4.3D), likely associated with late stages of orogenic collapse (Rivers et al. 2012) or related with late stages of opening of the Asgard sea (Strowbridge et al., 2022) around 0.95 Ga.

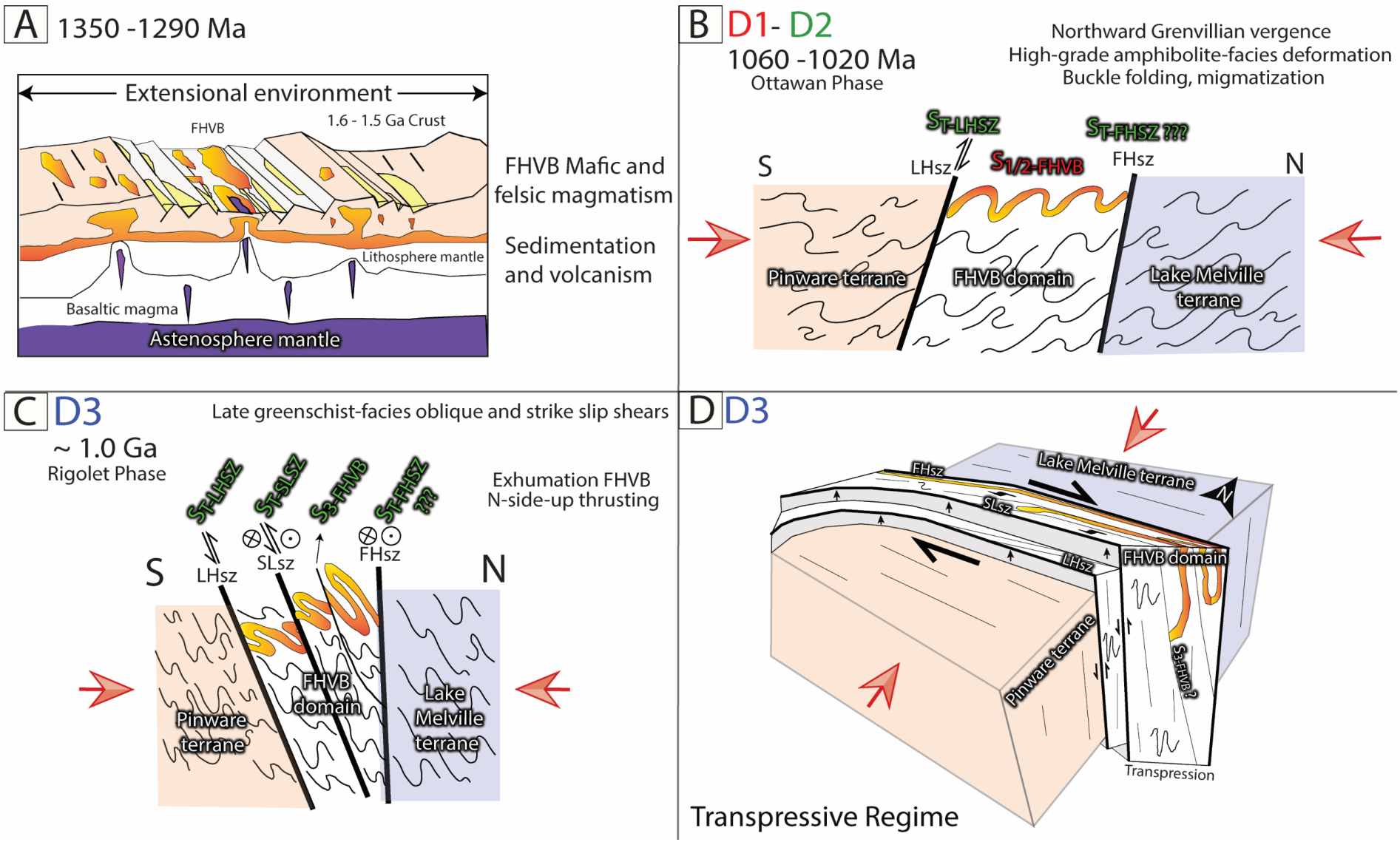

Figure 4.3 *Schematic multi-stage evolution for the Eastern Grenville Province in southeast Labrador, from 1.3 Ga formation of the FHVB to the Grenville Orogeny.* ***A)*** *Formation and deposition of the supracrustal bimodal packages of the FHVB atop the 1.7-1.5 Ga basement.* ***B)*** *Early to peak high-temperature Grenvillian deformation (D1-D2) between 1.06 and 1.02 Ga, with attendant buckle folding, shear folding, and north-directed thrusting.* ***C)*** *The evolution of shortening and the development of localized greenschist-facies oblique slip and strike-slip structures that facilitated the southward exhumation of the FHVB.* ***D)*** *Schematic diagram showing the transpressional regime (e.g., Fossen, 2017) between the oblique-slip and strike-slip structures with a probably north-south directed shortening. Vertical scale is exaggerated for clarity.*

Conclusion

This study refines the tectonic evolution of the 1.3 Ga FHVB, its basement rocks, and associated shear boundary structures through detailed fieldwork, structural analysis, and U-Pb petrochronology. U-Pb zircon ages confirm that the FHVB represents a bimodal volcano-sedimentary sequence comprising REE-bearing peralkaline rhyolites, mafic, and sedimentary rocks, all deposited ~1.3 Ga in an extensional setting along the Laurentian margin atop dismembered Labradorian-Pinwarian (1.7-1.5 Ga) basement.

U-Pb petrochronological results from zircon, monazite, and titanite reveal pervasive Grenvillian metamorphism and deformation that progressively affected the FHVB and its basement rocks. High-grade amphibolite-facies peak metamorphism (D1, ~1.06-1.04 Ga), is characterized by folding and migmatization during the tectonic burial and heating of the Lake Melville Terrane, with the Pinware and Mealy Mountains Terranes likely in a hanging wall position, remaining higher in the tectonic pile as they were thrust northward during this D1 event. Post-peak metamorphism and subsequent deformation (D2, ~1.04-1.02 Ga) involved buckle- and shear folding and localized dextral shearing during cooling, coeval with the regional collapse of the Ottawan Orogeny. Further cooling and strain localization developed sub-vertical strike-slip structures and south-vergent shear systems in a transpressive regime, facilitating the amphibolite to greenschist-facies southward exhumation of the FHVB during ~1.0 Ga D3 events that coincide with the Rigolet phase. Deformation ceased during a post-Grenvillian magmatic event (975–955 Ma) characterized by undeformed felsic intrusions in the PT and 956 Ma monzonitic dykes crosscutting

Grenvillian fabrics. These features mark a renewed extensional period around 0.95 Ga, representing the final stages of the tectonic evolution of the FHVB and surrounding regions.

References

Aleinikoff, J. N., Schenck, W. S., Plank, M. O., Srogi, L., Fanning, C. M., Kamo, S. L., & Bosbyshell, H. (2006). Deciphering igneous and metamorphic events in high-grade rocks of the Wilmington Complex, Delaware: Morphology, cathodoluminescence and backscattered electron zoning, and SHRIMP U-Pb geochronology of zircon and monazite. Geological Society of America Bulletin, 118(1-2), 39-64.

Aleinikoff, J. N., Wintsch, R. P., Fanning, C. M., & Dorais, M. J. (2002). U–Pb geochronology of zircon and polygenetic titanite from the Glastonbury Complex, Connecticut, USA: an integrated SEM, EMPA, TIMS, and SHRIMP study. Chemical Geology, 188(1-2), 125-147.

Basson, I. J., Muntingh, J. A., Jellicoe, B. C., & Anthonissen, C. J. (2016). Structural interpretation of the Steenkampskraal monazite deposit, Western Cape, South Africa. Journal of African Earth Sciences, 121, 301-315.

Bingen, B., Davis, W. J., & Austrheim, H. (2001). Zircon U-Pb geochronology in the Bergen arc eclogites and their Proterozoic protoliths, and implications for the pre-Scandian evolution of the Caledonides in western Norway. Geological Society of America Bulletin, 113(5), 640-649.

Brooks, C (1984). The Sm–Nd age of Labrador rock samples. A report to Energy Mines and Resources concerning contract serial no. OS83-00200. Unpublished Report to the Newfoundland Department of Mines and Energy, 15 pages.

Bucher, K., & Grapes, R. (2011). Petrogenesis of metamorphic rocks (Vol. 428). Berlin: Springer.

Cawood, P. A., Hawkesworth, C. J., & Dhuime, B. (2012). Detrital zircon record and tectonic setting. Geology, 40(10), 875-878.

Cherniak, D. J. (1993). Lead diffusion in titanite and preliminary results on the effects of radiation damage on Pb transport. Chemical Geology, 110(1-3), 177-194.

Cherniak, D. J., & Pyle, J. M. (2008). Th diffusion in monazite. Chemical Geology, 256(1-2), 52-61.

Corfu, F., Hanchar, J. M., Hoskin, P. W., & Kinny, P. (2003). Atlas of zircon textures. Reviews in mineralogy and geochemistry, 53(1), 469-500.

Corrigan, D., Rivers, T., & Dunning, G. (2000). U–Pb constraints for the plutonic and tectonometamorphic evolution of Lake Melville terrane, Labrador and implications for basement reworking in the northeastern Grenville Province. Precambrian Research, 99(1-2), 65-90.

Coutts, D. S., Matthews, W. A., & Hubbard, S. M. (2019). Assessment of widely used methods to derive depositional ages from detrital zircon populations. Geoscience Frontiers, 10(4), 1421-1435.

Dickinson, W. R., & Gehrels, G. E. (2009). Use of U–Pb ages of detrital zircons to infer maximum depositional ages of strata: a test against a Colourado Plateau Mesozoic database. Earth and Planetary Science Letters, 288(1-2), 115-125.

Emslie, R. F., Loveridge, W. D., & Stevens, R. D. (1984). The Mealy dykes, Labrador: petrology, age, and tectonic significance. Canadian Journal of Earth Sciences, 21(4), 437-446.

Engi, M. (2017). Petrochronology based on REE-minerals: monazite, allanite, xenotime, apatite. Reviews in Mineralogy and Geochemistry, 83(1), 365-418.

Fisher, C. M., Bauer, A. M., Luo, Y., Sarkar, C., Hanchar, J. M., Vervoort, J. D., ... & Pearson, D. G. (2020). Laser ablation split-stream analysis of the Sm-Nd and U-Pb isotope compositions of monazite, titanite, and apatite–Improvements, potential reference materials, and application to the Archean Saglek Block gneisses. Chemical Geology, 539, 119493.

Finger, F., Gerdes, A., Rene, M., & Riegler, G. (2009). The Saxo-Danubian Granite Belt: magmatic response to post-collisional delamination of mantle lithosphere below the southwestern sector of the Bohemian Massif (Variscan orogen). Geologica Carpathica, 60(3), 205.

Fossen, H. (2016). Structural geology. Cambridge University Press.

Fossen, H., & Cavalcante, G. C. G. (2017). Shear zones–A review. Earth-Science Reviews, 171, 434-455.

Frost, B. R., Chamberlain, K. R., & Schumacher, J. C. (2001). Sphene (titanite): phase relations and role as a geochronometer. Chemical geology, 172(1-2), 131-148.

Gehrels, G. E., Valencia, V. A., & Ruiz, J. (2008). Enhanced precision, accuracy, efficiency, and spatial resolution of U-Pb ages by laser ablation–multi-collector–inductively coupled plasma–mass spectrometry. Geochemistry, Geophysics, Geosystems, 9(3).

Gonçalves, G. O., Lana, C., Scholz, R., Buick, I. S., Gerdes, A., Kamo, S. L., ... & Nalini Jr, H. A. (2016). An assessment of monazite from the Itambé pegmatite district for use as U–Pb isotope reference material for microanalysis and implications for the origin of the "Moacyr" monazite. Chemical Geology, 424, 30-50.

Gordon, S. M., Kirkland, C. L., Reddy, S. M., Blatchford, H. J., Whitney, D. L., Teyssier, C., & McDonald, B. J. (2021). Deformation-enhanced recrystallization of titanite drives decoupling between U-Pb and trace elements. Earth and Planetary Science Letters, 560, 116810.

Gower, C. F., & Owen, V. (1984). Pre-Grenvillian and Grenvillian lithotectonic regions in eastern Labrador—correlations with the Sveconorwegian Orogenic Belt in Sweden. Canadian Journal of Earth Sciences, 21(6), 678-693.

Gower, C. F. (1985). Correlations between the Grenville Province and Sveconorwegian Orogenic Belt. In The Deep Proterozoic Crust in the North Atlantic Provinces. Edited by A.C. Tobi and J.L.R. Touret. NATO Advanced Study Institute, Series C. Mathematical and Physical Sciences, Volume 158, pages 247-257.

Gower, C. F. (1987). The Hawke River Terrane-a newly defined lithotectonic entity in the Grenville Province of eastern Labrador. Geol. Assoc. Canada, Abstracts with Program 12: 48.

Gower, C. F., & Loveridge, W. D. (1987). Grenvillian plutonism in the eastern Grenville Province. Radiogenic age and isotopic studies: Report, 1, 87-2.

Gower, C.F., Neuland, S., Newman, M. and Smyth, J. (1987): Geology of the Port Hope Simpson map region, Grenville Province, eastern Labrador. In Current Research. Government of Newfoundland and Labrador, Department of Mines, Mineral Development Division, Report 87-1, pages 183-199. [NFLD/1667]

Gower, C. F., & Erdmer, P. (1988). Proterozoic metamorphism in the Grenville Province: a study in the Double Mer–Lake Melville area, eastern Labrador. Canadian Journal of Earth Sciences, 25(11), 1895-1905.

Gower, C. F., Heaman, L. M., Loveridge, W. D., Schärer, U., & Tucker, R. D. (1991). Grenvillian magmatism in the eastern Grenville Province, Canada. Precambrian Research, 51(1-4), 315-336.

Gower, Charles F., Urs Schärer, and Larry M. Heaman (1992). The Labradorian orogeny in the Grenville province, eastern Labrador, Canada. Canadian Journal of Earth Sciences 29.9: 1944-1957.

Gower, C.F. van Nostrand, T., Peckham, V. and Anderson, J. (1993): Geology of the Upper St. Lewis River map region, southeast Labrador. In Current Research. Government of Newfoundland and Labrador, Department of Mines and Energy, Geological Survey Branch, Report 93-1, pages 17-34. [NFLD/2496]

Gower, C. F., & Tucker, R. D. (1994). Distribution of pre-1400 Ma crust in the Grenville province: Implications for rifting in Laurentia-Baltica during geon 14. Geology, 22(9), 827-830.

Gower, C. F. (1996). The evolution of the Grenville Province in eastern Labrador, Canada. Geological Society, London, Special Publications, 112(1), 197-218.

Gower, C.F., Hall, J., Kilfoil, G.J., Quinlan, G.M. and Wardle, R.J. (1997a): Roots of the Labradorian orogen in the Grenville Province in southeast Labrador: Evidence from marine, deep-seismic reflection data. Tectonics, Volume 16, pages 795-809.

Gower, C. F., & Krogh, T. E. (2002). U–Pb geochronological review of the Proterozoic history of the eastern Grenville Province. Canadian Journal of Earth Sciences, 39(5), 795-829.

Gower, C. F. (2003). Implications of re-assessed $^{40}Ar/^{39}Ar$ and K–Ar geochronological data for Grenvillian orogenesis in the eastern Grenville Province. In Current Research. Government of Newfoundland and Labrador, Department of Mines and Energy, Geological Survey, Report 03-1, pages 15-33.

Gower, C. F. (2005). Kinematic evidence for terrane displacements in the Grenville Province in eastern Labrador. Current Research. Department of Natural Resources, Geological Survey Branch, Report, 1, 73-92.

Gower, C. F., Kamo, S., & Krogh, T. E. (2008). Indentor tectonism in the eastern Grenville Province. Precambrian Research, 167(1-2), 201-212.

Gower, C.F., (2012). The Grenville Province of southeast Labrador and adjacent Quebec. Geological Association of Canada –Mineralogical Association of Canada, Joint Annual Meeting, St. John's, Field Trip Guidebook – B6, 140 pp

Gower, C. F. (2019). Regional Geology of Eastern Labrador (Eastern Makkovik and Grenville Provinces). Newfoundland and Labrador. Department of Natural Resources, Mines.

Haley, J. T. (2014). 1.3 Ga bimodal volcanism in southeastern Labrador: Fox Harbour (Doctoral dissertation, Memorial University of Newfoundland).

Hanmer, S., and D. J. Scott (1990). Structural observations in the Gilbert River belt, Grenville Province, southeastern Labrador. Current Research, Part C. Geologic Survey of Canada, Paper (1990): 1-11.

Hetherington, C. J., Backus, E. L., McFarlane, C. R., Fisher, C. M., & Pearson, D. G. (2018). Origins of textural, compositional, and isotopic complexity in monazite and its petrochronological analysis. Microstructural Geochronology: Planetary Records Down to Atom Scale, 63-90.

Hoffman, P.F. 1989. Precambrian geology and tectonic history of North America. In The geology of North America——an overview. Edited by A.W. Bally and A.R. Palmer. Geological Society of America, Decade of North American Geology. vol. A. pp. 447–512.

Hoskin, P. W., & Schaltegger, U. (2003). The composition of zircon and igneous and metamorphic petrogenesis. Reviews in mineralogy and geochemistry, 53(1), 27-62.

Indares, A. (2020). Deciphering the metamorphic architecture and magmatic patterns of large hot orogens: Insights from the central Grenville Province. Gondwana Research, 80, 385-409.

Indares, A. (2024). The Grenville Province: revisiting the orogenic framework and integrating recent findings. Canadian Journal of Earth Sciences, (ja).

Janots, E., Engi, M., Berger, A., Allaz, J., Schwarz, J. O., & Spandler, C. (2008). Prograde metamorphic sequence of REE minerals in pelitic rocks of the Central Alps: implications for allanite–monazite–xenotime phase relations from 250 to 610 C. Journal of Metamorphic Geology, 26(5), 509-526

Jochum, K. P., Weis, U., Stoll, B., Kuzmin, D., Yang, Q., Raczek, I., ... & Enzweiler, J. (2011). Determination of reference values for NIST SRM 610–617 glasses following ISO guidelines. Geostandards and Geoanalytical Research, 35(4), 397-429.

Kamo, S. L., Heaman, L. M., & Gower, C. F. (2011). Evidence for post-1200 Ma—pre-Grenvillian supracrustal rocks in the Pinware terrane, eastern Grenville Province at Battle Harbour, Labrador. Canadian Journal of Earth Sciences, 48(2), 371-387.

Kirkland, C. L., Spaggiari, C. V., Johnson, T. E., Smithies, R. H., Danišík, M., Evans, N., ... & McDonald, B. J. (2016). Grain size matters: Implications for element and isotopic mobility in titanite. Precambrian Research, 278, 283-302.

Kirkland, C. L., Yakymchuk, C., Gardiner, N. J., Szilas, K., Hollis, J., Olierook, H., & Steenfelt, A. (2020). Titanite petrochronology linked to phase equilibrium modelling constrains tectono-thermal events in the Akia Terrane, West Greenland. Chemical Geology, 536, 119467.

Ketchum, J. W., Jackson, S. E., Culshaw, N. G., & Barr, S. M. (2001). Depositional and tectonic setting of the Paleoproterozoic Lower Aillik Group, Makkovik Province, Canada: evolution of a passive margin-foredeep sequence based on petrochemistry and U–Pb (TIMS and LAM-ICP-MS) geochronology. Precambrian Research, 105(2-4), 331-356.

Knoper, M., Armstrong, R. A., Andreoli, M. A. G., & Ashwal, L. D. (2000). The Steenkampskraal monazite vein: a subhorizontal stretching shear zone indicating extensional collapse of Namaqualand at 1033 Ma. Journal of African Earth Sciences, 31(1), 38-38.

Kohn, M. J., & Malloy, M. A. (2004). Formation of monazite via prograde metamorphic reactions among common silicates: implications for age determinations. Geochimica et Cosmochimica Acta, 68(1), 101-113.

Kohn, M. J. (2014). Himalayan metamorphism and its tectonic implications. Annual Review of Earth and Planetary Sciences, 42(1), 381-419.

Kohn, M. J. (2017). Titanite petrochronology. Reviews in Mineralogy and Geochemistry, 83(1), 419-441.

Kowallis, B. J., Christiansen, E. H., & Griffen, D. T. (1997). Compositional variations in titanite. In Geological Society of America Abstracts with Programs (Vol. 29, No. 6, p. 402).

Kowallis, B. J., Christiansen, E. H., Dorais, M. J., Winkel, A., Henze, P., Franzen, L., & Mosher, H. (2022). Variation of Fe, Al, and F substitution in titanite (sphene). Geosciences, 12(6), 229.

Ma, Q., Evans, N. J., Ling, X. X., Yang, J. H., Wu, F. Y., Zhao, Z. D., & Yang, Y. H. (2019). Natural titanite reference materials for in situ U-Pb and Sm-Nd isotopic measurements by LA-(MC)-ICP-MS. Geostandards and Geoanalytical Research, 43(3), 355-384.

MagyarosI, Z., & Rayner, N. (2023). Rare earth element mineralization associated with the peralkaline Fox Harbour Volcanic Belt, southeastern Labrador, Canada. Atlantic Geoscience, 59.

Miller, R. R. (2015). Pantellerite-hosted rare earth element mineralization in southeast Labrador: The Foxtrot deposit. In Symposium on critical and strategic materials. British Columbia Geological Survey Paper (Vol. 3, p. 109).

Moser, Amy C., Bradley R. Hacker, George E. Gehrels, Gareth GE Seward, Andrew RC Kylander-Clark, and Joshua M. Garber (2022). "Linking titanite U–Pb dates to coupled deformation and dissolution–reprecipitation." Contributions to Mineralogy and Petrology 177, no. 3 (2022): 42.

Olierook, H. K., Taylor, R. J., Erickson, T. M., Clark, C., Reddy, S. M., Kirkland, C. L., ... & Barham, M. (2019). Unravelling complex geologic histories using U–Pb and trace element systematics of titanite. Chemical Geology, 504, 105-122.

O'Sullivan, G., Scibiorski, E., & Mark, C. (2024). Predictive models for detrital titanite provenance with application to the Nanga Parbat—Haramosh syntaxial massif, western Himalaya. Journal of Geophysical Research: Earth Surface, 129(5), e2023JF007351.

Owen, J. V. (1988). Geochemical changes accompanying the mylonitization of diverse rock types from the Grenville Front zone, eastern Labrador. Canadian Journal of Earth Sciences, 25(9), 1472-1484.

Passchier, C. W., & Trouw, R. A. (2005). Microtectonics. Springer Science & Business Media.

Perrot, M., Tremblay, A., & David, J. (2017). Detrital zircon U-Pb geochronology of the Magog Group, southern Quebec–stratigraphic and tectonic implications for the Quebec Appalachians. American Journal of Science, 317(10), 1049-1094.

Petrus, J. A., & Kamber, B. S. (2012). VizualAge: A novel approach to laser ablation ICP-MS U-Pb geochronology data reduction. Geostandards and Geoanalytical Research, 36(3), 247-270.

Pidgeon, R. T. (1992). Recrystallization of oscillatory zoned zircon: some geochronological and petrological implications. Contributions to Mineralogy and Petrology, 110(4), 463-472.

Philippe, S., Wardle, R.J. and Schärer, U. (1993). Labradorian and Grenvillian crustal evolution of the Goose Bay region, Labrador: New U–Pb geochronological constraints. Canadian Journal of Earth Sciences, Volume 30, pages 2315-2327.

Pyle, J. M., Spear, F. S., Rudnick, R. L., & McDONOUGH, W. F. (2001). Monazite–xenotime–garnet equilibrium in metapelites and a new monazite–garnet thermometer. Journal of Petrology, 42(11), 2083-2107.

Reynolds, P. H. (1989). 40Ar/39Ar dating of the Mealy dykes of Labrador: paleomagnetic implications. Canadian Journal of Earth Sciences, 26(8), 1567-1573.

Richter, M., Nebel-Jacobsen, Y., Nebel, O., Zack, T., Mertz-Kraus, R., Raveggi, M., & Rösel, D. (2019). Assessment of five monazite reference materials for U-Th/Pb dating using laser-ablation ICP-MS. Geosciences, 9(9), 391.

Rivers, T., Martignole, J., Gower, C. F., & Davidson, A. (1989). New tectonic divisions of the Grenville Province, southeast Canadian Shield. Tectonics, 8(1), 63-84.

Rivers, T. (2008). Assembly and preservation of lower, mid, and upper orogenic crust in the Grenville Province—Implications for the evolution of large hot long-duration orogens. Precambrian Research, 167(3-4), 237-259.

Rivers, T. (2009). The Grenville Province as a large hot long-duration collisional orogen–insights from the spatial and thermal evolution of its orogenic fronts. Geological Society, London, Special Publications, 327(1), 405-444.

Rivers, T. (2012). Upper-crustal orogenic lid and mid-crustal core complexes: signature of a collapsed orogenic plateau in the hinterland of the Grenville Province. *Canadian Journal of Earth Sciences*, *49*(1), 1-42.

Rubatto, D. (2017). Zircon: The Metamorphic Mineral. Reviews in Mineralogy and Geochemistry, 83, 261–295.

Rubatto, D., & Gebauer, D. (2000). Use of cathodoluminescence for U-Pb zircon dating by ion microprobe: some examples from the Western Alps. In Cathodoluminescence in geosciences (pp. 373-400). Berlin, Heidelberg: Springer Berlin Heidelberg.

Rubatto, D., Williams, I. S., & Buick, I. S. (2001). Zircon and monazite response to prograde metamorphism in the Reynolds Range, central Australia. Contributions to Mineralogy and Petrology, 140(4), 458-468.

Rubatto, D., Hermann, J., & Buick, I. S. (2006). Temperature and bulk composition control on the growth of monazite and zircon during low-pressure anatexis (Mount Stafford, central Australia). Journal of Petrology, 47(10), 1973-1996.

Sawyer, E. W. (2008). Atlas of migmatites (Vol. 9). NRC Research press.

Scibiorski, E., Kirkland, C. L., Kemp, A. I. S., Tohver, E., & Evans, N. J. (2019). Trace elements in titanite: A potential tool to constrain polygenetic growth processes and timing. Chemical Geology, 509, 1-19.

Scibiorski, E. A., & Cawood, P. A. (2022). Titanite as a petrogenetic indicator. Terra Nova, 34(3), 177-183.

Schaltegger, U., & Davies, J. H. (2017). Petrochronology of zircon and baddeleyite in igneous rocks: Reconstructing magmatic processes at high temporal resolution. Reviews in Mineralogy and Geochemistry, 83(1), 297-328.

Schärer, U., Krogh, T. E., & Gower, C. F. (1986). Age and evolution of the Grenville Province in eastern Labrador from U-Pb systematics in accessory minerals. Contributions to Mineralogy and Petrology, 94, 438-451.

Schärer, U., & Gower, C. F. (1988). Crustal evolution in eastern Labrador: constraints from precise U-Pb ages. Precambrian Research, 38(4), 405-421.

Scott, D. J., Machado, N., Hanmer, S., & Garièpy, C. (1993). Dating ductile deformation using U–Pb geochronology: examples from the Gilbert River Belt, Grenville Province, Labrador, Canada. Canadian Journal of Earth Sciences, 30(7), 1458-1469.

Search Minerals (2010). Report on a Detailed Airborne Magnetic Gradiometer and Radiometrics Survey – Porto Hope Simpson, Labrador.

Šilerová, D., Dyck, B., Cutts, J. A., & Larson, K. (2023). Long-Lived (180 Myr) Ductile Flow Within the Great Slave Lake Shear Zone. Tectonics, 42(9), e2022TC007721.

Sláma, J., Košler, J., Condon, D. J., Crowley, J. L., Gerdes, A., Hanchar, J. M., ... & Whitehouse, M. J. (2008). Plešovice zircon—a new natural reference material for U–Pb and Hf isotopic microanalysis. Chemical geology, 249(1-2), 1-35.

Spencer, K. J., Hacker, B. R., Kylander-Clark, A. R. C., Andersen, T. B., Cottle, J. M., Stearns, M. A., ... & Seward, G. G. E. (2013). Campaign-style titanite U–Pb dating by laser-ablation ICP: Implications for crustal flow, phase transformations and titanite closure. Chemical Geology, 341, 84-101.

Spencer, C. J., Kirkland, C. L., & Taylor, R. J. (2016). Strategies towards statistically robust interpretations of in situ U–Pb zircon geochronology. Geoscience Frontiers, 7(4), 581-589.

Stacey JS, Kramers JD (1975) Approximation of terrestrial lead isotope evolution by a two-stage model. Earth Planet Sci Lett 26:207–221.

Strowbridge S., Indares A., Dunning G., Walle M. (2022). A Tonian volcano-sedimentary succession in Newfoundland, eastern North America: a post-Grenvillian link to the Asgard Sea? Geology, 50: 655–659.

Sun, J., Yang, J., Wu, F., Xie, L., Yang, Y., Liu, Z., & Li, X. (2012). In situ U-Pb dating of titanite by LA-ICPMS. Chinese Science Bulletin, 57, 2506-2516.

Tohver, E., Bettencourt, J. S., Tosdal, R., Mezger, K., Leite, W. B., & Payolla, B. L. (2004). Terrane transfer during the Grenville orogeny: tracing the Amazonian ancestry of southern Appalachian basement through Pb and Nd isotopes. Earth and Planetary Science Letters, 228(1-2), 161-176.

Tomascak, P. B., Krogstad, E. J., & Walker, R. J. (1998). Sm-Nd isotope systematics and the derivation of granitic pegmatites in southwestern Maine. The Canadian Mineralogist, 36(2), 327-337.

Trouw, R. A., Passchier, C. W., & Wiersma, D. J. (2009). Atlas of Mylonites and related microstructures. Springer Science & Business Media.

Tucker, R. D., & Gower, C. F. (1994). U-Pb geochronological framework for the Pinware terrane, Grenville Province, southeast Labrador. The Journal of Geology, 102(1), 67-78.

Vermeesch, P. (2018). IsoplotR: A free and open toolbox for geochronology. Geoscience Frontiers, 9(5), 1479-1493.

Vermeesch, P. (2021). Maximum depositional age estimation revisited. Geoscience Frontiers, 12(2), 843-850.

Wasteneys, H. A., Kamo, S. L., Moser, D., Krogh, T. E., Gower, C. F., & Owen, J. V. (1997). U-Pb geochronological constraints on the geological evolution of the Pinware terrane and adjacent areas, Grenville Province, southeast Labrador, Canada. Precambrian Research, 81(1-2), 101-128.

Wiedenbeck, M. A. P. C., Alle, P., Corfu, F. Y., Griffin, W. L., Meier, M., Oberli, F. V, & Spiegel, W. (1995). Three natural zircon standards for U-Th-Pb, Lu-Hf, trace element and REE analyses. Geostandards newsletter, 19(1), 1-23.

Whitney, D. L., & Evans, B. W. (2010). Abbreviations for names of rock-forming minerals. American mineralogist, 95(1), 185-187.

Williams, M. L., & Jercinovic, M. J. (2002). Microprobe monazite geochronology: putting absolute time into microstructural analysis. Journal of Structural Geology, 24(6-7), 1013-1028.

Williams, M. L., Jercinovic, M. J., & Hetherington, C. J. (2007). Microprobe monazite geochronology: understanding geologic processes by integrating composition and chronology. Annu. Rev. Earth Planet. Sci., 35(1), 137-175.

Winter, J. D. (2014). Principles of igneous and metamorphic petrology (Vol. 2). Harlow, UK: Pearson education.